



HAL
open science

Converging technologies for optical and radio generation dedicated to communications at frequencies above 60 GHz

Ramin Khayatzadeh

► **To cite this version:**

Ramin Khayatzadeh. Converging technologies for optical and radio generation dedicated to communications at frequencies above 60 GHz. Other. Université Grenoble Alpes, 2015. English. NNT : 2015GREAT074 . tel-01231979

HAL Id: tel-01231979

<https://theses.hal.science/tel-01231979>

Submitted on 21 Nov 2015

HAL is a multi-disciplinary open access archive for the deposit and dissemination of scientific research documents, whether they are published or not. The documents may come from teaching and research institutions in France or abroad, or from public or private research centers.

L'archive ouverte pluridisciplinaire **HAL**, est destinée au dépôt et à la diffusion de documents scientifiques de niveau recherche, publiés ou non, émanant des établissements d'enseignement et de recherche français ou étrangers, des laboratoires publics ou privés.

THÈSE

Pour obtenir le grade de

DOCTEUR DE L'UNIVERSITÉ GRENOBLE ALPES

préparée à l'Université Grenoble Alpes

Spécialité : Optique et Radio Fréquence

Arrêté ministériel : le 6 janvier 2005 - 7 août 2006

Présentée par

« **Ramin KHAYATZADEH** »

Thèse dirigée par « **Béatrice CABON** » et « **Julien POËTTE** »

préparée au sein du **Laboratoire IMEP LAHC**

dans l'École Doctorale **E.E.A.T.S**

Convergence des Technologies Optiques et Radio pour la Génération dédiée aux Communications aux Fréquences Supérieures à 60 GHz

Thèse soutenue publiquement le « **22 Septembre 2015** »,
devant le jury composé de :

M. Jean-Pierre, VILCOT

DR CNRS, Président

M. Tchanguiz, RAZBAN

PR Polytech Nantes, Rapporteur

M. Olivier, LLOPIS

DR LAAS, Rapporteur

Mme. Béatrice CABON

PR INP Grenoble, Directrice de thèse

M. Julien POËTTE

MCF INP Grenoble, Co-encadrant de thèse



To the lord of time who surely will come...

Acknowledgements

I would like to appreciate my supervisor Prof. Béatrice CABON and my co-supervisor Dr. Julien POETTE for their great help, guidelines and support.

I would appreciate the engineers in IMEP LAHC Mr. Nicolas CARROA and Gregory GROSA for their strong support during the experiments.

I would thank my colleges and friends in IMEP LAHC, Matthieu BERTRAND, Aline COELHO DE SOUZA, Liu FANYU, Hamza HALLAK ELWAN, Ziad ISKANDAR, Frédéric PARMENT, Habeb RZAIGUI, Ayssar SERHAN, Ekta SHARMA, Isaac SILVA , Vipin VELAYUDHAN, Furat ABAYAJE, Pierre BOUSSEAUD, Tapas DUTTA, Tong SHAO, and so on.

I would thank my best friend Ali ANSARINIK who lives far away from us.

Finally, I would thank my parents, Shanaz and Mohammad-Ali. You sacrificed your own happiness, just so that I could be happy. Mom and dad, you have been there day after day, to make sure my life turned out this way. Thank you.

Grenoble, 3 July 2015

R. Kh.

Abstract

This Ph.D. investigates the radio over fiber communication systems at mm-wave frequencies higher than 60 GHz. The thesis elaborates on three crucial issues in these systems including: phase noise measurement of unstable optically generated mm-wave signals, elimination of phase noise impact on performance of radio over fiber systems using non-coherent down conversion technique, and studying the amplitude noise impacts on performance of system based on these detectors. In the first part of this work, a new digital phase noise measurement technique is presented which is able to extract the phase noise of any unstable mm-wave optically generated signal. This technique is able to measure the phase noise for a wide range of offset frequencies from close-in phase noise to far noise floor by adapting frequency resolution of measurement and without considering small angle approximation. In the second part, we present a radio over fiber system at mm-wave frequency based on non-coherent electrical frequency down conversion stage using an envelope detector which is robust against phase and frequency fluctuations of the optically generated carrier signal. Finally, a theoretical and experimental study of amplitude noise impact on performance of radio over fiber systems based on non-coherent receivers is presented. In this study, a simulation technique based on theory is developed which is able to determine, among different optical and electrical noise, the one which has the dominant effect on EVM results. This simulation technique is based on observing the EVM evolution versus received optical power.

Key words: Radio over Fiber - Millimeter-wave - Phase noise - Amplitude noise - Envelope detector.

Résumé

Ces travaux de recherche portent sur les systèmes de communication radio-sur-fibre aux fréquences millimétriques supérieures à 60 GHz. Cette thèse s'articule autour de trois problématiques cruciales pour ces systèmes : la mesure du bruit de phase des signaux millimétriques instables générés par voie optique, la suppression de l'impact du bruit de phase sur les performances des systèmes de communications radio-sur-fibre par l'utilisation de techniques de conversion de fréquence non-cohérente, et enfin l'étude de l'impact du bruit d'intensité sur les performances des systèmes à détection non-cohérente. La première partie du travail présente une nouvelle technique de détection numérique du bruit de phase, capable de mesurer le bruit de phase à n'importe quelle fréquence millimétrique générée par voie optique et donc le plus souvent instable. Il est possible de mesurer le bruit de phase pour une large gamme de fréquences de décalage, allant de fréquence très proches de la porteuse à des bruits lointains grâce à l'adaptation de la résolution fréquentielle de la mesure. Cette mesure se fait de plus sans l'approximation des petits angles, très souvent utilisés. Dans la deuxième partie, un système de communication millimétrique basé sur une détection non-cohérente est étudié. L'étage de conversion de fréquences électrique permettant l'analyse des signaux est réalisé avec une détection d'enveloppe, ce qui permet de s'affranchir des variations de phase et de fréquence de la porteuse générée par voie optique. Pour terminer, des études théoriques et expérimentales sont menées sur l'impact du bruit d'amplitude sur les systèmes radio-sur-fibre utilisant ce type de détection non-cohérente. Les simulations, basées sur des modèles théoriques, sont capables de déterminer quel bruit est prédominant lors des mesures d'EVM parmi les bruits optiques et électriques. Cette technique s'appuie sur l'observation de l'évolution de l'EVM sur la puissance optique reçue.

Mots clefs : Radio sur Fibre - Fréquences millimétriques - Bruit de phase - Bruit d'amplitude - Détection d'enveloppe.

Contents

Acknowledgements	i
Abstract (English/Français)	iii
List of figures	ix
List of tables	xiii
Acronyms	1
1 State of the art of millimeter-wave Radio-over-Fiber communication systems	3
1.1 Introduction	3
1.1.1 Frequency allocation in different mm-wave regions	4
1.2 Overview of Radio-over-Fiber in the mm-wave region	7
1.2.1 Optical mm-wave generation	7
1.2.2 RoF architecture	14
1.2.3 RoF system state-of-the-art	16
1.3 Outline and aims of the thesis	17
2 Phase Noise Measurement of Unstable Optically Generated Millimeter-Wave signal	27
2.1 Introduction	27
2.1.1 What is the phase noise?	28
2.1.2 Phase noise spectrum	28
2.2 Phase noise measurement methods	31
2.2.1 Direct spectrum technique	31
2.2.2 Phase or frequency detection techniques	32
2.3 Phase noise measurement of optically generated carrier	35
2.3.1 Direct spectrum analyzer method	37
2.3.2 Digital approach	37
2.4 Conclusion	48
3 Impact of Phase Noise in RoF System Based on PMLLD	51
3.1 Introduction	51
3.2 Different down-conversion methods	51
3.2.1 Non-Coherent receiver	52

Contents

3.2.2	Coherent receiver	55
3.3	RoF based on PMLLD using coherent and non-coherent receivers at 60 GHz . .	57
3.3.1	Non-coherent receiver	57
3.3.2	Coherent receiver	62
3.3.3	Coherent and non coherent receiver, a comparison	63
3.4	RoF at W band based on non-coherent receiver	66
3.4.1	Experimental results	66
3.5	Conclusion	69
4	Impact of Amplitude Noise in Millimeter-Wave Radio over Fiber Systems	73
4.1	Introduction	73
4.2	Different amplitude noise in RoF systems	74
4.2.1	Relative intensity noise (RIN)	74
4.2.2	Shot noise	74
4.2.3	Thermal noise	75
4.3	Global SNR in RoF system based on two DFB lasers	75
4.4	Global SNR in RoF system based on PMLLD	78
4.5	EVM in an RoF system based on non-coherent receiver	83
4.5.1	Simulation of EVM behaviour versus received optical power	84
4.5.2	Experimental setup and results	87
4.6	Conclusion	92
5	Conclusions and Prospects	95
A	List of personal publications	97

List of Figures

1.1	Mm-wave atmospheric absorption [15].	4
1.2	Channelization of 802.15.3c around the global [70].	6
1.3	MM-wave generation using two independent lasers.	8
1.4	MM-wave generation using two lasers and optical phase locking (OPL), Amp: Amplifier, LPF: Low pass filter.	9
1.5	MM-wave generation using optical injection locking.	9
1.6	MM-wave generation using direct modulation technique.	10
1.7	MM-wave generation using EOM: electro-optical modulator.	11
1.8	MM-wave generation using cascade of MZM [33].	11
1.9	Simulation of electrical fields of five individual phase locked modes and the superposition result, E_{total}	12
1.10	Optical spectrum of the output signal of a mode locked laser.	12
1.11	MM-wave generation using an MLL.	13
1.12	RoF very simple topology.	14
1.13	Schematic highlighting Baseband-over-Fiber, IF-over-Fiber and Radio-over-Fiber system configurations.	15
2.1	Power spectral density (PSD) of the phase noise at baseband and at carrier frequency f_c	29
2.2	Different sources of the phase noise presented by SSB spectrum of phase fluctuations versus different offset frequencies.	30
2.3	Direct spectrum measurement technique, DUT: Device Under Test.	32
2.4	Balanced mixer as a phase detector, LPF: Low Pass Filter, ESA: Electrical Spectrum Analyzer.	33
2.5	Phase noise measurement using PLL and reference source, PLL: Phase locked loop, LPF: Low Pass Filter, LNA: Low Noise Amplifier, ESA: Electrical Spectrum Analyzer.	34
2.6	Phase noise measurement using delay line frequency discriminator, LPF: Low Pass Filter, LNA: Low Noise Amplifier, ESA: Electrical Spectrum Analyzer.	34
2.7	Phase noise measurement setup in RoF system based on PMLLD, LNA: Low Noise Amplifier, LO: Local Oscillator, ESA: Electrical Spectrum Analyzer, DSO: Digital Storage Oscilloscope.	36

List of Figures

2.8	Four phase noise measurement traces for the same laser using direct spectrum analyzer method.	37
2.9	Schematic of signal processing for frequency noise measurement.	39
2.10	RoF laser (PMLLD) testbench with dual lens focaliser and DC biasing using coplanar prob.	41
2.11	Different laser diodes measured phase noise using small angle approximation method, $L_c(f)$	43
2.12	Laser L872 phase noise result with frequency resolution of 20 Hz using small angle approximation method, $L_c(f)$	43
2.13	Laser L872 phase noise result with different frequency resolution of (A) 10 Hz, (B) 100 Hz, (C) 1 kHz, (D) 10 kHz.	44
2.14	Laser L872 phase noise result using two signal processing techniques, FM detection (black) and small angle approximation (grey).	45
2.15	Laser L872 phase noise results using digital technique (Black curve) and FSUP analyzer (Blue curve) [24].	46
2.16	Phase noise comparison between Laser L872 (curve (A)) and the LO (curve (B)).	47
3.1	Block diagram of simulated RoF system based on non-coherent receiver, MLLD: mode-locked laser diode, MZM: Mach-Zehnder modulator, PD: photo-diode, A: amplifier, ED: envelope detector, LPF: low pass filter (a) Optical spectrum of signal at output of laser. (b) Optical spectrum of signal at output of modulator. (c) Electrical spectrum of signal at output of PD.	52
3.2	Block diagram of RoF system based on MLLD and coherent receiver, LO: local oscillator.	55
3.3	Experimental set-up of RoF communication system based on non-coherent receiver and coherent receiver - PMLLD: passively mode-locked laser diode, PC: polarization controller, MZM: Mach-Zehnder Modulator, AWG: arbitrary waveform generator, SMF: single mode fiber, VOA: variable optical attenuator LO: local oscillator, DSO: digital storage oscilloscope.	57
3.4	Constellation diagram and power spectrum of the detected signal for RoF system based on PMLLD (L872) and non-coherent receiver (ED) at 60 GHz and intermediate frequency of 300 MHz. (I.a) QPSK data rate of 40 Mbps, EVM=5.4 %. (I.b) PSD, QPSK data rate of 40 Mbps. (II.a) QPSK data rate of 60 Mbps, EVM=5.5 %. (II.b) PSD, QPSK data rate of 60 Mbps. (III.a) QPSK data rate of 80 Mbps, EVM=5.6 %. (III.b) PSD, QPSK data rate of 80 Mbps.	59
3.5	Constellation diagram of the detected signal for RoF system based on PMLLD (L872) and non-coherent receiver at 60 GHz and intermediate frequency of 500 MHz. (a) QPSK data rate of 300 Mbps, EVM=12 %. (b) QPSK data rate of 400 Mbps, EVM=16 %.	60
3.6	Normalized output power of detector (DET-15) versus intermediate frequency	61
3.7	Measured eye diagram for OOK signal at (a) 100 Mbps (b) 300 Mbps (c) 500 Mbps and (d) 2.5 Gbps for the received optical power of -0.25 dBm.	62

3.8	Q factor versus received optical power for different bit rates using non-coherent receiver.	62
3.9	Constellation diagram and power spectrum of the detected signal for RoF system based on PMLLD (L872) and coherent receiver at 60 GHz and intermediate frequency of 1 GHz. (I.a) constellation diagram of signal without harmonics, QPSK data rate of 100 Mbps, EVM=11 %. (I.b) PSD, QPSK data rate of 100 Mbps. (II.a) constellation diagram of signal with harmonic at 2 GHz, QPSK data rate of 100 Mbps, EVM=20 %. (II.b) PSD with harmonic at 2 GHz, QPSK data rate of 100 Mbps.	63
3.10	EVM versus received optical power for both coherent and non-coherent receivers at 400 and 200 Mbps with QPSK modulation.	64
3.11	EVM versus SNR for simulation and experimental measurement results, for coherent receiver with data rate of 200 Mbps.	65
3.12	W-band RoF based on two DFBs and non-coherent receiver.	66
3.13	EVM versus received optical power for 16QAM modulation scheme in the RoF W-band system.	67
3.14	Eye diagram for different data rates (A) 100 Mbps (B) 400 Mbps (C) 1 Gbps (D) 2 Gbps.	68
4.1	Schematic of RoF communication system based on two DFB lasers and non-coherent receiver, MZM: Mach-Zehnder Modulator, PD: Photo diode, A: Amplifier, ED: Envelope detector	76
4.2	Schematic of RoF communication system based on PMLLD and non-coherent receiver, MZM: Mach-Zehnder Modulator, PD: Photo diode, A: Amplifier, ED: Envelope detector	78
4.3	EVM simulation results versus received optical power for different RIN values.	84
4.4	EVM simulation results versus received optical power for different noise figure values of the LNA.	85
4.5	EVM simulation results versus received optical power for different phase noise values.	86
4.6	Experimental setup of RoF communication system based on A) two DFB lasers B) PMLLD, TC: Temperature Controller, PC: Polarization Controller, MZM: Mach-Zehnder Modulator, AWG: Arbitrary Waveform Generator, SMF: Single Mode Fiber, VOA:Variable Optical Attenuator, LNA: Low Noise Amplifier.	87
4.7	Power spectrum of the received noise for RoF based on PMLLD and two DFB lasers.	88
4.8	Measurement and simulation results of EVM versus received optical power for RoF based on two DFBs	89
4.9	Measurement and simulation results of EVM versus received optical power for RoF based on PMLLD	90



List of Tables

3.1 EVM results versus Bit Rate for different scenarios	64
-------------------------------------------------------------------	----

Acronyms

ADC	Analogue to Digital Converter
AMP	Amplifier
AWG	Arbitrary Waveform Generator
BB	Base Band
BER	Bit Error Rate
BPSK	Binary Phase Shift Keying
CEPT	Conference of Postal and Telecommunication Administration
CS	Central Station
DC	Direct Current
DFB	Distributed Feed Back
DSB	Double Side Band
DSO	Digital Storage Oscilloscope
DUT	Device Under Test
ED	Envelope Detector
EIRP	Equivalent Isotropic Radiated Power
EOM	Electro Optical Modulator
ESA	Electrical Spectrum Analyzer
ESD	Electro Static Discharge
ETSI	European Telecommunication Standard Institute
EVM	Error Vector Magnitude
FCC	Federal Communication Commission
FEC	Forward Error Correction
FFT	Fast Fourier Transform
FM	Frequency Modulation
HDTV	High Definition TV
IF	Intermediate Frequency
IFoF	IF over Fiber
ITU	International Telecommunication Union
LNA	Low Noise Amplifier
LO	Local Oscillator
LPF	Low Pass Filter
MLL	Mode Locked Laser

List of Tables

MLLD	Mode Locked Laser Diode
MPHPT communication	Ministry of Public Management, Home Affairs, Post and Telecom-
MZM	Mach Zehnder Modulator
NF	Noise Figure
NTC	Negative Temperature Coefficient
OIL	Optical Injection Locking
OOFK	Optical Orthogonal Frequency Division Multiplexing
OOK	ON OFF Keying
OPL	Optical Phase Locking
OPLL	Optical Phase Locked Loop
PAPR	Peak to Average Power Ratio
PC	Polarization Controller
PD	Photo Detector/ Photo Diode
PLL	Phase Locked Loop
PM	Phase Modulation
PMLL	Passively Mode Locked Laser
PSD	Power Spectral Density
QPSK	Quadrature Phase Shift Keying
RF	Radio Frequency
RoF	Radio over Fiber
RIN	Relative Intensity Noise
SMF	Single Mode Fiber
SNR	Signal to Noise Ratio
SSB	Single Side Band
TC	Temperature Controller
VCO	Voltage Control Oscillator
VOA	Variable Optical Attenuator
VSA	Vector Signal Analyzer

1 State of the art of millimeter-wave Radio-over-Fiber communication systems

1.1 Introduction

Future networks need to provide data rates up to tens of gigabit per second in order to satisfy the new applications hunger for high data rate. Some of these recent applications are; the next generation high definition TV (HDTV) so-called ultrahigh definition TV, or UHD, the "sync and go" file wireless transfer which enables large amount of file transfer between mobile terminals and storage devices, 3D TVs, wireless gaming with ensured high-quality performance, and tera-bit medical video instantaneous data transfer using wireless link ([1], [2]). The key to transmitting high-data rate using wireless link is spectrum, since the demand for the data rate is directly translated to the demand for the available bandwidth. Thus, it is required to find unlicensed and suitable frequency bands over which we can run the ultra fast applications. The huge available bandwidth around millimeter wave (mm-wave) spectrum represents great feasibility of multi-gigabit per second wireless communications ([3]- [9]). On the other hand, there are some specific characteristics for mm-wave and Terahertz (THz) signals which make them interesting for military (mm-wave short range radars), security (mm-wave security scanner used in airports), astronomy (mm-wave radio telescope) and also spectroscopic applications ([12], [13]). Thus, future wireless communication systems will use new frequency carrier bands such as mm-wave and THz frequencies to overcome the saturation of the radio frequency bands in combination with very high bit rates.

Despite these advantages and needs for mm-wave signals, there are two main issues with communication systems at mm-wave frequencies: first, generation of these frequencies which is a challenging topic in electronics since lack of solid-state signal sources, rather than detectors, is considered as the obstacle to developing applications at mm-wave domain ([10], [11]), and the second main issue is delivery difficulties such as high atmospheric attenuation for wireless delivery [15], and high attenuation due to the skin effect for coaxial cable delivery (attenuation

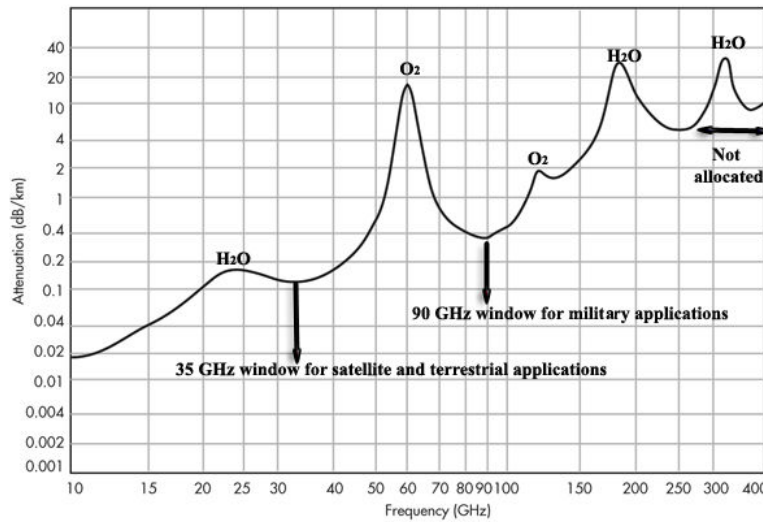


Figure 1.1 – Mm-wave atmospheric absorption [15].

of 5 to 10 dB per 1 meter at 60 GHz). These two matters have brought much attentions to the microwave-photonics based systems such as radio over fiber (RoF) communications systems. In RoF communication system, for generation of mm-wave signals photonic techniques are used which are superior to regular techniques based on electronics with respect to signal bandwidth. Moreover, the well known advantages of optical fiber such as low loss, light weight, large bandwidth, small size and low cable cost make the use of optical fiber a solution to the delivery problems of the mm-waves signal over long distances. During this thesis we have been targeting the RoF systems at mm-wave frequencies from different points of view with an emphasis on receiver side and so all of the efforts, investigations and explorations have been done towards this aim.

Remark: Strictly speaking, the term mm-wave refers to wavelengths less than 1 cm or frequencies higher than 30 GHz. However, in communication systems it is more usual to use mm-waves for frequencies higher than 55 GHz and the reason is that the globally available bands of 6-40 GHz, usually called microwave band, are fairly consistent in characteristics and are managed by the regulators around the world. However, the bands at frequencies higher than 55 GHz have different atmospheric propagation characteristics which make them be treated differently by the regulators, and it is there for more convenient to define them differently. Hereafter the term mm-waves refers to frequencies above 55 GHz until 200 GHz.

1.1.1 Frequency allocation in different mm-wave regions

The atmospheric absorption measurements at different frequencies have shown several frequency windows where radio-wave attenuation is minimized (Figure 1.1). These atmospheric windows are around: 35, 90, 140, 220 GHz [15]. However, few of these frequencies are available for commercial services, for example the frequencies around 35 GHz have already been used

for satellite and terrestrial communications, and the 90 GHz window has been reserved for military applications. The peak molecular absorption values which occur at 60, 119, 183, and 325 GHz are illustrated on Figure 1.1. The frequency gaps between the peak absorption values such as; 80, 140, and 220 GHz are proper candidate for broadband communications, however, not all these bands are available for commercial purposes.

Frequency band allocation strictly depends on the regulators of different countries. Furthermore, only few parts of spectrum are considered for unlicensed purposes. Hereafter a very short review of regulations and standards of mm-wave frequency bands in different countries is presented.

The 60 GHz and 70/80 GHz frequency bands are two of frequency bands that are of most use for high data rate applications in many countries. In the United States, the Federal Communication Commission (FCC) has allocated 57.05-64 GHz band for unlicensed operations. The predicted values for equivalent isotropic radiated power (EIRP) and maximum power to the antenna are limited to 43 and 27 dBm, respectively [17]. We need to mention that even though the maximum transmitted power is limited to 27 dBm, the actually transmitted power by the power amplifiers for 60 GHz is limited to 10 dBm [2]. In Japan, the Ministry of Public Management, Home Affairs, Post and Telecommunication (MPHPT) standardized the 59-66 GHz band in year 2000. Output power and antenna gain are constrained to 10 dBm and 47 dBi, respectively [18]. Ministry of information and Communication of Korea has introduced the 60 GHz band within 57-64 GHz for unlicensed operations, and a maximum transmitted power of 10 dBm and a maximum antenna gain of 17 dBi are regulated for indoor applications [19].

In Europe, the European Telecommunication Standard Institute (ETSI) and European Conference of Postal and Telecommunication Administrations (CEPT) are the organizations in charge of standardization and regulation of different frequency bands. Frequency bands regulation process in Europe is more complex as many countries are involved and many of them have already released their own preliminary standards. In general, the 59-66 GHz band is allocated for mobile services. For up-to-date information see [20].

Recently, many countries have considered the mm-wave frequencies above 70 GHz for ultra-high capacity point-to-point communications. According to International Telecommunication Union (ITU) radio regulations, the 71-76 GHz and 81-86 GHz bands are available for both fixed and mobile services. In the United States, the FCC licensed these two bands based on light licensing. The light licensing allows the users to register each path on a date in the database, and so the licenses will provide interference protection in a link-by-link bases and the priority goes to the date of link registration. Based on FCC regulation, the minimum antenna gain and maximum half-power beamwidth are 43 dBi and 1.2 degree, respectively and the maximum transmit power spectral density is set to 150 mW/100 MHz [21]. In November 2006, Office of Communication (Ofcom), the governmental regulator of communication systems in United Kingdom, opened the 71-76 GHz and 81-86 GHz frequency bands for point-to-point broadband fixed wireless systems on a light licensed basis. The recommended maximum EIRP

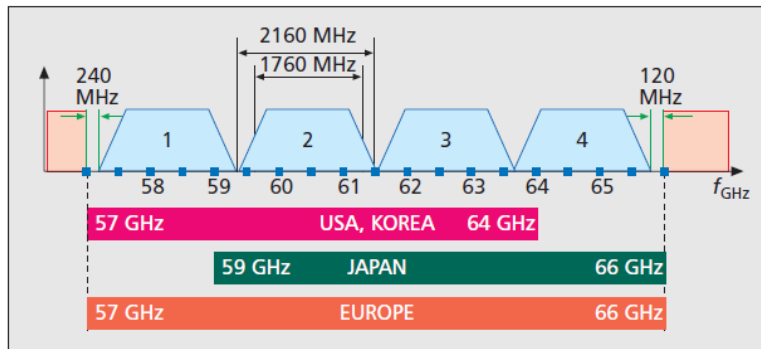


Figure 1.2 – Channelization of 802.15.3c around the global [70].

and maximum total output power at antenna port are 55 dBW and 0 dBW, respectively [22]. In Europe, the licensing and regulations of 70 and 80 GHz are depending on the countries regulators, for more information the reader is referred to [20].

Another frequency region that attracts much attentions recently is the spectrum higher than 275 GHz, which is not yet allocated to any specific application by the ITU. In particular, 300-500 GHz region attracted growing interest due to the recent progress in operation frequency of semiconductor devices.

1.1.1.1 IEEE 802.15.3c: The first IEEE wireless standard at mm-wave frequency

In September 2009, the first IEEE wireless standard in the 60-GHz band was approved by IEEE Standard Board as IEEE 802.15.3c [69]. A total of five usage models were accepted by the group, including: uncompressed video streaming¹, uncompressed multivideo streaming², office desktop³, conference ad hoc⁴, and kiosk file downloading⁵.

Channelization of IEEE 802.15.3c in 60 GHz band around the global presented in Figure 1.2. As can be seen in this figure, the 60 GHz band is divided into four channels of 2160 MHz. Devices in the United States can use channels 1-3, and those in Japan can use channels 2-4. The channels are large enough to support the data rate requires in the usage models with robust low-spectrum-efficiency modulation schemes. Lower and upper guard bands are also large enough (240 and 120 MHz) in order to minimize interference with other bands.

¹Large available bandwidth in the 60 GHz band enables sending HDTV signals which requires data rate of over 3.5 Gbps.

²In multivideo streaming, multiple video signals can be supplied by a single transmitter.

³Using office desktop, the personal computer can communicate with external computer peripherals.

⁴IEEE 802.15.3c can be used when many computers want to communicate with each other.

⁵In kiosk file downloading, the electronic devices can download the data such as video and games from an electronic kiosk at high data rate.

1.2 Overview of Radio-over-Fiber in the mm-wave region

Besides of benefiting unlicensed frequency bands of mm-wave region, thanks to low loss and large bandwidth of the optical fibers, RoF has attracted much attention as a solution to enlarge the coverage of the wireless mm-wave signal. Using this system in a cellular network, a large area can be covered utilizing micro-cells by means of low cost base stations (BS) which are linked to central station (CS) through optical fibers. In such a system, frequency limitation problems can be solved because many BSs can be installed, the zone radius can be reduced, and so the radio frequencies can be reused efficaciously in many radio zones without causing interference [16]. In this section, a brief overview of the RoF systems is presented, and we elaborate on the general aspects, issues and components of this communication system.

1.2.1 Optical mm-wave generation

A tunable mm-wave frequency can be generated by beating two or more optical waves on a photodetector (PD). The technique in which two or more signals of different frequencies are mixed in order to generate a third signal at the sum or difference frequency of the two original signals is called heterodyning. Equation 1.1 and 1.2 represent electric field of two optical waves:

$$E_1(t) = E_{01} \exp(j(\omega_1 t + \phi_1)) \quad (1.1)$$

and

$$E_2(t) = E_{02} \exp(j(\omega_2 t + \phi_2)) \quad (1.2)$$

where E_{01} and E_{02} are the amplitudes, ϕ_1 and ϕ_2 are the phase and ω_1 and ω_2 are the angular frequencies of two optical waves. The current at the output of a PD can be found as following:

$$\begin{aligned} I(t) &= RP_{opt} \\ I(t) &= R(E_1(t) + E_2(t))(E_1(t) + E_2(t))^* \\ &= R(|E_1(t)|^2 + E_1(t)E_2(t)^* + E_1(t)^*E_2(t) + |E_2(t)|^2) \\ &= R\left(E_{01}^2 + E_{01}E_{02} \exp(-j((\omega_2 - \omega_1)t + \phi_2 - \phi_1)) \right. \\ &\quad \left. + E_{01}E_{02} \exp(j((\omega_2 - \omega_1)t + \phi_2 - \phi_1)) + E_{02}^2\right) \quad (1.3) \end{aligned}$$

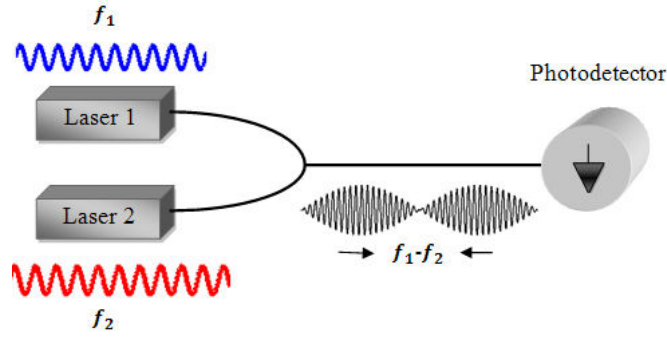


Figure 1.3 – MM-wave generation using two independent lasers.

where R and P_{opt} are the responsivity of the PD and the received optical power, respectively. Equation 1.3 can be simplified as:

$$I(t) = R \left(E_{01}^2 + E_{02}^2 + 2E_{01}E_{02} \cos((\omega_2 - \omega_1)t + \phi_2 - \phi_1) \right) \quad (1.4)$$

Equation 1.4 shows that using two optical modes, a microwave or mm-wave signal can be generated whose frequency is equal to the frequency difference between the two optical modes. On the other hand, 1.4 shows that the phase noise and frequency stability of the generated electrical mm-wave signal is strictly depending on the phase coherence between the optical signals. Using this technique one can generate electrical signal with a frequency up to THz. The only limit in this system is the PD bandwidth limitations [23].

The two optical modes in 1.1 and 1.2 can be generated using different techniques. In the following subsections, a short review of these techniques is presented.

1.2.1.1 Multiple laser sources

Optical heterodyning using two independent wavelength-tunable lasers is shown in Figure 1.3. The wavelength of the laser beam can be controlled using temperature controller. Therefore, by changing the temperature of the lasers, the frequency distance between the modes can be adjusted. The two optical modes are then coupled into an optical fiber to be transmitted to the PD. At the output of the PD the electrical signal with frequency equals to the frequency distance between the two optical modes can be generated, as it is shown in previous section. This method is the simplest and the most cost effective way to generate mm-waves. However, the frequency stability is very poor [24].

To generate low phase noise mm-wave signal, the phase of the two light sources are usually locked by implementing optical injection locking (OIL) ([25] and [26]) or by an optical phase-locked loop (OPLL) ([27]-[31]). Figure 1.4 presents the schematics of an mm-wave generation technique based on two lasers and an OPLL. The optical microwave carrier output is generated

1.2. Overview of Radio-over-Fiber in the mm-wave region

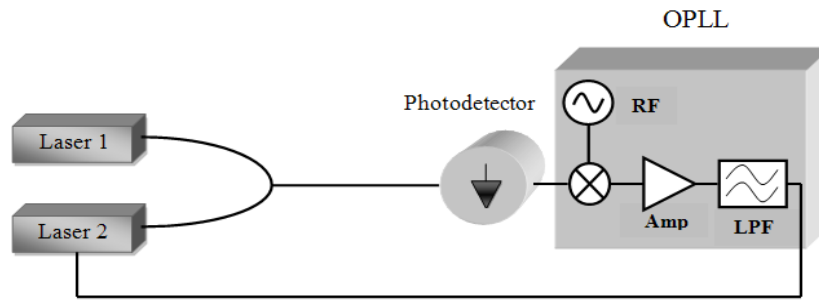


Figure 1.4 – MM-wave generation using two lasers and optical phase locking (OPL), Amp: Amplifier, LPF: Low pass filter.

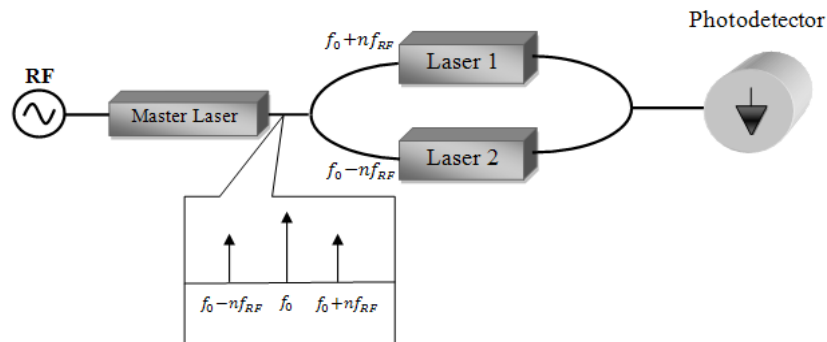


Figure 1.5 – MM-wave generation using optical injection locking.

from the beating between the two lasers optical modes in a PD. The resulting mm-wave signal is then amplified and mixed with the reference signal from the local oscillator (LO) by an RF mixer. The resulting phase error signal is used to tune the frequency of the laser 2, forcing it to track the master laser with a frequency offset equals the desired RF frequency. Using OPLL can significantly reduce the phase noise of the generated mm-wave signal [30]. However, the disadvantages of this technique are the high complexity of the whole setup and need of a pure LO signal at the receiver. The block diagram of OIL technique is shown in Figure 1.5. In this technique, a master laser is modulated directly using an RF source. Consequently, multiple side bands appear around the central wavelength at the output of the master laser. This signal in turn will be injected into the two slave lasers, and then the wavelength of the two lasers are chosen to be near the n th order side band, so that the two slave lasers are locked at the mentioned frequencies. The OIL suppresses the phase noise of the generated mm-wave signal and allows to use low frequency signals as a reference source. However, OIL allows a small detuning range and exhibits a comparatively high complexity.

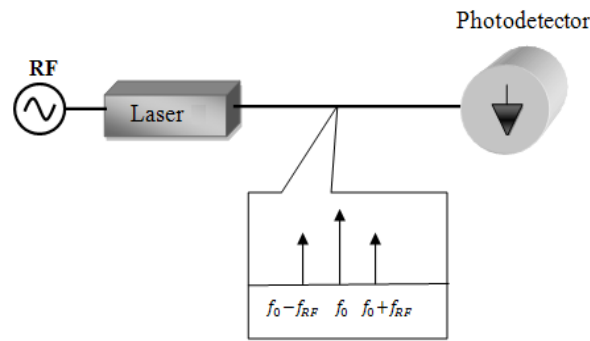


Figure 1.6 – MM-wave generation using direct modulation technique.

1.2.1.2 Modulation techniques

Using modulation techniques is another method for mm-wave generation. The modulation can be done directly or using an external modulator. In the direct modulation technique, the bias current of the laser is modulated using a stable RF signal, thus two optical phase locked side bands will be generated at the output of the laser (see Figure 1.6). The phase noise of the generated mm-wave signal is directly related to the quality of the applied RF source. This technique is widely used in baseband optical transmission benefiting from the simple configuration. However, the bandwidth of this technique is limited to 10 GHz which is not enough for mm-wave generation. An alternative approach in order to increase the bandwidth of modulation is to use external electro-optical modulators (EOM) like Mach-Zehnder modulators (MZM), as it is shown in Figure 1.7. Using these modulators, one can achieve considerably higher modulation bandwidth up to 40 GHz [38]. Utilizing external optical modulation technique to generate mm-wave signal was first presented in [29]. In this work, a frequency doubled electrical signal was generated by biasing an MZM to suppress the even-order optical side bands. Another similar work based on quadratic response of an optical intensity modulator to generate a 60 GHz mm-wave presented in [44]. In this technique, the optical carrier, the first and third-order optical side bands were suppressed by adjusting the drive signal level. An approach using an optical phase modulator is reported in [45]. In this approach, a Fabry-Perot filter was used to select the two second order optical side bands. By beating these two second-order side bands in a PD an electrical signal of 60 GHz frequency was achieved. However, since these approaches require tunable optical filters to select the second order side bands, thus the complexity and the cost of the system increase significantly.

The optical mm-wave generation implementing cascaded of EOMs is well studied in ([32]-[34]). The schematic of the method presented in [33] is shown in Figure 1.8. In this figure, an MZM driven by 30 GHz RF oscillator is implemented for generation of two optical modes at the frequency distance of 60 GHz. Then, the two modes are modulated with digital signal using the second MZM driven by the baseband data stream. The broadband signal at 60 GHz frequency is generated after beating the two digitally modulated optical tones. However, this technique only supports on off keying (OOK) 60 GHz signal due to the beating of two digitally

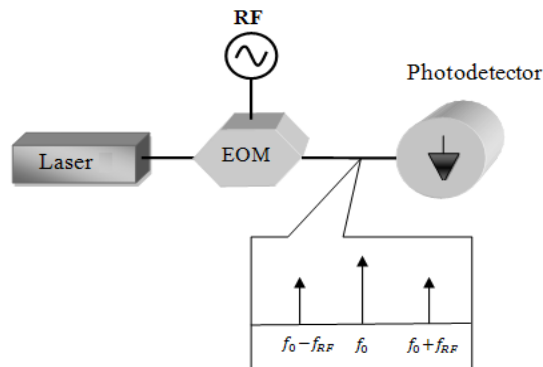


Figure 1.7 – MM-wave generation using EOM: electro-optical modulator.

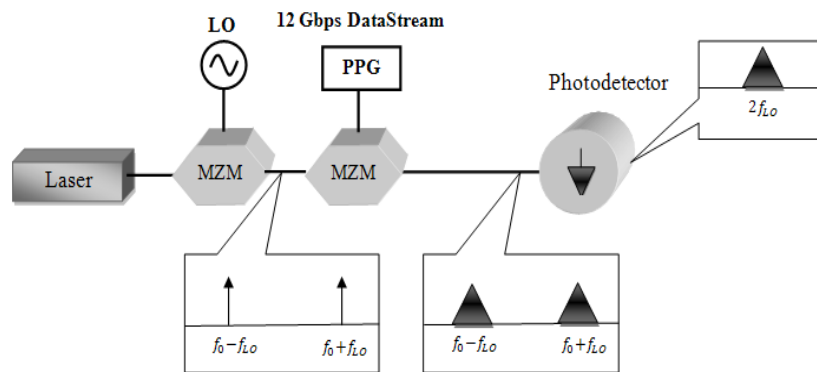


Figure 1.8 – MM-wave generation using cascade of MZM [33].

modulated optical tones .

1.2.1.3 Mode-locked laser diode

Mode-locking refers to the methods in which the lasers are used to obtain the ultrashort pulses, which are then called the mode-locked lasers (MLL) [35]. The phase of different electrical fields of an MLL only differ by a constant phase shift. Thus, at the output of the laser, the pulses are generated and the time distance between the pulses is constant. Figure 1.9 shows the electrical fields of five individual phase locked modes and the total electrical field obtained by superposition of the modes. Observing this figure, it can be seen that at the time when the modes are all in phase, red windows, the peak pulses appear. In this figure the frequency distance between the modes is fixed at 60 GHz. This separation in optical frequency corresponds to the pulse repetition frequency, f_r , of the laser which can be adjusted during laser fabrication. The optical spectrum of a pulse train, as generated in an MLL, consists of discrete lines with an exactly constant spacing which equals the repetition frequency. The optical spectrum simulation of the output signal of an MLL is presented in Figure 1.10, the laser consists of ten modes with the repetition frequency of 60 GHz.

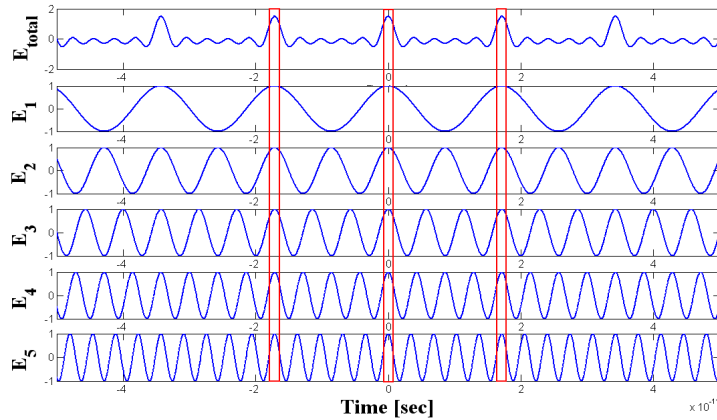


Figure 1.9 – Simulation of electrical fields of five individual phase locked modes and the superposition result, E_{total} .

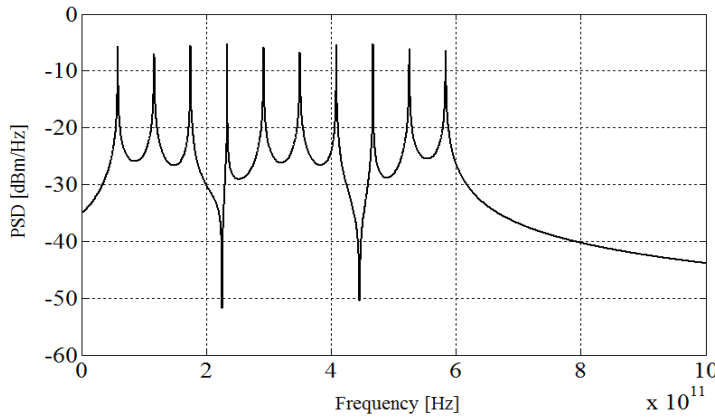


Figure 1.10 – Optical spectrum of the output signal of a mode locked laser.

In practice, the mode locking can be achieved using two different techniques; active mode locking and passively mode locking. In active mode locking, a very fast shutter is placed inside the laser cavity. The shutter opens every time light pulse makes a round-trip inside the laser cavity. This active modulation can be achieved with different kinds of electro-optical or acousto-optical modulators placed inside the laser cavity ([36] and [37]).

The passive mode locking method can be achieved by incorporating a saturable absorber¹ with suitable properties into the laser resonator along with a gain section. On the starting of the laser emission, the laser oscillates in noisy burst, as the modes have random phase. If one of these burst has enough energy to saturate the absorber, it will bleach the absorption and a net gain value occurs. The peak of the burst will experience low losses while the low-power trailing see more losses. As the energy burst travels back and forth, it is further shortened by

¹A saturable absorber is an optical component with a certain optical loss, which is reduced at high optical intensities. This can occur, e.g., in a medium with absorbing dopant ions, when a strong optical intensity leads to depletion of the ground state of these ions.

1.2. Overview of Radio-over-Fiber in the mm-wave region

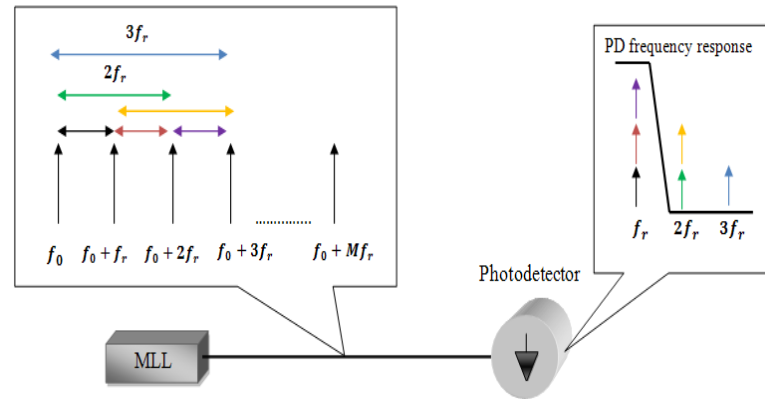


Figure 1.11 – MM-wave generation using an MLL.

the saturable absorption until the steady state is reached and the laser starts emitting a train of mode-locked pulses. The technique of passive mode locking allows the generation of much shorter pulses comparing to the active mode locking method, because a saturable absorber, driven by already very short pulses, can modulate the resonator losses much faster than any electronic modulator [43].

Observing the optical power spectrum of an MLL presented in Figure 1.10, it can be noticed that, one can generate mm-wave signals by heterodyning of the modes generated by this laser. Figure 1.11 shows the block diagram of mm-wave generation using an MLL. There are M modes at the output of the laser and the frequency distance between the adjacent modes is fixed and equals laser repetition frequency, f_r . Beating among different modes will generate different carrier frequencies at the output of the PD which are equal to the multiples of the laser repetition frequency ($n \times f_r$, $n = 1, 2, \dots$). However, because of the limited bandwidth of the PD, the frequencies higher than f_r will be filtered out, as illustrated in Figure 1.11.

Considering the advantages of the mm-wave generation technique based on MLL diode (MLLD) such as:

- Providing a large comb spectrum of phase locked optical modes just by using a laser diode at the transmitter.
- Simple up-conversion and modulation using DC bias.
- Lower phase noise in comparison with the techniques based on two free running lasers⁶.

It can be concluded that the RoF system based on MLLD provides much less complex and low cost configuration comparing to other techniques.

⁶Since in MLLD, the modes are generated in the same cavity, the phase correlation between the modes is better than using two free running laser sources.

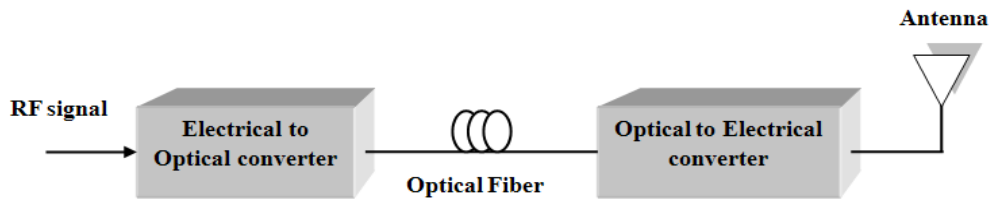


Figure 1.12 – RoF very simple topology.

The very first use of active MLL in mm-wave range is reported in [39], where the authors demonstrated transmission of 155 Mbps over 3 km of dispersion-shifted fiber. The first experimental demonstration of RoF based on passively mode locked quantum dash laser with data rate of 3.03 Gbps is presented in [40], and direct and external modulation setups are presented in [41] and [42].

The major part of theoretical and experimental studies on RoF systems presented in this thesis is based on using passively MLLD for mm-wave generation. III-V laboratory provided IMEP-LAHC laboratory with these lasers in order to be tested and characterized for future use in RoF communication systems.

1.2.2 RoF architecture

The main objectives of RoF system are the transport and distribution of wireless signals over optical fiber from a CS to different BSs, and delivery of RF signal from BSs to the mobile stations through wireless link. Thus, the fundamental elements of an RoF system are the components which are able to transform radio signal to optical wave and, vice versa. Figure 1.12 represents a very basic block diagram of a point to point RoF system. The RF electrical signal is transformed to optical domain using an electrical to optical converter (E/O) at the CS, and then the optical signal propagates through optical fiber to the BS. At the BS the signal is converted back to electrical domain using an optical to electrical converter (O/E) to be propagated through antenna towards the mobile stations.

Instead of RF signal, it is possible to use the baseband and intermediate frequency (IF) signals, in these cases, the system will be called baseband-over-Fiber and IF-over-Fiber (IFoF) communication systems. Figure 1.13 depicts a detailed configuration of RoF communication system for downlink⁷, and IFoF and baseband-over-Fiber systems for uplink⁸.

As illustrated in Figure 1.13 in RoF system, at the CS the baseband (BB) signal is frequency up-converted to corresponding RF frequency using an up-conversion stage, and then the electrical signal is transformed to optical signal using an E/O converter. The E/O converter is simply a light source like a monomode or multimode laser. The laser can be directly modulated by the RF signal in order to locate the RF signal on the intensity of the light, in this way the RF

⁷ traffic from the network to the user.

⁸ traffic from the user to the network.

1.2. Overview of Radio-over-Fiber in the mm-wave region

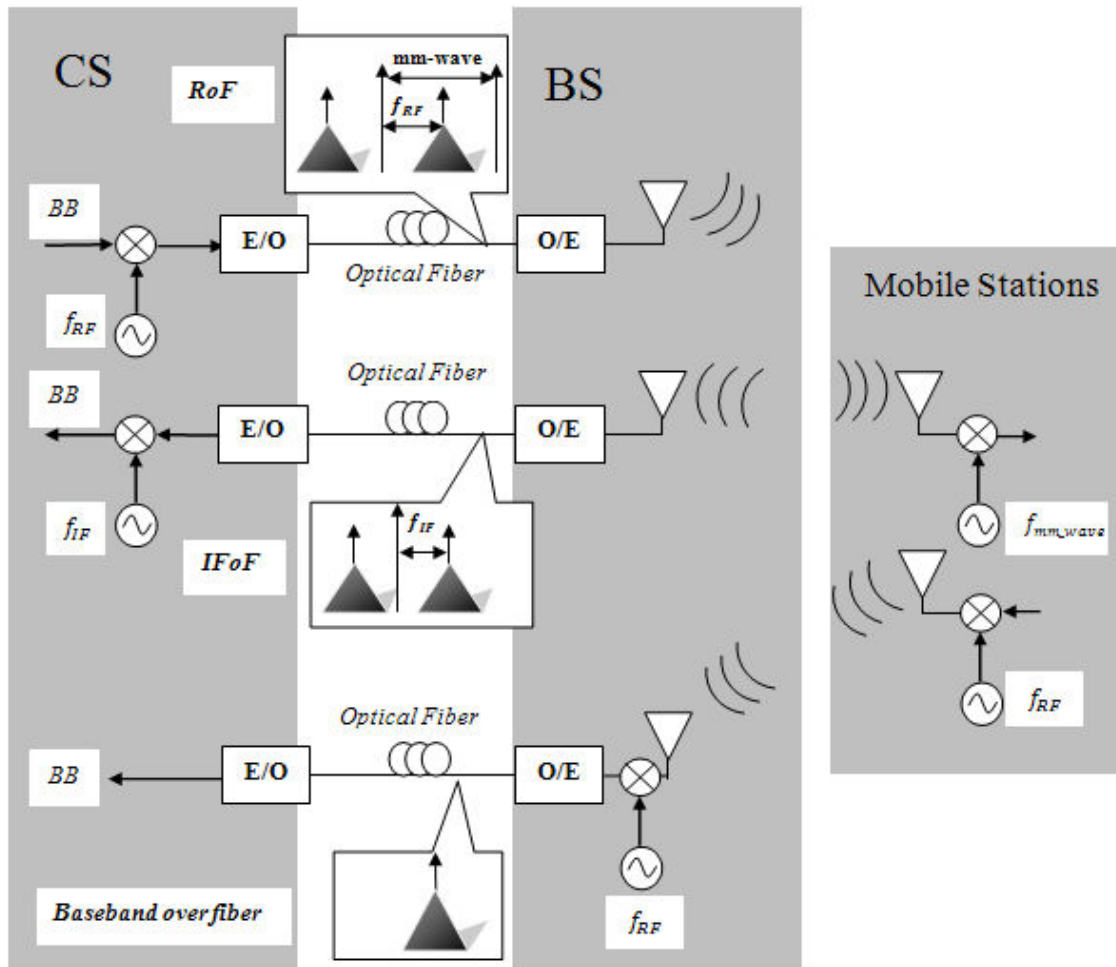


Figure 1.13 – Schematic highlighting Baseband-over-Fiber, IF-over-Fiber and Radio-over-Fiber system configurations.

signal is carried by an optical carrier. The modulated light is then transported through optical fiber to the BS accompanied by one or more optical modes, in such a way that the frequency distance between the two consecutive modes is fixed to mm-wave frequency range. At the BS, the received optical signal is transformed to electrical signal using an O/E converter which is a fast PD.

The PD plays two essential roles; conversion of the optical signal to electrical domain ,and mm-wave generation using heterodying technique. The frequency beating at the PD generates the BB signal and the signals at RF and mm-wave frequencies. The data is then transmitted to mobile stations through wireless link at mm-wave frequency. For the uplink connection, assuming that a high data rate communication is not required, then the wireless communication can be done at microwave frequency so that IFoF and baseband-over-fiber systems can be considered as more cost effective solutions, since the light source is not required to

have modulation bandwidth at high frequency range. In IFoF scheme, the IF signal after being transformed to electrical domain will be down-converted to the BB by a down-conversion stage at the CS. In this configuration an asymmetric communication system is considered. In the baseband-over-fiber configuration, the RF received signal is down-converted to baseband, and then transmitted to the CS through optical fiber.

1.2.3 RoF system state-of-the-art

The very first RoF system demonstration was done in 1990, a four channel cordless telephony signal transmitted over single mode fiber using subcarrier multiplexing. The demonstrated data rate for one channel was 72 kbps at an RF frequency of 0.86 GHz using binary frequency shift keying (BFSK) modulation scheme [47]. After that, many papers reported RoF systems using wavelength division multiplexing and subcarrier multiplexing [48, 49]. Many RoF systems based on intensity modulation of laser, direct or external modulations, have been also presented (see section 2.1.2 of this chapter). In these systems, three different transmission schemes can be used. First, double side band (DSB) transmission in which the data is modulated onto an optical RF carrier, thus creating two sidebands, upper optical sideband and lower optical sideband. The main drawback in this scheme is the chromatic dispersion which dramatically limits the length of optical fiber due to power fading effects [50, 51, 52]. In order to reduce the chromatic dispersion effects, various systems have been presented with suppressed optical carrier (DSB-CS), which reduce the limits of the optical fiber length [53, 54, 55]. For further improve of the tolerance to chromatic dispersion, some papers suggested the optical single-side band (SSB) transmission scheme, using which the complexity of the system will be increased [56, 57].

In 1995, an optical transmission over 400 m of single-mode fiber of two simultaneous 2.5 Mbps binary phase shift keying (BPSK) channels centered at a subcarrier frequency of 41 GHz was demonstrated using resonant modulation of monolithic semiconductor lasers [58]. From the first RoF systems at 60 GHz carrier frequency we can mention [51], in which transmission of a 120 Mbps quadrature phase shift keying (QPSK) signal over a fiber span of 13 km and a radio path of 5 m was demonstrated. Wireless data transmission at 10.6 Gbps using OOK modulation scheme on a 94 GHz carrier is achieved in 2008 in [59], mm-wave wireless signals are measured out to a distance of 800 m. In [60], the authors presented a 120-GHz-band wireless link that uses mm-wave photonic techniques. This system achieved error-free transmission of 10 Gbps OOK signals over a distance of more than 200 m with a received power of below -30 dBm. A scalable high-speed W-band (75-110-GHz) fiber wireless communication system using an optical frequency comb generator presented in [61]. In this paper, three channels of 8.3 Gbps optical orthogonal frequency-division-multiplexing (OOFDM) baseband signals were translated from the optical to the wireless domain using an optical frequency comb generator and the mm-wave carrier was generated by heterodyne mixing of OOFDM baseband signal with a free running laser. A tunable ultra-narrow linewidth (< 1 Hz) mm-wave and THz waves generation method based on femtosecond frequency comb MLL is reported in 2013 in [62]. In

this work, the 100 GHz carrier frequency was modulated at 40 Gbps OOK modulation. In [63], a 240 GHz optical mm-wave signal with very narrow linewidth ($< 10\text{Hz}$) was generated using an active MLL diode integrated with an electro-absorption modulator and also a fiber-radio transmission of 3 Gbps OOK data at 240 GHz is demonstrated.

In THz frequency domain, theoretical study of transmission characteristics in indoor short range communications at 350 GHz is well studied in [64] published in 2012. The authors employed a simulation environment considering realistic propagation conditions and system parameters in order to analyze the performance of future multigigabit indoor communication systems at THz frequencies. The transmitter position for optimal signal coverage, and influence of high-gain antennas on transmission aspects are investigated in this paper.

To generate signals at 300-400 GHz with photonics techniques, high-frequency PD is a key device [65]. A high-output-power photomixer module operating at 200 - 500 GHz has been developed in Japan, the module consists of a uni-traveling-carrier PD, a PD-waveguide mode-conversion coupler, and a compact metal package with a rectangular-waveguide that outputs sub-terahertz wave. The fabricated module exhibits a 10 dB down bandwidth of about 300 GHz and an output power as high as -2.7dBm at 350 GHz [66]. In [67], a fiber-wireless system in frequency range of 300-400 GHz is demonstrated using a uni-traveling-carrier PD (UTC-PD) and an error free transmission up to 2 Gbps has been obtained at 300 GHz. The main features of this research are that the carrier frequency is widely tunable, and the bit rate can be increased to at least 40 Gbps. At the receiver side, a Schottky barrier diode (SBD) is used to down-convert THz frequencies to IF in order to remove the phase noise impacts on the performance of received signal. Later in 2013, an RoF system proposed in [68] in which 18.6 Gbps QPSK data transmission at 100 GHz and 300 GHz carrier frequencies with 7% forward error correction (FEC) overhead is demonstrated. In that paper, signal generation is done using an optical frequency comb source and at the receiver an LO and a mixer at 100 GHz and 300 GHz are used in order to down-convert the mm-wave signal to IF.

1.3 Outline and aims of the thesis

The thesis presented herein explored the main issues of high speed RoF communication systems based on PMLLD in 55-110 GHz band. Several aspects of this system in 60 GHz band have been studied previously. Some of these recent studies are as follows: in [71] the authors presented a low-cost solution for RoF based on PMLLD, properties of mm-wave signal generation and modulation using PMLLD are studied in [72], chromatic dispersion in RoF systems based on PMLLD is well observed by the authors of [73], in [74] a method based on optical heterodyning is suggested in order to reduce the chromatic dispersion in RoF systems based on PMLLD, and the stabilization of the mm-wave carrier generated by PMLLD in RoF systems is explored in [75]. However, a number of aspects have remained uncovered such as: the phase and amplitude noise in RoF systems based on PMLLD and their impacts on different down-conversion methods, and also the impact of non-linearity of optical fiber on

Chapter 1. State of the art of millimeter-wave Radio-over-Fiber communication systems

chromatic dispersion as a compensating method in such communication systems. In this thesis, we have tried to cover these aspects in following chapters.

In **Chapter 2**, the phase noise in RoF system based on PMLLD is studied, and a time sampling and signal processing method is proposed in order to measure the phase noise of the generated mm-wave carrier in such a system. We could overcome the difficulties of measuring the phase noise of a PMLLD output signal, due to its frequency instability, by replacing a spectrum analyzer with a digital storage oscilloscope. For the first time, a mathematical approach based on frequency demodulation is used to extract the phase noise of the mm-wave carrier without considering any small signal approximation to separate the phase noise and the amplitude noise.

In **Chapter 3**, the impact of phase noise of PMLLD on two different types of receiver is studied; Firstly, the coherent receiver with electrical coherent down-conversion stage using a mixer and an LO, secondly, the non-coherent receiver with electrical non-coherent down-conversion stage using an envelope detector. Although some methods have been demonstrated to stabilize RF signal for the communication system based on PMLLD, in this chapter, it is shown that using a non-coherent receiver at the receiver side, one can overcome the phase fluctuations caused by PMLLD.

Chapter 4 is dedicated to study of amplitude noise in an RoF system based on two DFB lasers and PMLLD. A complete theoretical and experimental study of amplitude noise impact on performance of RoF communication system at mm-wave is presented. A simulation method is also presented that is able to determine the origin of the amplitude noise which has the most impact on error vector magnitude (EVM). This method is based on analyzing the trends of EVM versus received optical power graph. The impact of different optical and electrical noise such as relative intensity noise (RIN), shot noise and thermal noise on EVM is precisely studied employing experimental and theoretical analysis. Impact of optical sources phase noise on performance of the system is removed using a non-coherent down-conversion method based on envelope detector. Using this method, a very good matching between the experimental and the simulation results is observed.

In **Chapter 5**, the results of this thesis are summarized and the perspective of the possible future works are presented.

Bibliography

- [1] T. Kleine-Ostmann and T. Nagatsuma, "A Review on Terahertz Communications Research," *J. Infrared Milli Terahz Waves*, Vol. 32, pp. 143-171, Feb. 2011.
- [2] P. X. a. A. V. Su-Khiong Yong, "60 GHz Technology for Gbps WLAN and WPAN: From Theory to Practice," John Wiley & Sons, Ltd, 2011.
- [3] N. Guo, R. C. Qiu, S. S. Mo, and K. Takahashi, "60-GHZ Millimeter-Wave Radio: Principle, Technology, and New Results," *EURASIP J. Wireless Commun. and Netw.*, vol. 2007, pp. 48-48, 2007.
- [4] H. Chen, R. Lin and J. Ye, "Millimeter-wave Radio over Fiber System for Broadband wireless communication," *Microwave and Millimeter Wave Technologies Modern UWB antennas and equipment*, March 2010.
- [5] J. Wells, "Faster Than Fiber: The Future of Multi-Gb/s Wireless," *IEEE Microw. Mag.*, vol. 10, pp. 104-112, May 2009.
- [6] A. Kanno, T. Kuri, I. Hosako, T. Kawanishi, Y. Yasumura, Y. Yoshida and K. Kitayama, "100-GHz and 300-GHz coherent radio-over-fiber transmission using optical frequency comb source," *Broadband Access Communication Technologies VII, Proc. of SPIE*, vol. 8645, Feb. 2013.
- [7] X. Pang, A. Caballero, A. Dogadaev, V. Arlunno, L. Deng, R. Borkowski, J. S. Pedersen, D. Zibar, X. Yu and I. T. Monroy, "25 Gbit/s QPSK Hybrid Fiber-Wireless Transmission in the W-Band (75–110 GHz) With Remote Antenna Unit for In-Building Wireless Networks," *IEEE Photon. J.*, vol. 4, pp. 691-698, June 2012.
- [8] L. Deng, M. Beltrán, X. Pang, X. Zhang, V. Arlunno, Y. Zhao, A. Caballero, A. Dogadaev, X. Yu, R. Llorente, D. Liu and I. T. Monroy, "Fiber Wireless Transmission of 8.3-Gb/s/ch QPSK-OFDM Signals in 75–110-GHz Band," *IEEE Photon. Technol. Lett.*, vol. 24, pp. 383-385, March 2012.
- [9] O. Omomukuyo, M. P. Thakur and J. E. Mitchell, "Simple 60-GHz MB-OFDM Ultrawide-band RoF System Based on Remote Heterodyning," *IEEE Photon. Technol. Lett.*, vol. 25, pp. 268-271, Feb. 2013.

Bibliography

- [10] A. El Oualkadi, "Trends and Challenges in CMOS Design for Emerging 60 GHz WPAN Applications," *Advanced Trends in Wireless Communications*, In Tech, Feb. 2011.
- [11] C. Mann, "Practical challenges for the commercialization of terahertz electronics," in *Proc. IEEE MTT-S Int. Microwave Symp.*, Honolulu, pp. 1705–1708, June 2007.
- [12] W. L. Chan, J. Deibel, and D. Mittleman, "Imaging with terahertz radiation," *Rep. Prog. Phys.*, vol. 70, pp. 1325–1379, July 2007.
- [13] H. B. Liu, H. Zhong, N. Karpowicz, Y. Chen, and X.-C. Zhang, "Terahertz spectroscopy and imaging for defence and security applications," *Proc. IEEE*, vol. 95, no. 8, pp. 1514–1527, Aug. 2007.
- [14] T. Nagatsuma, "Generating millimeter and terahertz waves," *IEEE Microw. Mag.*, vol. 10, pp. 64–74, June 2009.
- [15] *Attenuation by Atmospheric Gases*, ITU-R Standard P.676-6, 2005.
- [16] E. Dahlman, B. Gudmundson, M. Nilsson, A. Skold "UMTS/IMT-2000 based on wideband CDMA," *IEEE Commun. Mag.*, vol. 36, pp. 70–80, Sep. 1998.
- [17] *Code of Federal Regulation, Telecommunication*, title 47, chapter 1, part 15.255, Federal Communication Commission Std., 2004.
- [18] *Regulations for enforcement of the radio law 6-4-2 specified low power radio station (11) 59-66 GHz band*, Ministry of Public Management, Home Affairs, Posts and Telecommunication, Japan Std., 2000.
- [19] "Frequency allocation comment of 60 GHz band," Ministry of Information and Communication of Korea, Tech. Rep., 2006.
- [20] European Radiocommunications Office. Website. <http://www.ero.dk>. Online; accessed 19-Sep-2012.
- [21] FCC 03-248, "Allocation and services rules for the 71-76 GHz, 81-86 GHz and 92–95 GHz Bands," federal communication commission Nov. 2003.
- [22] Ofcom, "Making spectrum available for 71-76 and 81-86 GHz bands," Nov. 2006.
- [23] J. Yao, "A tutorial on microwave photonics," *IEEE Photon. Soc. Newsletter*, pp. 4–12, April 2012.
- [24] A. Hirata, M. Harada, K. Sato, and T. Nagatsuma, "Low-cost millimeter-wave photonic techniques for Gigabit/s wireless link," *IEICE Trans. Electron.*, vol. E86-C, no. 8, pp. 1296–1300, Aug. 1997.
- [25] J. Genest, et al., "Microwave signals generated by optical heterodyne between injection-locked semiconductor lasers," *Quantum Electron.*, *IEEE Journal of*, vol. 33, pp. 989–998, 1997.

- [26] L. Goldberg, et al., "Microwave signal generation with injection-locked laser diodes," *Electron. Lett.*, vol. 19, pp. 491-493, 1983.
- [27] Z. C. F. Fan and M. Dagenais, "Optical generation of a megahertz-linewidth microwave signal using semiconductor lasers and a discriminator-aided phase-locked loop," *IEEE Trans. Microw. Theory Techn.*, vol. 45, pp. 1296-1300, Aug 1997.
- [28] K. J. Williams, et al., "6-34 GHz offset phase-locking of Nd:YAG 1319 nm nonplanar ring lasers," *Electron. Lett.*, vol. 25, pp. 1242-1243, 1989.
- [29] J. J. O'Reilly, et al., "Optical generation of very narrow linewidth millimetre wave signals," *Electron. Lett.*, vol. 28, pp. 2309-2311, 1992.
- [30] L. N. Langley, et al., "Optical phase locked loop (OPLL) module for use as a 9 GHz source in phased array communications antennas," *International Topical Meeting on Microwave Photonics*, 1998, pp. 141-142.
- [31] S. Takasaka, et al., "External Synchronization of 160-GHz Optical Beat Signal by Optical Phase-Locked Loop Technique," *IEEE Photon. Technol. Lett.*, vol. 18, pp. 2457-2459, 2006.
- [32] Z. Ye, et al., "Photonic Generation of M-QAM/M-ASK Signals at Microwave/Millimeter-Wave Band Using Dual-Drive Mach-Zehnder Modulators With Unequal Amplitudes," *IEEE J. Lightw. Technol.*, vol. 26, pp. 2604-2610, 2008.
- [33] M. Weiss, et al., "60GHz radio-over-fibre wireless system for bridging 10Gb/s ethernet links," in *Optical Communication, 34th European Conference on*, 2008, pp. 1-2.
- [34] G. H. Nguyen, et al., "Generation of 60-GHz MB-OFDM Signal-Over-Fiber by Up-Conversion Using Cascaded External Modulators," *IEEE J. Lightw. Technol.*, vol. 27, pp. 1496-1502, Jun 2009.
- [35] EX. Kärtner, U. Morgner, T. Schibli, R. Ell, H.A. Haus, J.G. Fujimoto, and E.P. Ippen., "Few-cycle laser pulse generation and its applications," chapter *Fewcycle pulses directly from a laser*, pages 73–135. *Topics in Applied Physics*. Springer Berlin, 2004.
- [36] L. E. Hargrove, R. L. Fork, and M. A. Pollack, "Locking of He-Ne laser modes induced by synchronous intracavity modulation," *Appl. Phys. Lett.*, vol. 5, pp.4-5, July 1964. (first report of active mode locking)
- [37] H. A. Haus, "A theory of forced mode locking," *IEEE J. Quantum Electron.*, vol. 11, pp. 323-330, July 1975.
- [38] J. Yu, Z. Jia, L. Yi, Y. Su, G. Chang, and T. Wang, "Optical millimeter-wave generation or up-conversion using external modulators," *IEEE Photon. Technol. Lett.*, vol. 18, pp. 265-267, Dec. 2005.

Bibliography

- [39] R.P. Braun, G. Grosskopf, C.H. von Helmlolt, K. Kruger, U. Kruger, D. Rohde, and F. Schmidt, "Optical microwave generation and transmission experiments in the 12 and 60 GHz-region for wireless communications," *Microwave Symposium Digest, 1996.*, IEEE MTT-S International, vol.2, pp. 499 – 501, Jun 1996.
- [40] B. Charbonnier, P. Chanclou, J. L. Corral, G. H. Duan, C. Gonzalez, M. Huchard, D. Jäger, F. Lelarge, J. Marti, L. Naglic, L. Pavlovic, V. Polo, R. Sambaraju, A. Steffan, A. Stöhr, M. Thual, A. Umbach, F. Van Dijk, M. Vidmar, and M. Weiss, "Photonics for broadband radio communications at 60 GHz in access and home networks," In *International Topical Meeting on Microwave Photonics (MWP)/ Asia-Pacific Microwave Photonics Conference (APMP)*, Gold Coast, Australia, 2008.
- [41] M. Huchard, P. Chanclou, B. Charbonnier, F. van Dijk, G.H. Duan, C. Gonzalez, F. Lelarge, M. Thual, M. Weiss, and A. Stohr, "60 GHz radio signal up-conversion and transport using a directly modulated mode-locked laser. In *International Topical Meeting on Microwave Photonics (MWP)/ Asia-Pacific Microwave Photonics Conference (APMP)*, Gold Coast, Australia, Oct 2008.
- [42] M. Huchard, B. Charbonnier, P. Chanclou, F. Van Dijk, F. Lelarge, G.H. Duan, C. Gonzalez, and M. Thual, "Millimeter-wave photonic up-conversion based on a 55 GHz quantum dashed mode-locked laser," In *34th European Conference and Exhibition on Optical Communication (ECOC)*, Brussels, Belgium, Sep 2008.
- [43] J. Javaloyes, S. Balle, E.A. Avrutin, G. Tandoi, P. Stolarz, M. Sorel, C.N. Ironside, J. Marsh, "Dynamics of semiconductor passively mode-locked lasers: Experiment and theory," In *15th International Conference on Transparent Optical Networks (ICTON)*, Cartagena, June 2013.
- [44] J. J. O'Reilly and P. M. Lane, "Fiber-supported optical generation and delivery of 60 GHz signals," *Electron. Lett.*, vol. 30, no. 16, pp. 1329-1330, 1994.
- [45] P. Shen, N. J. Gomes, P. A. Davies, W. P. Shillue, P. G. Huggard, and B. N. Ellison, "High-purity millimeter-wave photonic local oscillator generation and delivery," in *Proceeding of International Microwave Photonics Topical Meeting*, Sep. 2003, pp.189-192.
- [46] N. Mohamed, S.M. Idrus, A.B. Mohammad, and H. Harun "Millimeter-wave carrier generation system for radio over fiber," In *International Symposium on High Capacity Optical Networks and Enabling Technologies (HONET)*, pp. 111–115, Nov 2008.
- [47] A. J. Cooper, "Fiber/radio for the provision of cordless/mobile telephony services in the access network," *Electron. Lett.*, vol. 26, no. 24, pp. 2054-2056, Nov. 1990.
- [48] G. H. Smith, D. Novak, and C. Lim, "A millimeter-wave full-duplex fiber-radio star-tree architecture incorporating WDM and SCM," *IEEE Photon. Technol. Lett.*, vol. 10, no. 11, pp. 1650-1652, Nov. 1998.

-
- [49] A. Stohr, K. Kitayama, and D. Jager, "Full-duplex fiber-optic RF subcarrier transmission using a dual-function modulator/photodetector," *IEEE Trans. Microw. Theory Techn.*, vol. 47, no. 7, pp. 1338-1341, Jul. 1999.
- [50] A. Stohr, K. Kitayama, and T. Kuri, "Fiber-length extension in an optical 60 GHz transmission system using an EA-modulator with negative chirp," *IEEE Photon. Technol. Lett.*, vol. 11, no. 6, pp. 739-741, Jun. 1999.
- [51] L. Noel, D. Wake, D. G. Moodie, D. D. Marcenac, L. D. westbrook, and D. Nettet, "Novel techniques for high capacity 60 GHz fiber-radio transmission systems," *IEEE Trans. Microw. Theory Techn.*, vol. 45, no. 8, pp. 1416-1423, Aug. 1997.
- [52] T. Kuri, K. Kitayama, A. Stohr, and Y. Ogawa, "Fiber-optic millimeter-wave down-link system using 60 GHz band external modulation," *IEEE J. Lightw. Technol.*, vol. 17, no. 5, pp. 799-806, May 1999.
- [53] J. Ma, C. Yu, Z. Zhou, and J. Yu, "Optical millimeter-wave generation by using external modulator based on optical carrier suppression," *Optics Commun.*, vol. 268, no. 1, pp. 51-57, Dec. 2006.
- [54] Z. Jia, J. Yu, and G. K. Chang, "A full-duplex radio-over-fiber system based on optical carrier suppression and reuse," *IEEE Photon. Technol. Lett.*, vol. 18, no. 16, pp. 1726-1728, Aug. 2006.
- [55] L. Chen, Y. Shao, X. Lei, H. Wen, and S. Wen, "A Novel Radio-over-Fiber System With Wavelength Reuse for Upstream Data Connection," *IEEE Photon. Technol. Lett.*, vol. 19, no. 6, pp. 387-389, Mar. 2007.
- [56] M. Sieben, J. Conradi, D. E. Dodds, "Optical single side band transmission at 10 Gb/s using onle electrical dispersion compensation," *IEEE J. Lightw. Technol.*, vol. 17, no. 10, pp. 1742-1749, Oct. 1999.
- [57] J. Han, B. J. Seo, Y. Han, B. Jalali, and H. Fetterman, "Reduction of fiber chromatic dispersion effects in fiber wireless and photonic time-stretching system using polymer modulators," *IEEE J. Lightw. Technol.*, vol. 21, no. 6, pp. 1504-1509, June 2003.
- [58] J. B. Georges, D. M. Cutrer, M. H. Kiang, and K. Y. Lau, "Multichannel millimeter-wave subcarrier transmission by resonant modulation of monolithic semiconductor lasers," *IEEE Photon. Technol. Lett.*, vol. 7, no. 4, pp. 431-433, Apr. 1995.
- [59] R. W. Ridgway and D. W. Nippa, "Generation and modulation of 94-GHz signal using electroptic modulators," *IEEE Photon. Technol. Lett.*, vol. 20, no. 8, pp. 653-655, Apr. 2008.
- [60] A. Hirata, T. Kosugi, H. Takahashi, R. Yamaguchi, F. Nakajima, T. Furuta, H. Ito, H. Sugahara, Y. Sato, and T. Nagatsuma, "120-GHz-band millimeter wave photonic wireless link for 10-Gb/s data transmission," *IEEE Trans. Microw. Theory Techn.*, vol. 54, no. 5, pp. 1937-1944, May 2006.

Bibliography

- [61] L. Deng, M. Beltran, X. Pang, X. Zhang, V. Arlunno, Y. Zhao, A. Caballero, A. Dogadaev, X. Yu, R. Llorente, D. Liu, and I. T. Monroy, "Fiber wireless transmission of 8.3-Gb/s/ch QPSK-OFDM signals in 75-110-GHz band," *IEEE Photon. Technol. Lett.*, vol. 24, no. 5, pp. 383-385, Mar. 2012.
- [62] S. Preussler, N. Wenzel, A. Zadok, and T. Schneider, "Tunable generation of ultra-narrow linewidth millimeter and THz-waves and their modulations at 40 Gbd," in *International Topical Meeting on Microwave Photonics (MWP)*, Alexandria (USA), Oct. 2013.
- [63] T. Ohno, F. Nakajima, T. Furuta, and H. Ito, "A 240-GHz active mode-locked laser diode for ultra-broadband fiber-radio transmission systems," in *Optical Fiber communication Conference, OFC2005*, Mar. 2005.
- [64] R. Piesiewicz, M. Jacob, M. Koch, J. Schoebel, and T. Kurner, "Performance Analysis of Future Multigigabit Wireless Communication Systems at THz Frequencies With Highly Directive Antennas in Realistic Indoor Environments," *IEEE J. Sel. Topics Quantum Electron.*, vol. 14, no. 2, pp. 421-430, Mar. 2012.
- [65] T. Nagatsuma, H. Ito, and T. Ishibashi, "High-power RF photodiodes and their applications," *Laser and Photonics Review*, vol. 3, no. 1-2, pp. 123-137, Jan. 2009.
- [66] A. Wakatsuki, T. Furuta, Y. Muramoto, T. Yoshimatsua, and H. Ito, "High-power and broadband sub-terahertz wave generation using a J-band photomixer module with rectangular-waveguide output port," in *International Conference on Infrared, Millimeter and Terahertz Waves*, Pasadena (USA), Sep. 2008.
- [67] T. Nagatsuma, H. J. Song, Y. Fujimoto, K. Miyake, A. Hirata, K. Ajito, A. Wakatsuki, T. Furuta, N. Kukutsu, and Y. Kado, "Giga-bit wireless link using 300-400 GHz bands," *Tech. Dig. IEEE International Topical Meeting on Microwave Photonics*, Oct. 2009.
- [68] A. Kanno, T. Kuri, I. Hosako, T. Kawanishi, Y. Yasumura, Y. Yoshida, K. Kitayama, "100-GHz and 300-GHz coherent radio-over-fiber transmission using optical frequency comb source," *Proc. SPIE 8645, Broadband Access Communication Technologies VII*, 864503, Feb. 2013.
- [69] IEEE Std 802.15.3c-2009 (Amendment to IEEE Std 802.15.3-2003), "IEEE Standard for Information Technology — Telecommunications and Information Exchange between Systems — Local and Metropolitan Area Networks — Specific Requirements. Part 15.3: The ultimate purpose of the 60-GHz WPAN systems is to deliver MAC throughput of the order of multi-Gb/s over a reasonable range. To accomplish this, system designers have to increase the transmission range, especially in non-line-of-sight channels. *IEEE Communications Magazine*. July 2011 121 Wireless Medium Access Control (MAC) and Physical Layer (PHY) Specifications for High Rate Wireless Personal Area Networks (WPANs) Amendment 2: Millimeter-Wave-Based Alternative Physical Layer Extension," Oct. 2009, pp. c1-187.

- [70] T. Baykas, C. S. Sum, Z. Lan, J. Wang, M. A. Rahman, H. Harada, S. Kato, "IEEE 802.15. 3c: the first IEEE wireless standard for data rates over 1 Gb/s," *Communications Magazine*, IEEE, vol. 49(7), pp. 114-121, July 2011.
- [71] F. Brendel, J. Poette, B. Cabon, and F. van Dijk, "Low-cost analog fiber optic links for in-house distribution of millimeter-wave signals," *Cambridge/EuMA International Journal of Microwave and Wireless Technology*, vol. 3, pp. 231-236, 2011.
- [72] F. Brendel, J. Yi, J. Poette, B. Cabon, and T. Zwick, "Properties of millimeter-wave signal generation and modulation using mode-locked Q-dash lasers for gigabit RF-over-fiber links," in *7th German Microwave Conference (GeMiC)*, Ilmenau, Germany, PP. 1-4, Mar. 2012.
- [73] F. Brendel, J. Poette, B. Cabon, T. Zwick, F. van Dijk, F. Lelarge, A. Accard, "Chromatic dispersion in 60 GHz radio-over-fiber networks based on mode-locked lasers," *IEEE J. Lightw. Technol.*, vol. 29, no. 24, pp. 3810-3816, Dec. 2011.
- [74] H. Rzaigui, J. Poette, B. Cabon, F. Brendel, and Ramin Khayatzadeh, "Optical Heterodyning for Reduction of Chromatic Dispersion Sensitivity in 60 GHz Mode-Locked Laser Systems," *IEEE J. Lightw. Technol.*, vol. 31, no. 17, pp. 2955-2960, Sep. 2013.
- [75] F. Brendel, T. Zwick, J. Poette, and B. Cabon, "PLL-Stabilized Optical Communications in Millimeter-Wave RoF Systems," *IEEE J. Opt. Commun. Netw.*, vol. 6, no. 1, pp. 45-53, Jan. 2014.

2 Phase Noise Measurement of Unstable Optically Generated Millimeter-Wave signal

2.1 Introduction

Generation of mm-wave carrier signal in mm-wave radio-over-fiber systems relies on optical technique based upon heterodyning of optical modes. In heterodyne detection, two or more optical modes with frequency difference higher than 50 GHz are mixed at a non-linear mixer which is commonly a PD. This non-linear mixing generates mm-wave signals at the output of PD. However, one of the main issues of using this technique is the phase noise or frequency instability of the generated mm-wave signal. One solution in order to reduce phase instability of generated mm-wave signal is to use passively MLL, since all the optical modes are generated inside the same cavity, and so they are phase correlated, the fluctuation of frequency distance between the optical modes reduces [22]. This phase noise reduction is much more in systems based on actively mode locked lasers. Although mode-locking frequencies up to 1 THz have been achieved using MLLs and the phase noise is lower than the techniques based on two free running lasers, still these lasers have their own drawbacks such as frequency drift and phase noise which can impact the performance of the communication system especially for systems based on passively mode locking techniques in which no control outout signal is applied to the laser. Thus, having a good knowledge of the phase noise and frequency drift of PMLLs in RoF systems can help us to select the most proper laser for RoF applications. High phase noise value for a carrier in an RoF system can impact the performance of the system such as: increasing Error Vector Magnitude (EVM), Bit Error Rate (BER) and interferences. Measuring the phase noise of the free running MLLs in frequency domain using spectrum analyzer is not feasible since the frequency drift of generated mm-wave signal is high so that the spectrum analyzer cannot be locked to the carrier frequency. Because of this problem, in this work, we have selected another approach which is based on time domain measurements. In this method and in the first step, we sample the signal in time domain using sampling oscilloscope and in the second step using MATLAB FFT (Fast Fourier Transform), we transform the time domain sampled data to the frequency domain and finally, phase noise measurement at different offset frequencies from the mm-wave carrier is performed using PSD (Power Spectral Density) of the carrier signal. Characterization of PMLL for high speed RoF communications

Chapter 2. Phase Noise Measurement of Unstable Optically Generated Millimeter-Wave signal

is under the scope of this chapter. Developing the MATLAB code for measuring the phase noise in time domain, testing and validation of this method are also other parts presented in this chapter.

2.1.1 What is the phase noise?

Equation 2.1 represents the output signal of an ideal oscillator which generates a pure sine wave.

$$v(t) = A \sin(2\pi f_c t) \quad (2.1)$$

where A and f_c are the amplitude and carrier frequency of the output signal, respectively. As can be seen in 2.1, the amplitude and the frequency of the output signal are constant over time and so the zero crossing time of the output signal in time domain is constant and proportional to period of the signal. The time domain equation for the output signal of a real oscillator is represented as follows:

$$v(t) = A(1 + \epsilon(t)) \sin(2\pi f_c t + \phi(t)) \quad (2.2)$$

Comparing 2.1 and 2.2, one can notice that there are two more terms in 2.2; $\epsilon(t)$ is the amplitude fluctuations and $\phi(t)$ represents the phase fluctuations of the output signal which is known as phase noise. In practice, we always deal with these two unwanted fluctuations.

Because of the time varying phase noise, the frequency of the signal changes with time as well, and so the zero crossing points of the signal also change randomly. This time domain instability is called jitter, and the impact of phase noise in time domain is observed by measuring the jitter. Since the phase noise is a random variable the change in period of the signal is considered as a random variable too.

Noise sources contributing to frequency fluctuations in the practical oscillators can be explained as follow: first, additive noise associated with the oscillator and accessory circuits, such as amplifiers and bias supply, which is merely added to the signal; second, the shot noise in the oscillator that is also related to the amplifier. It requires a current flow in a barrier for example in base emitter junction in a bipolar transistor; third, fluctuations in the resonator frequency [1] and [2]. The main non-linear processes in a classical microwave oscillator occurs in the amplifier. The amplifier brings simultaneously additive and multiplicative noise.

2.1.2 Phase noise spectrum

In frequency domain, output signal of an ideal oscillator would be presented as two Dirac delta functions for positive and negative frequencies at the oscillator carrier frequency, f_c .

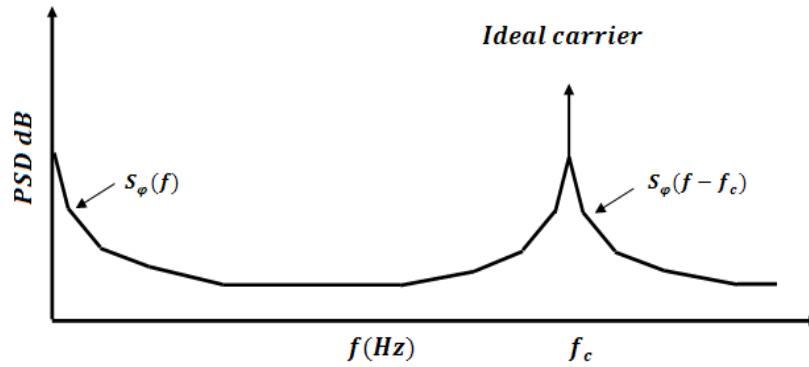


Figure 2.1 – Power spectral density (PSD) of the phase noise at baseband and at carrier frequency f_c .

This shows that all the signal's power is at a single frequency. However, the real oscillators suffer from the phase noise which causes power leakage to the frequencies around the carrier. In order to study the phase noise in frequency domain we rewrite 2.2 as 2.3 by neglecting the amplitude noise as follow:

$$v(t) = A \sin(2\pi f_c t + \phi(t)) = A \left(\sin(2\pi f_c t) \cos(\phi(t)) + \cos(2\pi f_c t) \sin(\phi(t)) \right) \quad (2.3)$$

Assuming that the phase noise is small $|\phi(t)| \ll 1$, one can apply the small angle approximation to 2.3 and obtain 2.5.

$$\sin(\phi(t)) \approx \phi(t) \quad \text{and} \quad \cos(\phi(t)) \approx 1 \quad (2.4)$$

$$v(t) \approx A \left(\sin(2\pi f_c t) + \cos(2\pi f_c t) \phi(t) \right) \quad (2.5)$$

Observing 2.5, one can conclude that the phase noise is modulated by the carrier at frequency of f_c .

The spectral density of a random signal is defined as the Fourier transform of its auto-correlation function. The auto-correlation of the phase is defined as:

$$R_\phi(\tau) = \langle \phi(t) \phi(t + \tau) \rangle \quad (2.6)$$

where $\langle . \rangle$ denotes the mean value over time. Writing R_ϕ as a function of τ alone implies that

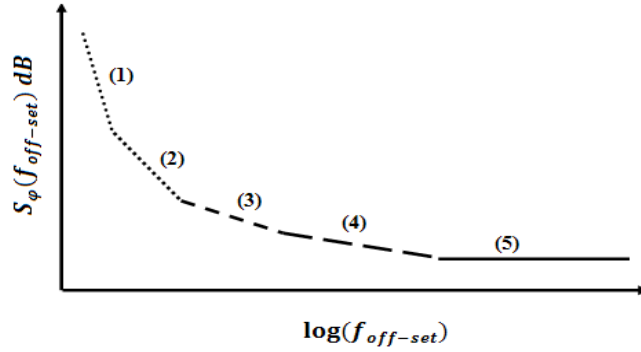


Figure 2.2 – Different sources of the phase noise presented by SSB spectrum of phase fluctuations versus different offset frequencies.

ϕ is wide sense stationary [3]. The spectral density of phase noise can be written as:

$$S_{\phi}(\omega) = \int_{-\infty}^{\infty} R_{\phi}(\tau) \exp(-j\omega\tau) d\tau \quad (2.7)$$

where $\omega = 2\pi f$ is the angular frequency. Using 2.7, one can calculate the spectral density of $\nu(t)$ in 2.5 for positive frequencies as follows:

$$S_{\nu}(\omega) = A^2 \delta(\omega - \omega_c) + A^2 S_{\phi}(\omega - \omega_c) \quad (2.8)$$

Observing 2.8, one can measure the spectral density of phase noise by measuring the spectral density of the oscillator output signal at f_c , as it is shown in Figure 2.1. In this figure, it can be seen that the baseband PSD of phase noise is frequency up-converted to f_c utilizing an ideal carrier which represents $S_{\nu}(\omega)$.

Different sources of the phase noise is modelled in Figure 2.2 [5]. In this figure, a single side band (SSB) phase noise spectral density is illustrated versus offset frequency ($f_{off-set} = f - f_c$) in logarithmic scale. The common sources of phase noise presented in this figure are described as follows [4]:

(1) Random walk frequency modulation (FM) noise: the phase noise PSD follows -40 dB per decade, and it can be observed for the close-in offset frequencies. The noise is generated by the mechanical shock, vibration, or temperature variations that can cause carrier frequency fluctuations.

(2) Flicker (FM) noise: the PSD follows -30 dB per decade. This noise exists in all oscillators and is usually negligible compare to other sources, and it can be observed at close-in offset

frequencies.

(3) White (FM) noise: the spectrum follows -20 dB per decade, and it is the white noise that causes a random frequency modulation. This noise is commonly found in the clocks that use a slave clock locked to another oscillator with high quality factor.

(4) Flicker phase modulation (PM) noise: the spectrum follows -10 dB per decade and is associated with the physics of the resonator and non-oscillatory components. At high offset frequencies, this noise is dominated by white PM noise.

(5) White PM noise: the PSD is flat and it can usually be associated to thermal noise of the resistors, diodes, amplifiers, etc. This noise can be reduced using narrow band filters.

Observing the power spectrum of the phase noise versus offset frequency and comparing with the model presented in Figure 2.2, one can determine different sources of phase noise. On the other hand, by measuring phase noise power spectral density and integrating over desired bandwidth we can determine the mean square value of phase fluctuation (σ^2) [2]:

$$\sigma^2 = \int_{f_1}^{f_2} S_\phi(f) df \quad (2.9)$$

Another advantage of plotting the phase noise spectrum is to find the amount of overlapping of the spectra of two adjacent channels in the communication systems such as GSM (Global System for Mobile Communications). This overlapping is the consequence of using a non-ideal LO at the transceiver and may cause interference among different channels.

2.2 Phase noise measurement methods

There are several well-known phase noise measurement techniques. In this section, some of these techniques are briefly studied and a new digital technique based on frequency demodulation is presented. This method is then used to measure phase noise of mm-wave carriers in an RoF system based on PMLLD.

2.2.1 Direct spectrum technique

Direct spectrum technique is one of the oldest and simplest phase noise measurement techniques. The theory of this technique is studied in previous section where amplitude noise of output signal of oscillator is neglected and phase noise is considered to be small (see 2.8). Using this technique, we often represent the phase noise in terms of SSB spectrum adjacent to the carrier. The representation that is used for this power spectrum is $L_c(f)$, and its unit is $\frac{dB_c}{Hz}$ or dB with respect to the signal power or to the carrier power when total side band power is

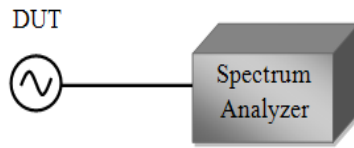


Figure 2.3 – Direct spectrum measurement technique, DUT: Device Under Test.

small. Provided that phase fluctuation mean-squared value is small enough ($\sigma \ll 1$), one can write $L_c(f)$ as: ([8], [9])

$$L_c(f) = \frac{S_\phi(f)}{2} \quad (2.10)$$

As illustrated in Figure 2.3, in this technique, the device under test (DUT) is directly connected to a spectrum analyzer which is tuned to the input signal frequency and directly measuring PSD of signal. Although this technique is very simple, it has many limitations and drawbacks. Some of these drawbacks are listed bellow [6] and [7].

- Significantly limited by the spectrum analyzer's dynamic range since the carrier is not removed from the signal.
- The amplitude noise is not removed from the phase noise measurement results.
- The spectrum analyzer's inherent SSB phase noise at the offset of interest must be lower than the noise of the DUT.
- This technique may not be useful to measure close-in phase noise, since phase noise values are high for these frequencies and small angle approximation may not be applicable.

2.2.2 Phase or frequency detection techniques

In order to separate phase noise from amplitude noise, it is required to use a phase or frequency detector. In this case, the phase noise of a carrier can be demodulated to be measured with a baseband spectrum analyzer to get the spectral density of the phase fluctuation $S_\phi(f)$. These techniques allow us to remove background carrier which effectively can improve dynamic range of measurement system. On the other hand, utilizing phase detectors, we are able to extract the exact value of phase fluctuations, $\phi(t)$, without neglecting impact of amplitude noise.

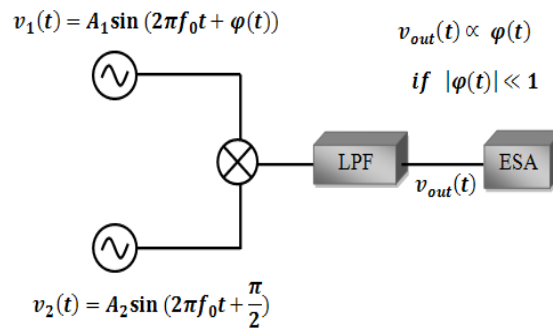


Figure 2.4 – Balanced mixer as a phase detector, LPF: Low Pass Filter, ESA: Electrical Spectrum Analyzer.

2.2.2.1 Phase detector: Balanced mixer

The schematic of this technique is presented in Figure 2.4. The signal from DUT, $v_1(t)$, and the reference signal, $v_2(t)$, are both input to the mixer at same frequency but with 90° phase difference. The high frequency term at the output of mixer is filtered out using a Low Pass Filter (LPF). Thus, the voltage at the output of LPF is proportional to sinus function of phase fluctuations $\varphi(t)$, and so by assuming small angle approximation one can measure the phase noise of DUT directly by measuring the signal at the output of the LPF.

This technique requires a very low phase noise frequency adjustable reference oscillator, and a low noise amplifier (LNA) may be placed after the LPF in order to increase the sensitivity of the system. It is also needed to be sure that the phase quadrature can be maintained without the use of an external PLL or reference.

2.2.2.2 Phase locked loop method

This method is one of the adaptations of phase detector technique, in which a double balanced mixer is used to detect the phase noise. The schematic of this method is illustrated in Figure 2.5, in this method the DUT source is compared to a reference source which is controlled in such a way that follows the DUT frequency drift and maintains the phase quadrature. The high frequency term ($f = 2f_c$) is filtered out using an LPF and the mixer output signal is proportional to the combined phase noise contributions of DUT and reference source. Assuming that the reference source phase noise is negligible compared to DUT, one can conclude that the output signal of the mixer is proportional to phase noise of the DUT. The output signal of the detector is then amplified and analyzed using an electrical spectrum analyzer (ESA).

This phase noise measurement method is capable of tracking frequency drift of DUT, and also is insensitive to amplitude noise. However, using this technique, we need a low phase noise tunable reference source which requires wide tuning range in case of high drifting DUT. It is also needed to mention that, the measurements made inside the PLL bandwidth need to be

Chapter 2. Phase Noise Measurement of Unstable Optically Generated Millimeter-Wave signal

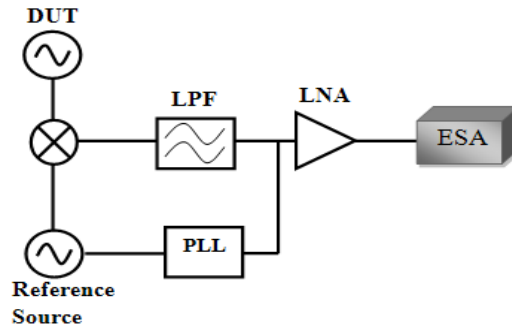


Figure 2.5 – Phase noise measurement using PLL and reference source, PLL: Phase locked loop, LPF: Low Pass Filter, LNA: Low Noise Amplifier, ESA: Electrical Spectrum Analyzer.

corrected which increase the complexity of the phase detector [25].

2.2.2.3 Frequency discriminator method

The frequency discriminator method is proposed in order to remove the need of a second reference source in the phase detector PLL method. This makes the frequency discriminator a suitable method to measure phase noise of high frequency drift sources which are difficult to phase lock.

Figure 2.6 , represents the block diagram of a basic delay line frequency discriminator that converts the frequency fluctuations of DUT into voltage fluctuations. The PSD of this voltage fluctuation is then measured using an ESA. The frequency fluctuation transforms into phase noise in the delay line, and this phase noise is then compared with the signal in the second path using a balanced mixer phase detector. The phase shifter is adjust to put the input signals to the mixer in phase quadrature.

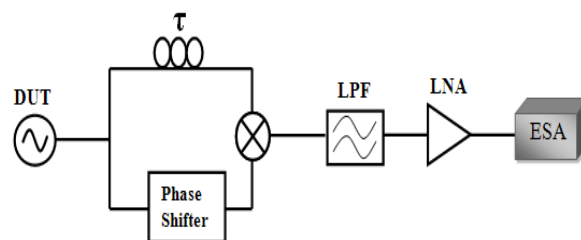


Figure 2.6 – Phase noise measurement using delay line frequency discriminator, LPF: Low Pass Filter, LNA: Low Noise Amplifier, ESA: Electrical Spectrum Analyzer.

In [10], by describing the DUT phase noise as a narrow band frequency modulation (FM)

2.3. Phase noise measurement of optically generated carrier

signal, the output voltage of the LPF is driven as:

$$\Delta v(f_m) = K_\phi 2\pi\tau \Delta f(f_m) \frac{\sin(\pi f_m \tau)}{(\pi f_m \tau)} \quad (2.11)$$

where K_ϕ is the phase detector constant, τ represents the delay provided by the delay line, Δf is the frequency fluctuation of the DUT, and f_m is the offset frequency from the carrier. Observing 2.11, the output voltage fluctuation is proportional to $\sin(x)/x$ which implies that the output response will have peaks and nulls. The nulls occur at offset frequencies equal to $\frac{n}{\tau}$ (n is an integer number), and so the sensitivity of the measurement system is very poor around these offset frequencies. Equation 2.11 also shows that we can increase the sensitivity of the system by increasing the delay time τ . However, this can decrease the offset frequencies at which the nulls occur. The optimum sensitivity and calibration of this system is well studied in [10].

2.2.2.4 Digital phase noise measurement

There are many papers published on digital phase noise measurement techniques. In [12], the authors presented a new approach to measure phase noise using a fast analog-to-digital converter (ADC) to sample RF signal and perform all down-conversion and phase detection using signal processing. In the signal processing part, the Arctangent function is used to extract the phase noise of the DUT, then the detected phase noise from the DUT is subtracted from the phase of a reference oscillator in order to remove the phase noise of instrument's clock. Finally, the spectrum of the measured phase difference is achieved by computing Discrete Fourier Transform (DFT). Using ADC limits the broadband noise floor of PSD by its own white noise. However, there are two main advantages of this technique: Firstly, the phase noise can be measured without using any analog PLL, and secondly, this technique does not require any calibration of phase detector and LNA. For more publications interested readers are referred to [13], [14], and [15]. Digital phase noise measurement is a commercially available technique today (below 1 GHz) for example [26].

Although the theory of phase noise measurement in this technique is relatively simple, practical implementation requires complicated signal processing such as quadrature signal detection and demodulation.

2.3 Phase noise measurement of optically generated carrier

The phase noise measurement methods for optically generated carrier can be the same as those that are used to measure electrically generated carriers phase noise. In this section, we elaborate on problems and issues of phase noise measurement of mm-wave carriers generated in an RoF system based on passively MLLD (PMLLD). The PMLLD used in this

Chapter 2. Phase Noise Measurement of Unstable Optically Generated Millimeter-Wave signal

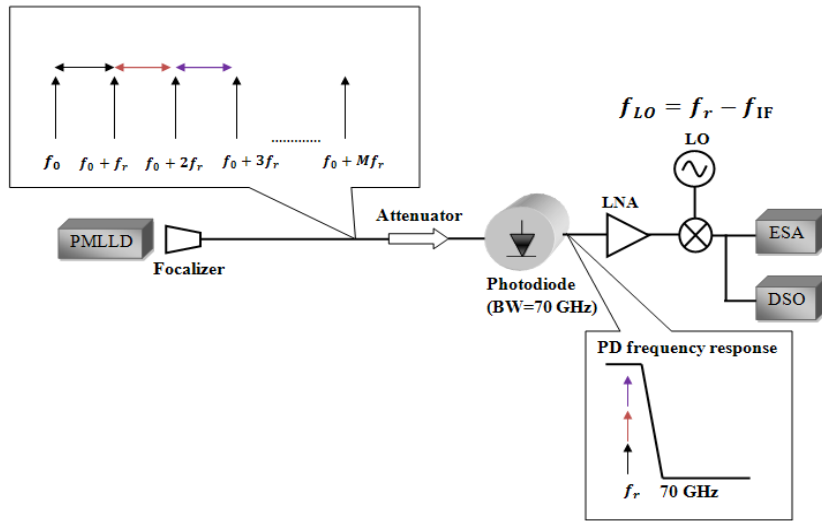


Figure 2.7 – Phase noise measurement setup in RoF system based on PMLLD, LNA: Low Noise Amplifier, LO: Local Oscillator, ESA: Electrical Spectrum Analyzer, DSO: Digital Storage Oscilloscope.

work is a quantum-dash heterostructure grown on S-doped InP wafers [11]. These lasers were manufactured by Alcatel Thales III-V Lab and delivered to IMEP-LAHC lab to be characterized for use in RoF communication systems as part of TelDot ANR project [23].

Figure 2.7 represents phase noise measurement setup in the RoF system based on PMLLD. In order to have maximum optical power into the fiber, a dual lens focalizer is placed after the laser diode, and single mode fiber (SMF) of 70 meter length is used in order to reduce the dispersion effects on RF power at the output of the PD. There are 30 main modes at the output of the laser and the frequency distance between the adjacent modes is fixed and equals laser repetition frequency, $f_r \approx 60 \text{ GHz}$ ¹. Beating among different modes will generate different carrier frequencies at the output of the PD which are equal to the multiples of the laser repetition frequency. However, because of the limited bandwidth of the PD, the frequencies higher than 70 GHz will be filtered out, as illustrated in Figure 2.7. An LNA is used after the PD to increase the level of the mm-wave signal. The mm-wave signal at the output of the LNA is then down-converted to IF using a mixer and an LO in order to be analyzed by signal analyzers. The LO is an Agilent signal generator and the frequency of LO is chosen between 58 GHz to 61 GHz.

In this work, two different approaches are considered to measure the phase noise of IF signal. The first approach is based on using ESA to measure the SSB spectrum of phase noise, and the second approach is based on sampling the IF signal using digital storage oscilloscope (DSO) and signal processing of the samples to extract the phase noise spectrum.

¹The repetition frequency of the laser is adjusted during the fabrication process which is proportional to the length of cavity $\approx 700 \mu\text{m}$.

2.3. Phase noise measurement of optically generated carrier

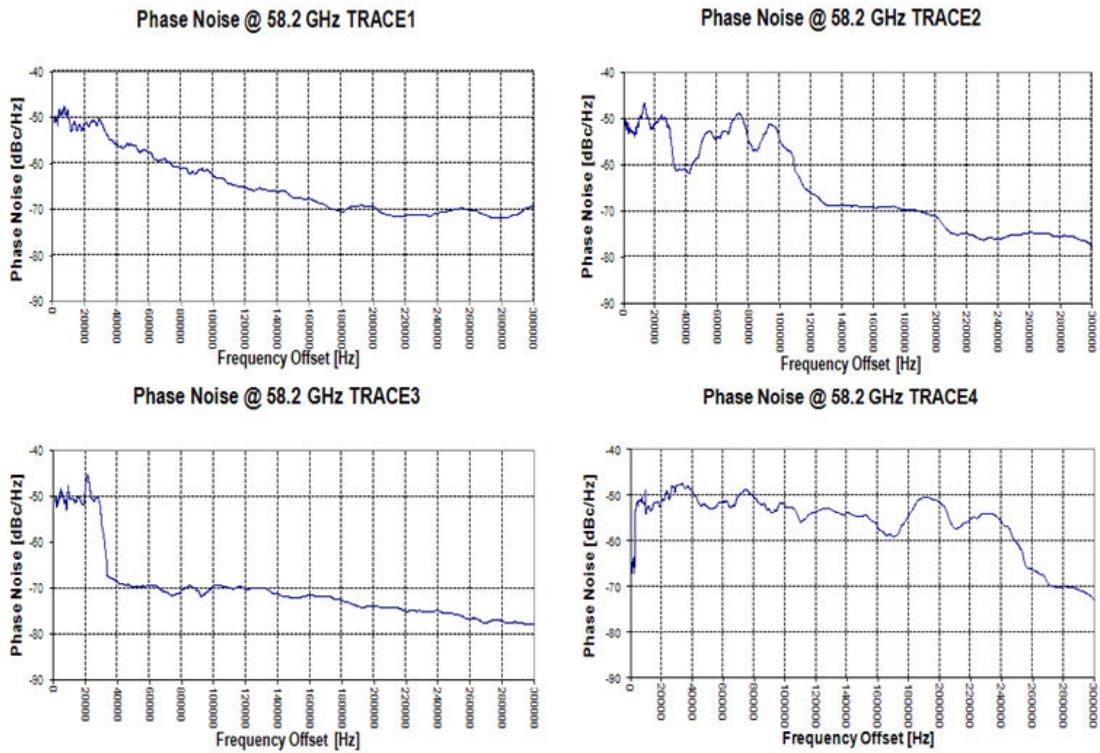


Figure 2.8 – Four phase noise measurement traces for the same laser using direct spectrum analyzer method.

2.3.1 Direct spectrum analyzer method

As illustrated in Figure 2.7, in direct spectrum measurement technique, we measure the SSB spectrum adjacent to the IF carrier, $L_c(f)$, using an ESA (Agilent-40 GHz). The frequency drift of the IF carrier is one of the main issues of using direct spectrum technique to measure optically generated mm-wave phase noise in the RoF system based on PMLLD. The IF carrier frequency drift at the output of the PD is such high that the LO in the ESA cannot track this frequency fluctuations. Therefore, the obtained phase noise spectrum results are not the same for different measurements, especially for the close-in phase noise results.

Figure 2.8 shows four different traces of measured phase noise using direct spectrum analyzer method for the RoF system presented in Figure 2.7. As can be seen in this figure, due to the frequency drift of the IF signal at the output of the mixer measured phase noise spectrum changes over time which indicates that the ESA cannot follow the frequency drift of the IF carrier.

2.3.2 Digital approach

Direct spectrum analyzer technique is the simplest phase noise measurement technique since the intermediate devices such as phase shifter, delay-line, voltage control oscillator (VCO) are

Chapter 2. Phase Noise Measurement of Unstable Optically Generated Millimeter-Wave signal

not needed. On the other hand the spectrum analyzer disability to follow the carrier frequency drift and being locked to IF output signal makes this method unreliable for RoF based on free running optical systems or any other high frequency drift oscillators. The solution that we propose is to replace the spectrum analyzer with a DSO and sample signal in time domain. Using off-line storage and transforming data to the frequency domain by FFT (Fast Fourier Transform) function utilizing desktop computers give us this ability to achieve stable and reliable results. Other advantage of using time sampling to measure the phase noise is that using advanced signal processing methods, we can remove the impact of amplitude noise and extract the exact phase noise value without considering any small angle approximation. The difference between this approach and the digital phase noise technique is that in this technique the signal processing is done off-line using MATLAB which enables us to remove all the digital design difficulties, limitations and costs.

2.3.2.1 Theory of phase noise measurement using time domain sampling

The output pulse train of a PMLLD after converting to electrical signal can be written as:

$$v(t) = \sum_{n=1}^{M-1} A_n \sin(2\pi n f_r t + \phi_n(t)) \quad (2.12)$$

where A_n and f_r are the nominal amplitude and repetition frequency, respectively, and $\phi_n(t)$ represents the phase noise. Here for simplicity, we neglect the amplitude noise and consider the first harmonic, thus we can rewrite 2.12:

$$v(t) = A \sin(2\pi f_r t + \phi(t)) \quad (2.13)$$

A simple approach of measuring the phase noise PSD is based on the assumption that the rms phase deviation is small so that we can apply the small angle approximation to 2.13 as explained in direct detection technique:

$$v(t) \approx A \left(\sin(2\pi f_r t) + \phi(t) \cos(2\pi f_r t) \right) \quad (2.14)$$

Observing 2.14, one can say that phase fluctuation of laser is carried by an ideal carrier with the carrier frequency equals to repetition frequency, so the PSD of down-converted output signal of PD represents the phase fluctuations PSD. An improved technique that we propose here is based on frequency demodulation of PD output signal considering the existence of amplitude noise in order to extract the frequency noise with better accuracy.

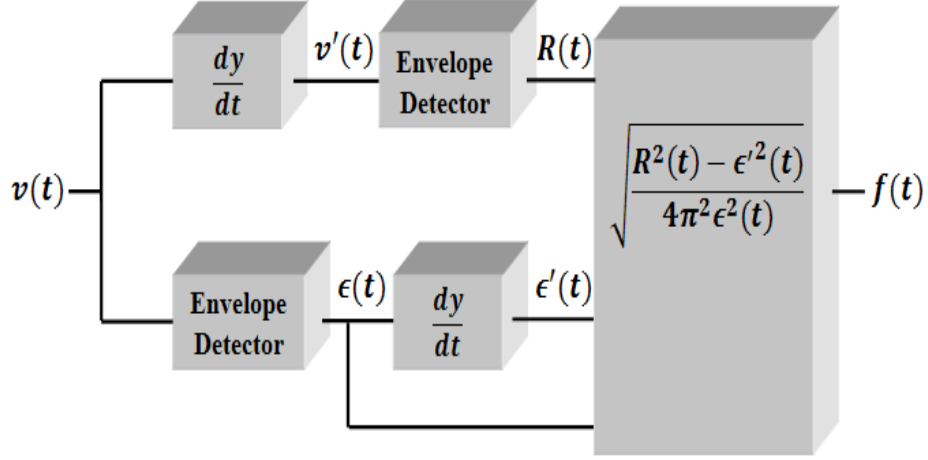


Figure 2.9 – Schematic of signal processing for frequency noise measurement.

Considering the amplitude noise, 2.13 becomes:

$$v(t) = \epsilon(t) \sin\left(2\pi f_r t + \phi(t)\right) \quad (2.15)$$

where $\epsilon(t)$ is the amplitude fluctuation that can be extracted from $v(t)$ using an envelope detector (ED).

By taking derivative of the PD output signal we are able to transform the frequency noise into amplitude fluctuations as following expression:

$$v'(t) = \frac{dv(t)}{dt} = \epsilon(t) \left(2\pi f_r + \frac{d\phi(t)}{dt}\right) \cos\left(2\pi f_r t + \phi(t)\right) + \frac{d\epsilon(t)}{dt} \sin\left(2\pi f_r t + \phi(t)\right) \quad (2.16)$$

For simplicity

$$\epsilon'(t) = \frac{d\epsilon(t)}{dt} \quad (2.17)$$

$$f(t) = f_r + \frac{1}{2\pi} \frac{d\phi(t)}{dt} \quad (2.18)$$

$$y(t) = f(t) - f_r = \frac{1}{2\pi} \frac{d\phi(t)}{dt} \quad (2.19)$$

Chapter 2. Phase Noise Measurement of Unstable Optically Generated Millimeter-Wave signal

The term $f(t)$ represents the instantaneous frequency of output signal of PD and $y(t)$ is the frequency fluctuation, we rewrite 2.16 as:

$$v'(t) = 2\pi\epsilon(t)f(t) \cos\left(2\pi f_r t + \phi(t)\right) + \epsilon'(t) \sin\left(2\pi f_r t + \phi(t)\right) \quad (2.20)$$

Using

$$a \sin(x) + b \cos(x) = R \sin(x + \phi) \quad (2.21)$$

where $R = \sqrt{a^2 + b^2}$, $\sin \phi = \frac{b}{R}$ and $\cos \phi = \frac{a}{R}$, equation 2.20 can be expressed as:

$$v'(t) = R(t) \cos\left(2\pi f_r t + \phi(t) - \Phi(t)\right) \quad (2.22)$$

where

$$R(t) = \sqrt{\epsilon'^2(t) + \left(2\pi\epsilon(t)f(t)\right)^2} \quad (2.23)$$

and

$$\Phi(t) = \tan^{-1}\left(\frac{\epsilon'(t)}{2\pi\epsilon(t)f(t)}\right) \quad (2.24)$$

Observing 2.22, we extract $R(t)$ by using the same ED which is used to extract $\epsilon(t)$ from 2.15. Having $R(t)$, $\epsilon(t)$ and $\epsilon'(t)$ we find the instantaneous frequency which contains the frequency fluctuations.

$$f(t) = \sqrt{\frac{R^2(t) - \epsilon'^2(t)}{4\pi^2\epsilon^2(t)}} \quad (2.25)$$

Finally, having the frequency fluctuations of signal in time domain, we use the FFT to find PSD of frequency fluctuations $S_y(f)$ and phase noise $S_\phi(f)$ [2].

$$S_\phi(f) = \frac{S_y(f)}{f^2} \quad (2.26)$$

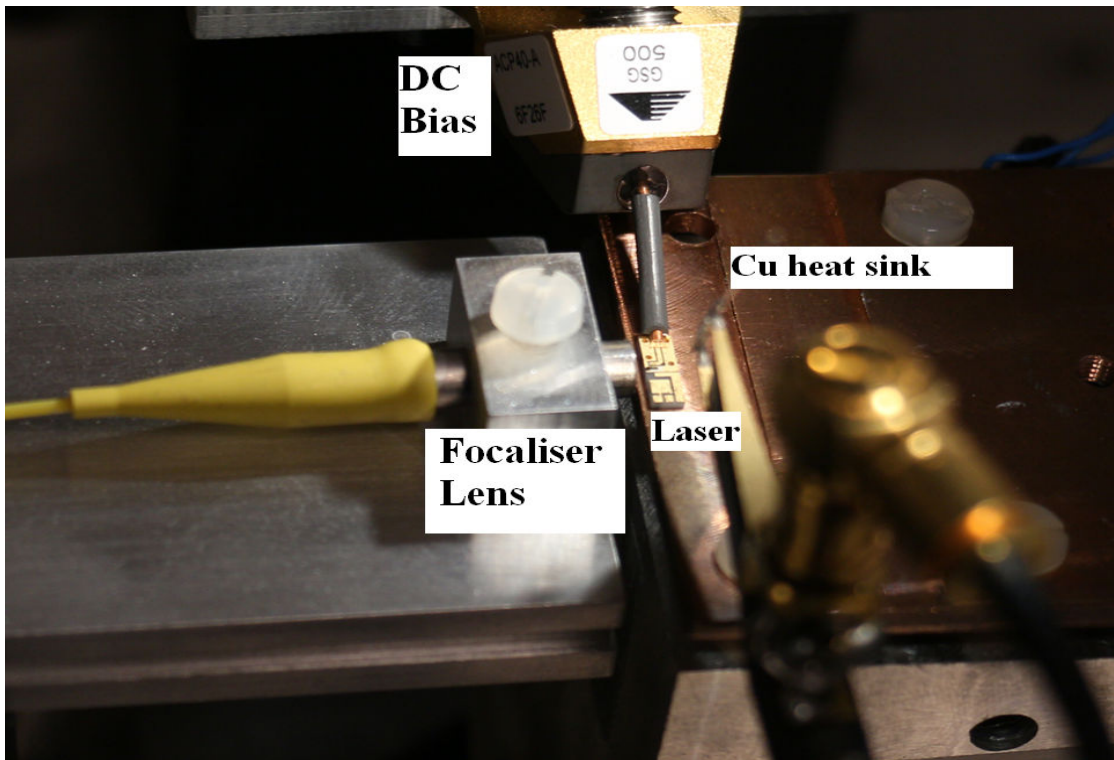


Figure 2.10 – RoF laser (PMLLD) testbench with dual lens focaliser and DC biasing using coplanar prob.

The IF signal after being sampled using DSO, $v(t)$ (see Figure 2.7), is processed using a MATLAB function that is able to extract frequency fluctuation, as illustrated in Figure 2.9. The schematic of signal processing approach used to obtain frequency fluctuation is illustrated in this figure.

2.3.2.2 Measurement results for different PMLLD

Four PMLLD samples have been used for this work which are labelled by the identifiers L24, L34, L611 and L872. The laser test bench is illustrated in Figure 2.10. In this testbench, a focaliser lens is used for coupling between laser and optical fiber. The submount of the laser is placed on a copper heat sink, and the DC bias is established by probing directly onto the coplanar waveguide using a cascade Microtech Infinity Probe. A bias-T is used to supply the DC current and RF signal to the probe.

In order to regulate temperature of the laser a thermo-electric device is placed under the copper heat sink. This thermo-electric device is then connected to a bipolar driver which finds the error amount between the actual temperature and the set point. The actual temperature is measured by a negative-temperature-coefficient (NTC) thermistor. During the experiments, the operating temperature is adjust to 25° Celsius.

Two different signal processing methods are used to obtain the PSD of phase noise: Firstly,

Chapter 2. Phase Noise Measurement of Unstable Optically Generated Millimeter-Wave signal

we use the method based on small angle approximation, $L_c(f)$ in 2.10, and secondly, the PSD obtained using the theory presented in previous section, $S_\phi(f)$ in 2.26. Then, the results from both techniques are compared.

Figure. 2.11 depicts the phase noise measurement results for different laser diodes at their optimal biasing currents (L24 at 200 mA, L34 at 200 mA, L61611 at 200 mA and L872 at 225 mA). These results are obtained assuming small angle approximation for phase fluctuations and neglecting the amplitude noise, $L_c(f)$. The frequency resolution is set to 40 kHz and the noise floor is around $-130 \frac{dB_c}{Hz}$. The results in this figure show that the laser with the identifier L61611 has the highest phase noise comparing to the other lasers. For example at offset frequency of 1 MHz, the phase noise value for L61611 is $-70 \frac{dB_c}{Hz}$, whereas for the lasers L24, L34 and L872, the phase noise values are -84 , -84 and $-88 \frac{dB_c}{Hz}$, respectively.

In previous section 2.1.2, the shape of an oscillator phase noise spectrum is presented in Figure 2.2. Comparing the results in Figure 2.11 and the spectrum shape is presented in Figure 2.2, the effect of white FM noise (-20 dB per decade) can be seen for the offset frequencies of 50 kHz to 100 MHz for the lasers: L24, L34 and L872, whereas for laser L61611 this noise is observable for offset frequencies higher than 1 MHz to 1 GHz and then the measurement reaches the noise floor. The reason that we cannot see the other noise sources effect such as $\frac{1}{f}$ noise is that the linear relationship between $S_\phi(f)$ and $L_c(f)$ only holds for small modulation by phase noise (small angle approximation). On the other hand, the frequency resolution in this figure is not small enough to show the close-in phase noise results. For this reason another measurement is shown in Figure 2.12 with the frequency resolution set to 20 Hz in order to observe the close-in phase noise values. This figure represents the phase noise result for laser L872 and the frequency offset of 20 Hz up to 2 MHz. Observing this figure, we can see that the phase noise results reach a plateau for the offset frequencies close to the carrier ($\approx 50 kHz$) which indicates that phase noise mean square value for these offset frequencies is not small enough to hold the linear relationship between $L_c(f)$ and $S_\phi(f)$. As it is shown in Figure 2.12, the phase noise results are more noisy using smaller frequency resolution (red curve), so in order to reduce the measurement noise we have used the smooth function of MATLAB (black curve). Another drawback of having smaller frequency resolution is the higher noise floor. As it can be seen in Figure 2.11, the noise floor is around $-130 \frac{dB_c}{Hz}$, whereas in Figure 2.12 the noise floor is increased to $-90 \frac{dB_c}{Hz}$. This trade-off between having better frequency resolution, to observe close-in phase noise, and getting reliable result for far from the carrier phase noise is well studied in [16]. To overcome this drawback, a method is developed using which accurate measurement results for both close-in phase noise and far from the carrier phase noise can be assured.

2.3.2.3 Digital technique based on different frequency resolutions

In this technique, we try to use different frequency resolutions in order to observe close-in phase noise and far from the carrier phase noise results in a single figure. To do so, the measurement is done in a series of stages and at each stage a frequency resolution is chosen

2.3. Phase noise measurement of optically generated carrier

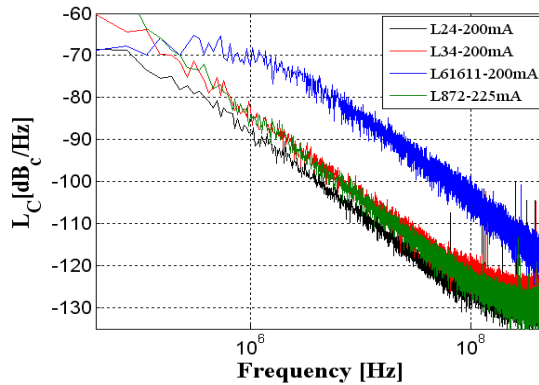


Figure 2.11 – Different laser diodes measured phase noise using small angle approximation method, $L_c(f)$.

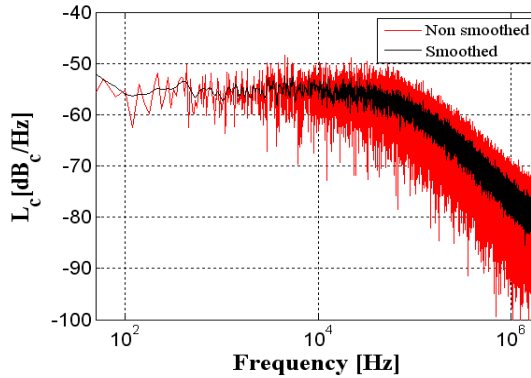


Figure 2.12 – Laser L872 phase noise result with frequency resolution of 20 Hz using small angle approximation method, $L_c(f)$.

which provides for evaluation of a different portion of phase noise PSD. All the different portions are then overlapped in order to present a single figure of the phase noise PSD. In order to change frequency resolution of the phase noise PSD there are two parameters that we can change: (i) sample rate and (ii) obtained record length (number of points obtained by sampling the carrier and used in FFT function). The frequency resolution (FR) relationship with these two parameters is presented in 2.27.

$$FR = \frac{SR}{RL} \quad (2.27)$$

where SR is the sample rate and RL is the record length.

Equation 2.27 shows that by reducing the sampling rate or/and increasing the record length, one can obtain better frequency resolution (lower FR).

Figure 2.13 illustrates the phase noise measurement result using different frequency resolu-

Chapter 2. Phase Noise Measurement of Unstable Optically Generated Millimeter-Wave signal

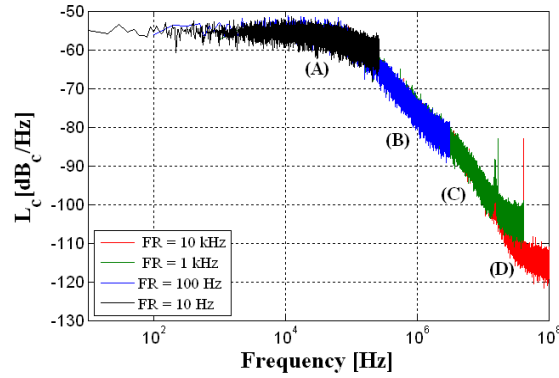


Figure 2.13 – Laser L872 phase noise result with different frequency resolution of (A) 10 Hz, (B) 100 Hz, (C) 1 kHz, (D) 10 kHz.

tions. In this method the resolution frequency has been changed by changing the SR and fixing the memory depth at 100 000 samples. The results for four different resolution frequencies are presented in this figure. Curves (A), (B), (C) and (D) have been achieved for 10 Hz, 100 Hz, 1 kHz and 10 kHz frequency resolution, respectively. The noise floor of the phase noise measurement system depends on the frequency resolution that is achieved using FFT. Lower and lower sample rates assure better and better frequency resolution, but they also cause higher and higher noise floor. We can see the same results in Figure 2.13, the noise floor for the curves (A), (B), (C) and (D) are $-63 \frac{dB_c}{Hz}$, $-85 \frac{dB_c}{Hz}$, $-105 \frac{dB_c}{Hz}$ and $-118 \frac{dB_c}{Hz}$, respectively. Using this technique, we are able to observe the phase noise results from very close to the carrier offset frequencies (1 Hz) to frequencies far from the carrier (100 MHz).

2.3.2.4 Digital technique based on frequency demodulation

In previous section, we have observed that small angle approximation is not applicable for the close-in phase noise values and consequently the $L_c(f)$ cannot be considered as a appropriate method to measure the close-in phase noise, since for the offset frequencies close to the carrier, the phase noise is supposed to be increasing faster with the slope of -30 dB per decade, whereas by estimating $S_\phi(f)$ using $L_c(f)$ the results show a plateau for close-in offset frequencies.

In this section, we use the frequency demodulation method in order to observe the close-in phase noise and the impact of $\frac{1}{f}$ noise on phase noise PSD.

Figure 2.14 represents the results obtained from two different signal processing techniques; the grey curve shows the PSD of phase fluctuations obtained assuming small angle approximation for phase fluctuations, and the black curve is the phase fluctuations PSD using our FM detection method and considering the existence of amplitude fluctuations. As it is shown on this figure, the results are approximately similar for the offset frequencies above 20 kHz and the decreasing rate of phase noise is -20 dB per decade. Below 20 kHz, the grey curve reaches a plateau and for the frequencies closer to 0 Hz the phase noise value remains constant. In

2.3. Phase noise measurement of optically generated carrier

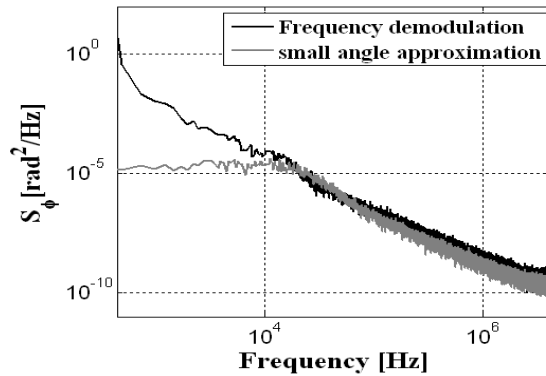


Figure 2.14 – Laser L872 phase noise result using two signal processing techniques, FM detection (black) and small angle approximation (grey).

contrary, the phase fluctuations PSD obtained from our FM detection method (black curve) is increasing for the offset frequencies closer to 0 Hz, which is similar to the model presented by IEEE as recommended frequency stability measure in the Fourier frequency domain [5]. Based on this model, the phase noise increases for the frequencies closer to the carrier, and from a certain frequency close to 0 Hz the $\frac{1}{f}$ noise starts which increases the phase noise fluctuations at these offset frequencies. Therefore, the small angle approximation cannot be reliable for these offset frequencies; in the grey curve, the $\frac{1}{f}$ noise cannot be observed, while the black curve shows $\frac{1}{f}$ noise effect.

2.3.2.5 Accuracy verification

In order to verify the accuracy of the suggested method, we used commercial R&S FSUP signal analyzer to measure phase noise of the same laser. A PLL is located at the end of the communication system presented in Figure 2.7, before the DSO, in order to stabilize the carrier frequency of the output signal of the PD so that phase noise measurement using FSUP analyzer becomes possible. The detailed explanation about the PLL is given in [17].

In Figure 2.15, the black curve represents the results obtained using our time domain sampling method and the blue curve is the measured results obtained by FSUP analyzer. As it is shown in this figure, the two curves are well matched for the offset frequencies higher than 10 kHz, and the difference between the two curves for the frequencies lower than 10 kHz is due to the PLL used in the commercial analyzer which suppresses the phase noise for the frequencies lower than its bandwidth [18]. The overshoot at 90 kHz can be attributed to the loop filter function of the PLL that is used to stabilize frequency of the carrier. The phase noise results in Figure 2.15 are much less than the results in Figure 2.14 because of the PLL used before DSO. Comparison between the two curves presented in this figure shows that our method result perfectly matches the commercial tool result for the frequencies at which the analyzer can work properly. For the offset frequencies where FSUP analyzer results need to be compensated ($f < 10$ kHz), our method gives reliable results.

Chapter 2. Phase Noise Measurement of Unstable Optically Generated Millimeter-Wave signal

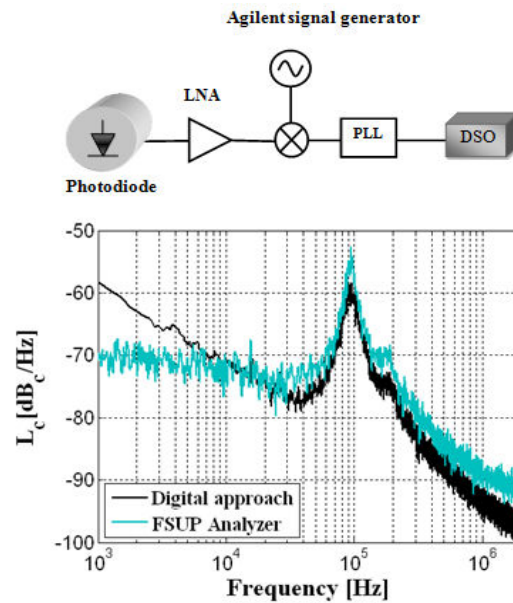


Figure 2.15 – Laser L872 phase noise results using digital technique (Black curve) and FSUP analyzer (Blue curve) [24].

2.3.2.6 Effective elements in phase noise measurement using digital approach

An explanation of critical elements that impact the phase noise measurement is presented in this section.

Frequency resolution

Frequency resolution impacts the measured noise floor as can be seen in Figure 2.13. Lower frequency resolution causes higher noise floor and vice versa, so there is a trade-off between observing close-in phase noise which requires low frequency resolution and measured noise floor. This parameter is well studied in section 2.3.2.3.

Sampling clock phase noise

The sampling process basically is a multiplication of the sampling clock and the analog input signal. This multiplication is in time domain, which is equivalent to convolution in the frequency domain; therefore the spectrum of the sampling clock oscillator is convolved with the input and shows up on the FFT output signal. Thus, close-in phase noise of sampling clock determines the close-in phase noise floor of the digital measurement system and its broadband phase noise impacts over all SNR [19].

2.3. Phase noise measurement of optically generated carrier

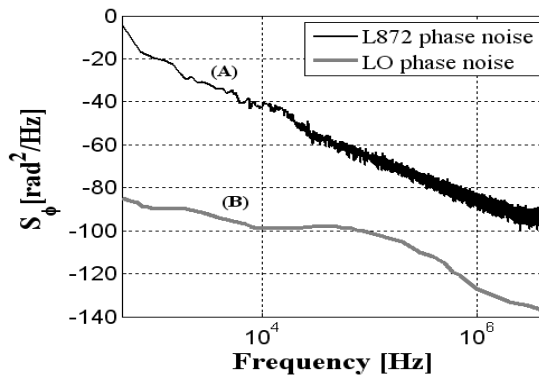


Figure 2.16 – Phase noise comparison between Laser L872 (curve (A)) and the LO (curve (B)).

ADC noise floor

ADC noise impacts the noise floor of the measurement system and its value depends on sampling resolution. ADC with higher sampling resolution causes lower noise floor. The sampling resolution of the DSO used in this work is 8 bits. To calculate the noise floor of an ADC interested readers refer to [20].

LO phase noise

As shown in Figure 2.7, the mm-wave signal is down-converted to IF using a mixer and an LO. And since down-conversion is a multiplication process in time domain, the same explanation as given for sampling clock effect can be true for the LO impact on measured phase noise. Figure 2.16 illustrates a comparison between measured phase noise of laser L872 and the LO. Curve (A) shows the PSD of phase noise of the laser L872 and curve (B) represents the LO phase noise PSD at 67 GHz which is taken from the datasheet of the Agilent PSG (E8257D) [21]. Observing this figure, it can be seen that phase noise of the LO used in our measurement system is way lower than the phase noise of the mm-wave signal and so the impact of LO phase noise on measurement results is negligible.

2.4 Conclusion

In summary, in this chapter we elaborate on phase noise measurement of unstable optically generated mm-wave carrier signal in an RoF system based on PMLLD. We have proposed and experimentally demonstrated an approach to measure the phase noise of optically generated mm-wave carrier based on time sampling of output signal of PD. Using this approach, we have been able to successfully overcome the difficulties of phase noise measurement of mm-wave signal, because of frequency instability, in this RoF system. The proposed method is able to distinguish the amplitude and phase fluctuations so that the impact of amplitude noise on phase noise measured results has been suppressed. Very well matching between the commercial tool and our method results has been observed.

The results have been published in:

Khayatzadeh, R., Rzaigui, H., Poette, J., and Cabon, B. (2013). "Accurate Millimeter-Wave Laser Phase Noise Measurement Technique". *IEEE Photonics Technology Letters*, 25(13), 1218-1221.

Bibliography

- [1] A. Hajimiri, and T. H. Lee, "A General Theory of Phase Noise in Electrical Oscillators," IEEE J. Solid-State Circuits, vol. 33, no. 2, pp. 179-194, Feb. 1998.
- [2] L.S Cutler, and C. L. Searle, "Some Aspects of the Theory and Measurement of Frequency Fluctuations in Frequency Standards," Proc. IEEE, vol. 54, no. 2, pp. 136-154, Feb. 1966.
- [3] J. Rutman, and F. L. Walls, "Characterization of frequency stability in precision frequency sources," Proc. IEEE, vol. 79, no. 6, pp. 952-960, June 1991.
- [4] "Using Clock Jitter Analysis to reduce BER in Serial Data Applications," Application Note, Agilent Technologies, USA, Dec. 2006.
- [5] J. A. Barnes, A. R. Chi, L. S. Cutler, D. J. Healey, D. B. Leeson, T. E. McGunigal, J. A. Mullen, W. L. Smith, R. L. Sydnor, R. Vessot and G. M. R. Winkler, "Characterization of frequency stability," IEEE Trans. Instrum. Meas., vol. IM-20, pp. 105-120, May 1971.
- [6] Agilent Technologies Inc., "Agilent's Phase Noise Measurement Solutions Finding the Best Fit for Your Test Requirements," Selection Guide, USA, July, 2013.
- [7] K. Gheen, "Phase noise measurement methods and techniques," Agilent Technologies, Inc., USA, 2012.
- [8] Hewlett-Packard Co., "HP 3047A/11740A Phase noise Measurement System," Palo Alto, CA, Feb. 1985.
- [9] T. Decker, and B. Temple, "Choosing a phase noise measurement technique," Agilent Technologies Inc., USA, 2000.
- [10] Hewlett-Packard Co., "Phase noise characterization of microwave oscillators: Frequency discriminator method," Product Note: 11729C-2, USA, Sep. 1985.
- [11] F. Lelarge, B. Dagens, J. Renaudier, R. Brenot, A. Accard, F. van Dijk, D. Make, O. Le Gouezigou, J. Provost, F. Poingt, J. Landreau, O. Drisse, E. Derouin, B. Rousseau, F. Pomereau, and G. Duan, "Recent Advances on InAs/InP Quantum Dash Based Semiconductor Lasers and Optical Amplifiers Operating at 1.55 μm ," IEEE J. Sel. Topics Quantum Electron., vol. 13, No. 1, pp. 111-124, Feb. 2007.

Bibliography

- [12] J. Grove, J. Hein, J. Retta, P. Schweiger, W. Solbrig, and S.R. Stein, "Direct-Digital Phase-Noise Measurement," IEEE International Ultrasonics, Ferroelectrics, and Frequency Control Conference, Montreal, Que., Canada, Aug. 2004.
- [13] H. Tsuchida, "Wideband phase-noise measurement of mode-locked laser pulses by a demodulation technique," Optics Lett., vol. 23, No. 4, pp. 286-288, Feb. 1998.
- [14] H. Tsuchida, "Time-interval analysis of laser-pulse-timing fluctuations," Optics Lett., vol. 24, No. 20, pp. 1434-1436, Oct. 1999.
- [15] H. Tsuchida, "Correlation between amplitude and phase noise in a mode-locked Cr:LiSAF laser," Optics Lett., vol. 23, No. 21, pp. 1686-1688, Nov. 1998.
- [16] L. Angrisani, A. Baccigalupi, and M. D'Arco, "Evaluating Phase Noise Power Spectrum with Variable Frequency Resolution," IEEE Trans. Instrum. Meas., vol. 53, No. 3, pp. 685-691, June 2004.
- [17] F. Brendel, T. Zwick, J. Poette, and B. Cabon, "A novel technique for sideband stabilization in the presence of carrier phase noise in RoF systems," in Proc. Eur. Microw. Conf., pp. 550-553, Nov. 2012.
- [18] R. Wanner, Optimum PLL Settings for Phase Noise Measurements With the R&S FSUP Munich, Germany: Rohde & Schwarz, May 2010.
- [19] W. Kester, "Converting oscillator phase noise to time jitter," Analogue Device, Boston, MA, USA, Tech. Rep. MT-008, 2009.
- [20] A. Arrants, B. Brannon and R. Reeder, "Understanding High Speed ADC Testing and Evaluation," Application note, Analogue Devices Inc., USA.
- [21] Agilent E8257D PSG Microwave Analog Signal Generator Datasheet, Agilent Technol., Santa Clara, CA, USA, 2012.
- [22] S. Srinivasan, M. Davenport, M. J. R. Heck, J. Hutchinson, E. Norberg, G. Fish and J. Bowers, "Low phase noise hybrid silicon mode-locked lasers," Front. Optoelectron. vol. 7, no. 3, pp. 265-276, Nov. 2014.
- [23] www.teldot.fr/project.htm
- [24] R. Khayatzadeh, H. Rzaigui, J. Poette, and B. Cabon, "Accurate Millimeter-Wave Laser Phase Noise Measurement Technique". IEEE Photon. Technol. Lett., vol. 25, no. 13, pp. 1218-1221, July 2013.
- [25] Motorola Co., "Phase Noise Measurement Using the Phase Lock Technique," Application Note: AN 1639, USA, 1999.
- [26] <http://www.microsemi.com/products/timing-synchronization-systems/test-measurement/test-sets>

3 Impact of Phase Noise in RoF System Based on PMLLD

3.1 Introduction

In previous chapter the phase noise measurement issues in an RoF system based on optical heterodyning is well studied and a new digital off-line approach is presented in order to ease phase noise measurement of unstable optically generated mm-wave signal. The results in second chapter show that the main weak point of RoF systems where the carrier is generated from optical heterodyning is the frequency instability of the mm-wave signal and so high phase noise value (see Figure 2.16). In this chapter, we study the phase noise impact on RoF system based on PMLLD at 60 GHz and W band RoF based on two free running lasers. We also present the non-coherent frequency down-conversion as a solution for phase noise problem of these systems. The RoF communication systems at 60 GHz and 100 GHz are presented and performances of different electrical down-conversion methods for these communication systems are studied. Impact of PMLLD phase noise on error vector magnitude (EVM) is also observed for different digital modulation schemes and a complete theory and experimental study of using non-coherent frequency down-conversion technique based on envelope detector (ED) is provided. The performance of ED to down-convert the signal with OOK modulation in this communication system is observed using eye diagram and quality factor (Q factor) measurement. In this chapter, it is shown that using an ED at the receiver side, one can overcome the mm-wave frequency fluctuations and so improve the performance of the system.

3.2 Different down-conversion methods

After wireless transmission, the signal at mm-wave frequency needs to be down-converted so that the ADC can sample the received signal and then digitized signal can be processed at mobile station. Hereafter we study two different down-conversion techniques in RoF system based on PMLLD and free running lasers. In the first technique, an ED is used to detect the data from the envelope of the received mm-wave signal. It is shown here that this technique

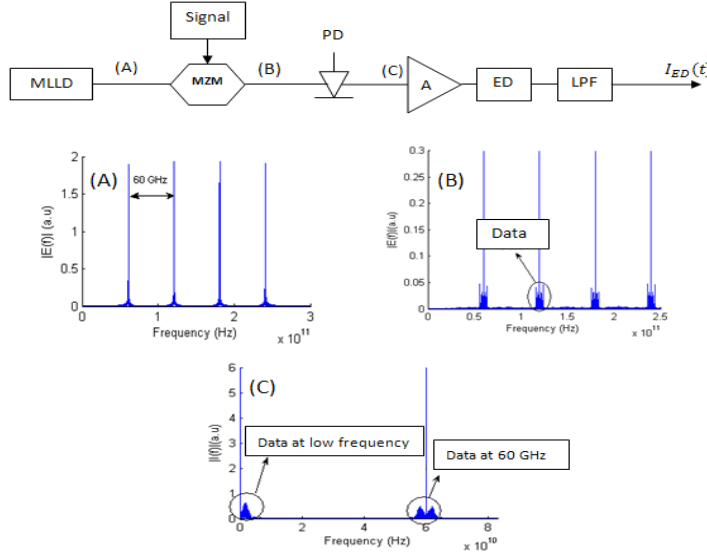


Figure 3.1 – Block diagram of simulated RoF system based on non-coherent receiver, MLLD: mode-locked laser diode, MZM: Mach-Zehnder modulator, PD: photo-diode, A: amplifier, ED: envelope detector, LPF: low pass filter (a) Optical spectrum of signal at output of laser. (b) Optical spectrum of signal at output of modulator. (c) Electrical spectrum of signal at output of PD.

is robust against the phase noise or frequency instability of the received mm-wave signal which is quite high in the systems based on optical heterodyning. In the second technique, the mm-wave signal is down converted to the IF using an LO and a mixer. The frequency of the LO is set to a value close to the repetition frequency of the laser.

3.2.1 Non-Coherent receiver

The block diagram of the suggested RoF system is presented in Figure 3.1. In this figure, the MATLAB simulation result for each block is presented to verify the correctness of the theories and also to make the explanations more clear. As an example, simulation result for optical spectrum composed of four modes is shown in Figure 3.1 (A). The frequency distance between two adjacent modes is set to 60 GHz which is equal to the repetition frequency, $f_r = FSR$ of the cavity, of the PMLLD. The PMLLD produces many optical modes at its output. The optical comb spectrum of a PMLLD consisting of M modes can be described as follows:

$$E(t) = \exp(j(2\pi f_0 t)) \sum_{n=0}^{M-1} E_n \exp\left(j\left(2\pi f_r n t + \phi_n(t)\right)\right) \quad (3.1)$$

where f_0 is the first mode carrier frequency and E_n and ϕ_n are the amplitude and the relative phase fluctuation of the n th optical mode. The intensity of light at the output of laser is externally modulated using an asymmetric Mach-Zehnder modulator (MZM) by digital signals

such as BPSK and QPSK at IF. The electrical field at the output of the MZM can be expressed as:

$$E_{MZM}(t) = \frac{1}{2} \exp(j(2\pi f_0 t + \theta)) \left[1 + \exp(j\Delta\phi(t)) \right] \sum_{n=0}^{M-1} E_n \exp\left(j(2\pi f_r n t + \phi_n(t))\right) \quad (3.2)$$

where θ is the constant phase shift caused by the MZM and

$$\Delta\phi(t) = \frac{\pi}{V_\pi} V(t) \quad (3.3)$$

where $V(t)$ is the applied voltage to the MZM and V_π is the required voltage to tune MZM from minimum to maximum transmission to cause a phase shift of 180° . Optical spectrum of modulated signal at the output of MZM is shown in Figure 3.1 (B). Observing this figure, we can see that the data appears as two side bands around each mode. At the base station, beating between the modes is done utilizing a PD. Output current of the PD, with responsivity of R , can be found as following:

$$\begin{aligned} I_{PD}(t) &= RP_{opt} = \frac{R}{4} \left(2 + \exp(j\Delta\phi(t)) + \exp(-j\Delta\phi(t)) \right) \\ &\times \left(\sum_{m=0}^{M-1} \sum_{n=0}^{M-1} E_m E_n \exp\left(j(m-n)2\pi f_r t + \phi_m(t) - \phi_n(t)\right) \right) \\ &= \frac{R}{2} (1 + \cos\Delta\phi) \times \left(\sum_{m=0}^{M-1} \sum_{n=0}^{M-1} E_m E_n \cos\left((m-n)2\pi f_r t + \phi_m(t) - \phi_n(t)\right) \right) \end{aligned} \quad (3.4)$$

Assuming the PD bandwidth is limited to less than $2f_r$, 100 GHz in practical, only the terms with condition $|i - j| = 1$ can pass through the PD, so we can rewrite 3.4 as:

$$I_{PD}(t) = \frac{R}{2} (1 + \cos\Delta\phi(t)) \left[\sum_{i=0}^{M-2} 2E_i E_{i+1} \cos\left(2\pi f_r t + \phi_{i+1}(t) - \phi_i(t)\right) + \sum_{i=0}^{M-1} E_i^2 \right] \quad (3.5)$$

The electrical spectrum of the detected signal at the output of the PD is illustrated in Figure 3.1 (C). The data at 60 GHz corresponds to the first sum in 3.5 and the data at IF frequency corresponds to the second sum. Signal at IF frequency (some GHz) will be experimentally filtered out after passing through low noise amplifier whose center frequency is 60 GHz and its bandwidth is limited to some GHz.

Assuming an ideal square-law ED and considering that the DC term in 3.5 is filtered out by the amplifier, the terms containing the DC can be neglected and so, the intensity at the output of the detector, $I_{out}(t)$, can be written as:

$$I_{out}(t) = |I_{PD}(t)|^2 = \frac{R^2}{2} \left(1 + \cos \Delta\phi(t) \right)^2 \times \left[\sum_{i=0}^{M-2} \sum_{j=0}^{M-2} E_{i+1} E_i E_{j+1} E_j \cos \left(4\pi f_r t + (\phi_{i+1} - \phi_i) + (\phi_{j+1} - \phi_j) \right) + \sum_{i=0}^{M-2} \sum_{j=0}^{M-2} E_{i+1} E_i E_{j+1} E_j \cos \left((\phi_{i+1} - \phi_i) - (\phi_{j+1} - \phi_j) \right) \right] \quad (3.6)$$

The first sum in 3.6 is the high frequency term that will be filtered out by the low pass filter (LPF) of the ED. So the down-converted signal after LPF can be written as

$$I_{ED}(t) = \frac{R^2}{2} \left(1 + \cos \Delta\phi(t) \right)^2 \left[\sum_{i=0}^{M-2} \sum_{j=0}^{M-2} E_{i+1} E_i E_{j+1} E_j \cos \left(\Delta\phi_{non-coherent} \right) \right] \quad (3.7)$$

where

$$\Delta\phi_{non-coherent} = (\phi_{i+1} - \phi_i) - (\phi_{j+1} - \phi_j) \quad (3.8)$$

Theory in 3.7 shows that phase and amplitude modulation of the modulating signal at IF can be recovered, as they are both modulating the amplitude of the optical modes. It can be also seen that the output signal of the ED, I_{ED} , contains the phase fluctuation, $\Delta\phi_{non-coherent}$, which depends on the subtraction of the phase difference between adjacent modes.

We need to mention that the $\Delta\phi(t)$ contains the data signal, this can be shown by setting the applied signal to the MZM and biasing the modulator in the middle of transmission, $V_{DC} = \frac{V_\pi}{2}$

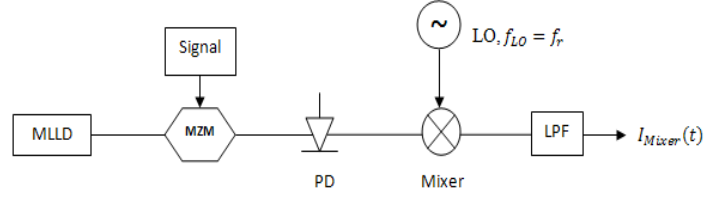


Figure 3.2 – Block diagram of RoF system based on MLLD and coherent receiver, LO: local oscillator.

as:

$$V(t) = \frac{V_{\pi}}{2} + D(t) \quad (3.9)$$

where $D(t)$ is the data signal and so

$$\Delta\phi(t) = \frac{\pi}{V_{\pi}} \left(\frac{V_{\pi}}{2} + D(t) \right) \quad (3.10)$$

and then assuming small angle approximation we will have the data signal at the output of the cosine function

$$\cos(\Delta\phi(t)) = \cos\left(\frac{\pi}{2} + \frac{\pi}{V_{\pi}} D(t)\right) = -\sin\left(\frac{\pi}{V_{\pi}} D(t)\right) \approx -\frac{\pi}{V_{\pi}} D(t) \quad (3.11)$$

3.2.2 Coherent receiver

The block diagram of the RoF system based on coherent receiver is presented in Figure 3.2. As can be seen in this figure the electrical signal after PD is down-converted to IF using a mixer and an LO. The frequency of the LO is close to the repetition frequency of the laser. The down-converted signal can be easily be found assuming output signal of the LO as follows

$$I_{LO}(t) = I_{LO} \cos\left(2\pi f_{LO}t + \phi_{LO}(t)\right) \quad (3.12)$$

where I_{LO} , f_{LO} and $\phi_{LO}(t)$ are the amplitude, carrier frequency and phase fluctuation of the LO, respectively. And the output signal of the mixer can be expressed as

$$I_{Mixer}(t) = \frac{R}{2} I_{LO} \left(1 + \cos \Delta\phi(t)\right) \left(\sum_{i=0}^{M-1} E_i E_{i+1} \left[\cos\left(2\pi(f_r + f_{LO})t + \phi_{i+1}(t) - \phi_i(t) + \phi_{LO}(t)\right) + \cos\left(2\pi(f_r - f_{LO})t + \phi_{i+1}(t) - \phi_i(t) - \phi_{LO}(t)\right) \right] \right) \quad (3.13)$$

Assuming that $f_{LO} = f_r$ and removing the high frequency term, we can rewrite 3.13 as follows using 3.11,

$$I_{Mixer}(t) = \frac{R}{2} I_{LO} \left(1 - \frac{\pi}{V_\pi} D(t)\right) \sum_{i=0}^{M-1} E_i E_{i+1} \cos\left(\Delta\phi_{coherent}\right) \quad (3.14)$$

where

$$\Delta\phi_{coherent} = \phi_{i+1} - \phi_i - \phi_{LO} \quad (3.15)$$

Comparing 3.7 and 3.14, if one assumes that the modes of the MLLD are perfectly locked within the full spectrum, then this implies that the receiver based on non-coherent detector is completely robust against the laser phase noise effects ($\Delta\phi_{non-coherent} = 0$), however this assumption may not be correct within the full spectrum of the MLLD. But the assumption that this fluctuation is much smaller than the phase difference between the adjacent modes is feasible, $\Delta\phi_{non-coherent} \ll \Delta\phi_{coherent}$, which can show that down-conversion using ED is much more robust against the laser phase noise effects, consequently, impact of the LO phase noise does not exist for this receiver. Furthermore non-coherent receiver benefits of more simplicity when compared to coherent receiver by removing a mixing stage and an LO. The

3.3. RoF based on PMLLD using coherent and non-coherent receivers at 60 GHz

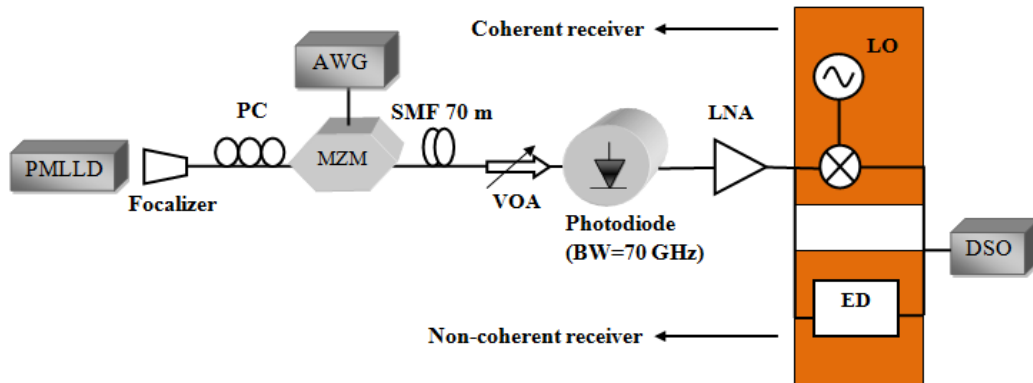


Figure 3.3 – Experimental set-up of RoF communication system based on non-coherent receiver and coherent receiver - PMLLD: passively mode-locked laser diode, PC: polarization controller, MZM: Mach-Zehnder Modulator, AWG: arbitrary waveform generator, SMF: single mode fiber, VOA: variable optical attenuator LO: local oscillator, DSO: digital storage oscilloscope.

coherent detection is still the only way to measure the phase noise of the beat-note and also the only way to perform full phase recovery in complex systems, in contrary with the envelope detection.

3.3 RoF based on PMLLD using coherent and non-coherent receivers at 60 GHz

3.3.1 Non-coherent receiver

The experimental set-up of RoF communication system based on PMLLD and an electrical non-coherent down-conversion stage using an ED is presented in Figure 3.3. The repetition frequency of PMLLD is 60.9 GHz and the output optical power is 9 dBm. The external modulation is done using an MZM, the data at IF is applied to the MZM using an Arbitrary Waveform Generator (AWG) that generates QPSK signals at different data rates. A 70 meter single mode optical fiber is used in order to achieve maximum RF power at the output of the PD. The received optical power of the PD and consequently the electrical power at the input of the ED can be controlled using variable optical attenuator (VOA) before the PD. A PIN PD of 70 GHz bandwidth is used to realize the beating of optical modes, and also acts as a filter for higher order mode beatings. At the receiver, a zero bias power detector, Schottky barrier beam lead diode, acts as ED and is used to extract the data from envelope of received signal. Before the ED an amplifier of 30 dB gain with 10 GHz bandwidth is used to increase the power level. EVM values are measured using Vector Signal Analyzer (VSA) after being sampled by digital storage oscilloscope (DSO).

3.3.1.1 EVM measurement

The error vector magnitude (EVM) is a measure used to quantify the performance of a digital radio transmitter or receiver. A signal sent by an ideal transmitter or received by a receiver would have all constellation points precisely at the ideal locations, however various imperfections in the implementation such as carrier leakage, amplitude, phase noise etc. cause the actual constellation points to deviate from the ideal locations. Informally, EVM is a measure of how far the points are from the ideal locations [2]. EVM measurements can provide a great deal of insight into the performance of digitally modulated signals. With proper use, EVM and related measurements can pinpoint exactly the type of degradations present in a signal and can even help identify their sources. In order to measure EVM value, the average power of the error vector is divided to the power of the reference signal. In this case, the EVM is measured in dB as in 3.16:

$$EVM(dB) = 10 \log \left(\frac{P_{error}}{P_{signal}} \right) \quad (3.16)$$

EVM can also be expressed as [3]:

$$EVM(\%) = \frac{\sqrt{\frac{1}{N} \sum_{n=1}^N |S_r(n) - S_t(n)|^2}}{R_{max}} \times 100 \quad (3.17)$$

where N is the number of transmitted symbols, S_r is normalised received symbol, S_t is the ideal transmitted symbol, and R_{max} is maximum magnitude of the ideal transmitted symbol for the chosen modulation. However, in order to better see the impact of phase and amplitude noise on EVM, it can be further expressed as [4]:

$$EVM = \sqrt{\frac{1}{SNR} + 2 - 2 \exp\left(\frac{-\sigma^2}{2}\right)} \sqrt{\frac{1}{PAPR}} \quad (3.18)$$

where SNR is signal to noise ratio, σ is rms value of phase noise and PAPR is the peak to average power ratio for the considered modulation scheme.

3.3. RoF based on PMLLD using coherent and non-coherent receivers at 60 GHz

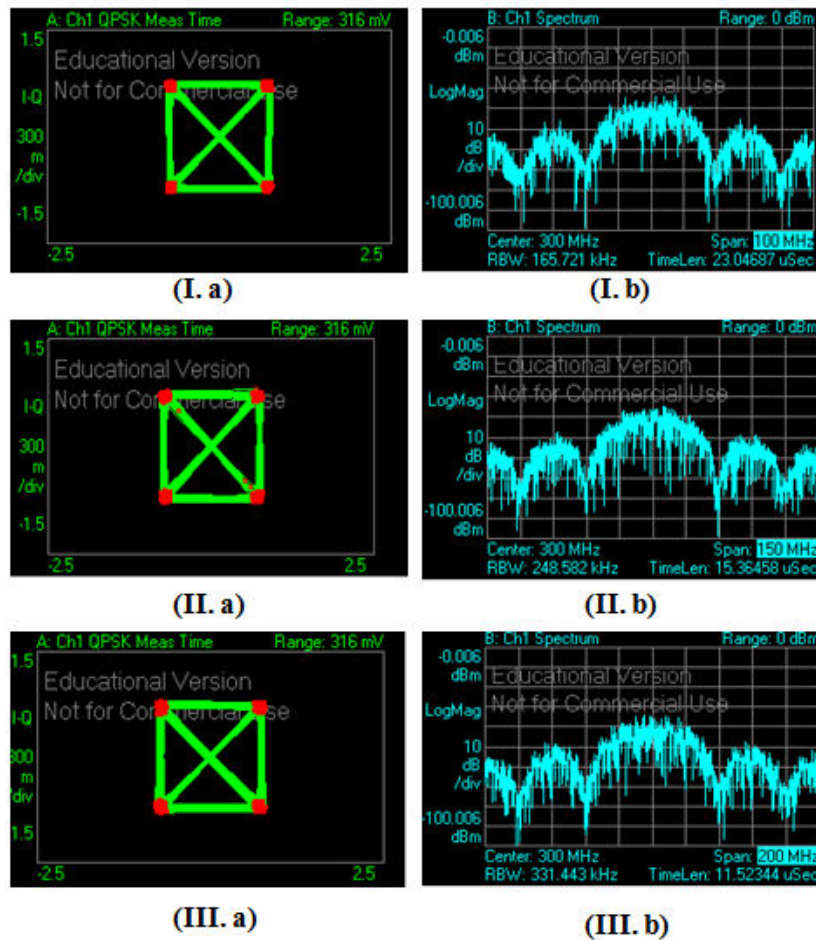


Figure 3.4 – Constellation diagram and power spectrum of the detected signal for RoF system based on PMLLD (L872) and non-coherent receiver (ED) at 60 GHz and intermediate frequency of 300 MHz. (I.a) QPSK data rate of 40 Mbps, EVM=5.4 %. (I.b) PSD, QPSK data rate of 40 Mbps. (II.a) QPSK data rate of 60 Mbps, EVM=5.5 %. (II.b) PSD, QPSK data rate of 60 Mbps. (III.a) QPSK data rate of 80 Mbps, EVM=5.6 %. (III.b) PSD, QPSK data rate of 80 Mbps.

The system performance is verified for different data rates and received optical power values as shown in Figure 3.4. The optical fiber length is fixed to 70 m while the received optical power is varied by changing the attenuation value of the VOA. The electrical loss imposed by RF down-conversion stage (in this section ED) is 27 dB. A constellation diagram is a representation of a signal modulated by a digital modulation scheme. It displays the signal as a two dimensional scatter diagram in the complex plane at symbol sampling instants. This diagram represents the possible symbols that may be selected by a given modulation scheme as points in the complex plane.

Measured constellation diagrams can be used to recognize the type of noise and distortion in a signal [5]. The constellation diagram and the power spectrum of the detected signal for QPSK modulation at different data rates is presented in Figure 3.4. The intermediate frequency

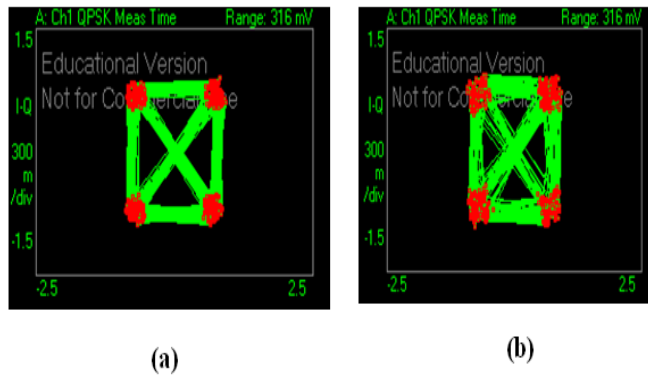


Figure 3.5 – Constellation diagram of the detected signal for RoF system based on PMLLD (L872) and non-coherent receiver at 60 GHz and intermediate frequency of 500 MHz. (a) QPSK data rate of 300 Mbps, EVM=12 %. (b) QPSK data rate of 400 Mbps, EVM=16 %.

is set at 300 MHz and the data rate varies from 40 Mbps to 80 Mbps for figures I, II and III, respectively.

The measured EVM values for 40 Mbps, 60 Mbps and 80 Mbps are 5.4 %, 5.5 % and 5.6 %, respectively. In order to increase the data rate to higher values, the intermediate frequency is set to 500 MHz and then the data rate is increased to 300 Mbps and 400 Mbps for QPSK modulation scheme. The constellation diagram for 300 Mbps and 400 Mbps are shown in Figure 3.5 (a) and (b). The EVM results for the same received optical power and for 300 Mbps and 400 Mbps are 12 % and 16 %, respectively. Comparing the results in Figure 3.4 and 3.5, one can conclude that increasing the data rate increases the EVM of the system. This degradation in performance of the system is due to: firstly, the bandwidth limitation of the ED and secondly, for the same received optical power by increasing the data rate the bandwidth of the limiting filter at the receiver side needs to be increased so the noise power will increase which reduces the SNR value and consecutively increases the EVM of the system. The bandwidth limitation of ED is that of an internal electrostatic discharge (ESD) protection circuit that protects detector from possible damages. Nevertheless, this limitation can be removed by replacing the ESD protection with an LNA with large bandwidth which can protect the detector against ESD and also increase the bandwidth of the signal at the output of the detector. Figure 3.6, represents the transfer function of the ED used in our receiver (Millitech DET-15) when terminated to a 50 Ω load. As can be seen in this figure, the RF power at the output of the detector for IF at 500 MHz is 10 dB less compare to the peak value at IF of 50 MHz.

Observing the constellation diagrams, one can conclude that the impact of phase noise on received symbols is removed and the only noise impact is the amplitude noise which includes intensity noise of the laser, shot noise and the thermal noise at the receiver. More details on amplitude noise impact on EVM in RoF system are given in the next chapter.

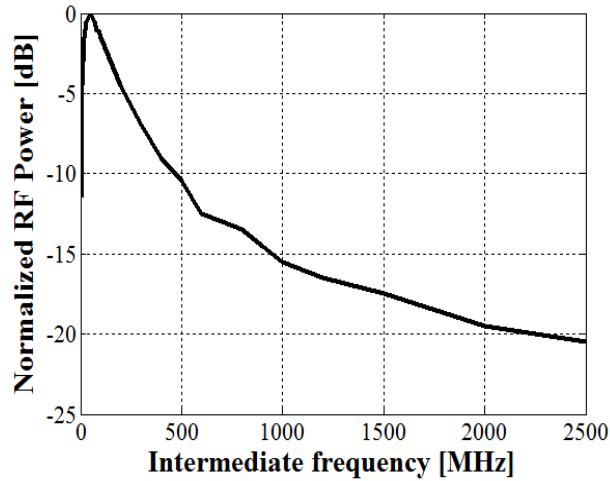


Figure 3.6 – Normalized output power of detector (DET-15) versus intermediate frequency

3.3.1.2 Q factor measurement

The Q factor represents the concept of SNR in a digital signal and is defined as:

$$Q = \frac{I_1 - I_2}{\sigma_1 + \sigma_0} \quad (3.19)$$

where I_1 and I_2 correspond to the levels of the data '1's and '0's and σ_1 and σ_0 correspond to the standard deviation of the noise on '1's and '0's, respectively. Q factor measurement is done using DSO. The OOK signals with different bit rates are applied to the MZM using AWG. The Q factor measurement is done for non-coherent receiver using the same experimental set-up as presented in Figure 3.3.

The eye diagrams for different data rates of 100, 300, 500 Mbps and 2.5 Gbps for OOK modulation are presented in Figure 3.7(a)–(d), respectively. It can be seen that the eye opening is diminishing while the data rate increases which is due to the limited bandwidth of the detector also resulting in inter symbol interference. As can be seen in this figure, the phase noise or jitter is removed but the impact of amplitude noise on eye opening can be observed. Q factor is then measured using 3.19.

The measured Q factor for bit rates of 100, 300 and 500 Mbps for non-coherent receiver are presented in Figure 3.8. For received optical power less than -1.7 dBm, increasing received power increases the Q factor. A Q factor of more than 6 for received optical power of -3.7 dBm and data rate of 500 Mbps is achieved, which corresponds to a bit error rate (BER) less than 10^{-9} [6]. By increasing the data rate to 500 Mbps, it can be seen that the Q factor decreases,

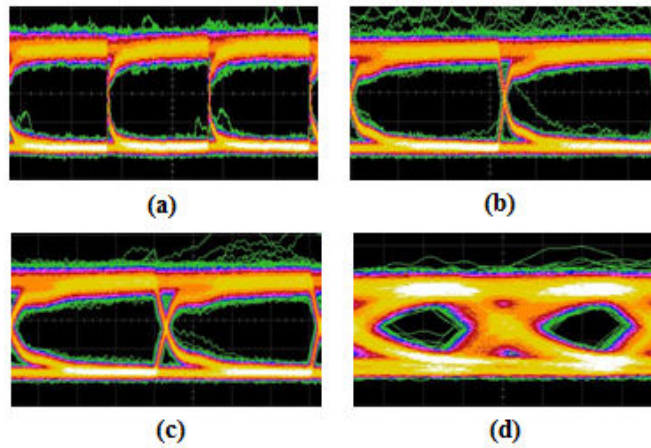


Figure 3.7 – Measured eye diagram for OOK signal at (a) 100 Mbps (b) 300 Mbps (c) 500 Mbps and (d) 2.5 Gbps for the received optical power of -0.25 dBm.

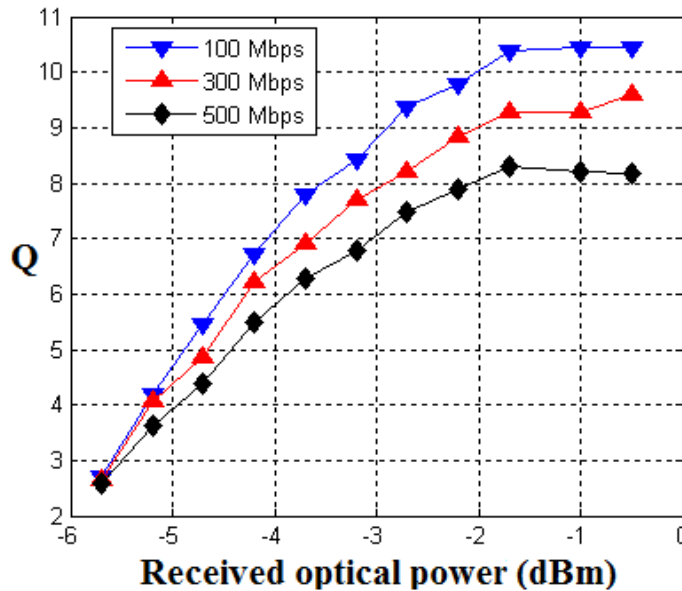


Figure 3.8 – Q factor versus received optical power for different bit rates using non-coherent receiver.

which is attributed mainly to the bandwidth limitation imposed by the detector.

3.3.2 Coherent receiver

As it is shown in Figure 3.3, in the coherent receiver, a mixer and an LO is used in order to down-convert the mm-wave signal to IF. The mixer used in this set-up is a V band mixer (M60-5 Spacek Labs 55-65 GHz) with IF bandwidth of 10 GHz and conversion loss of 5 dB at 60 GHz. Before the mixer, an amplifier of 30 dB gain is used to increase the power level. The

3.3. RoF based on PMLLD using coherent and non-coherent receivers at 60 GHz

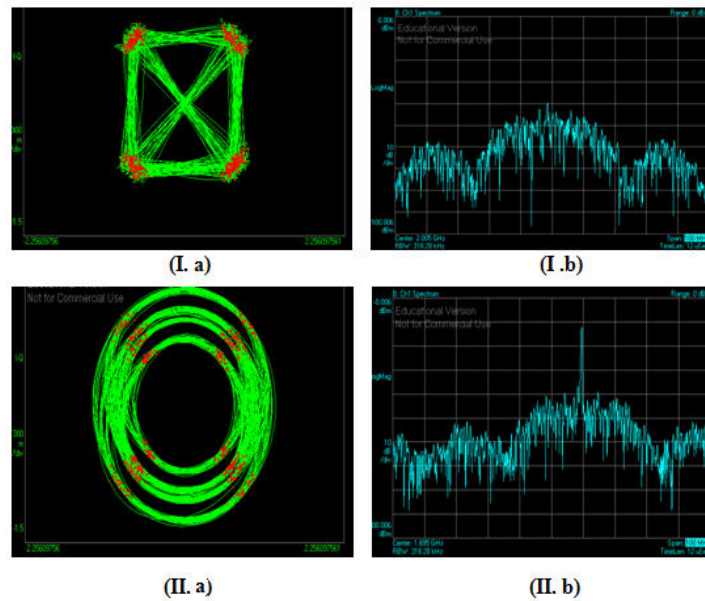


Figure 3.9 – Constellation diagram and power spectrum of the detected signal for RoF system based on PMLLD (L872) and coherent receiver at 60 GHz and intermediate frequency of 1 GHz. (I.a) constellation diagram of signal without harmonics, QPSK data rate of 100 Mbps, EVM=11 %. (I.b) PSD, QPSK data rate of 100 Mbps. (II.a) constellation diagram of signal with harmonic at 2 GHz, QPSK data rate of 100 Mbps, EVM=20 %. (II.b) PSD with harmonic at 2 GHz, QPSK data rate of 100 Mbps.

LO is a frequency tunable Agilent signal generator.

The constellation diagram for QPSK modulation at 1 GHz IF and data rate of 100 Mbps is presented in Figure 3.9. In this figure, constellation diagram and PSD for two different scenarios are presented. In Figure 3.9 (I. a), the results show the constellation diagram of the scenario in which there is no harmonics in the received frequency band, as it can be seen in the PSD of the signal in Figure 3.9 (I. b). Still the impact of phase noise on the detected symbols can be observed which shows that coherent receiver is sensitive to phase or frequency instability. The measured EVM in this scenario is 11 %. The constellation diagram and PSD of the detected signal in presence of a harmonic at 2 GHz is presented in Figure 9 (II. a) and (II. b), respectively. The measured EVM in this scenario is increased to 20 %.

3.3.3 Coherent and non coherent receiver, a comparison

Table 3.1 represents EVM values measured for back to back (BTB) configuration, coherent and non-coherent receivers. As it is expected, the EVM values for RoF based on non-coherent receiver are lower than the values for coherent receiver, for approximately the same received optical power, despite the loss imposed by the non-coherent receiver which is much more than the coherent receiver loss, it is seen that the EVM results of the coherent detector are

Chapter 3. Impact of Phase Noise in RoF System Based on PMLLD

much higher than the the EVM values of non-coherent receiver, which implies that the phase noise impact on down-converted data using coherent receiver is degrading the performance of RoF system.

Table 3.1 – EVM results versus Bit Rate for different scenarios

Bit Rate(Mbps)	EVM (%)	EVM (%)	EVM (%)
-	BTB	Coherent	Non-coherent
100	2.8	11.0	4.8
200	2.9	11.3	6.7
300	3.8	11.5	9.6
400	4.0	11.8	9.8

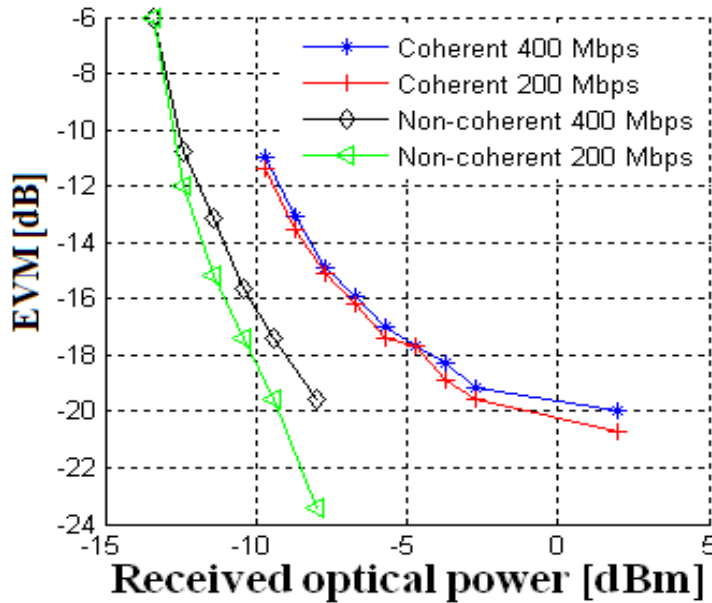


Figure 3.10 – EVM versus received optical power for both coherent and non-coherent receivers at 400 and 200 Mbps with QPSK modulation.

In Figure 3.10, measured EVM values versus received optical power for both coherent and non-coherent receivers and data rates of 400 and 200 Mbps are illustrated and compared. The results show that EVM values for non-coherent receiver are lower than values for coherent receiver, for the same received optical power, despite the loss imposed by power detector. As can be seen in this figure, the EVM results for coherent receiver reach a floor for optical power more than -4 dBm due to the phase noise. Observing this floor, one can conclude that increasing received optical power in order to improve SNR without reducing phase noise will not improve the performance of communication system based on coherent receiver, while it improves SNR and EVM for the receiver based on non-coherent receiver.

We can use 3.17 to model the impact of phase noise on EVM values of the detected signal

3.3. RoF based on PMLLD using coherent and non-coherent receivers at 60 GHz

based on coherent receiver. Considering this formula, if one assumes that phase noise value at the receiver is high, then even if the SNR value is infinite, the EVM cannot approach zero, as it is shown in 3.20 assuming $PAPR = 1$

$$\lim_{SNR \rightarrow \infty} EVM = \sqrt{2 - 2 \exp\left(\frac{-\sigma^2}{2}\right)} \quad (3.20)$$

The model presented in 3.20 and the experimental results of EVM values versus SNR for coherent receiver and QPSK data at 200 Mbps are illustrated in Figure 3.11, a good agreement between simulation and experiments is achieved. In this figure, it can be seen that by increasing the SNR to very high values the EVM values are reaching an error floor. This error floor can be calculated using 3.20. The error floor of 10 % corresponds to an RMS phase error of 5.7° obtained from 3.20 assuming infinite SNR.

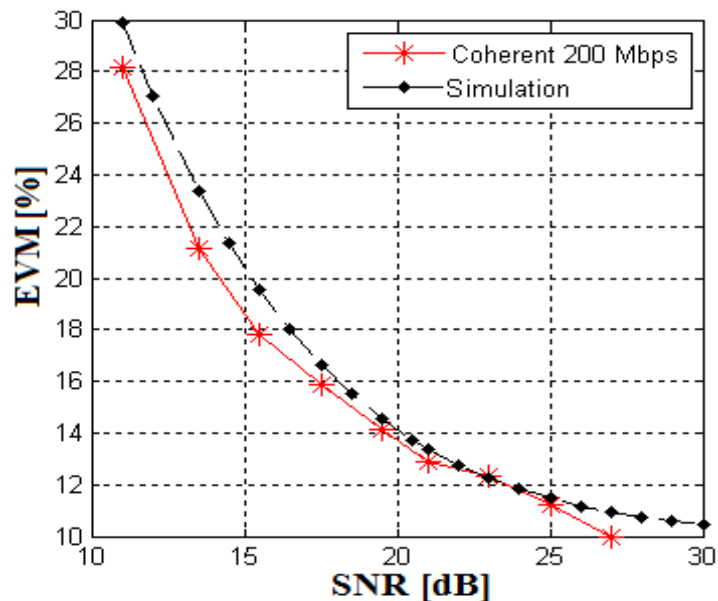


Figure 3.11 – EVM versus SNR for simulation and experimental measurement results, for coherent receiver with data rate of 200 Mbps.

Beside phase noise, the harmonics or spurious due to the mixing stage that may appear using coherent receiver (see Figure 3.3) are considered as the other weak spot of this down-conversion technique, comparing to non-coherent receiver method. If these harmonics locate on the same frequency band as desired IF signal, the EVM value will be impressively increased as it is shown in Figure 3.9.

3.4 RoF at W band based on non-coherent receiver

W frequency band is attracting more attentions due to its wide available bandwidth (75-110 GHz). There are many applications using W frequency band such as: satellite communication, W band radar research, radar targeting and tracking and also non military applications for high data rate systems ([10]-[12]).

In this section, a W band RoF system based on two free running DFB lasers and a non-coherent detector is presented. Many RoF systems based on coherent detection at W band have been studied recently ([7]-[9]), but few works contributed to RoF W band using non-coherent receiver, to our knowledge.

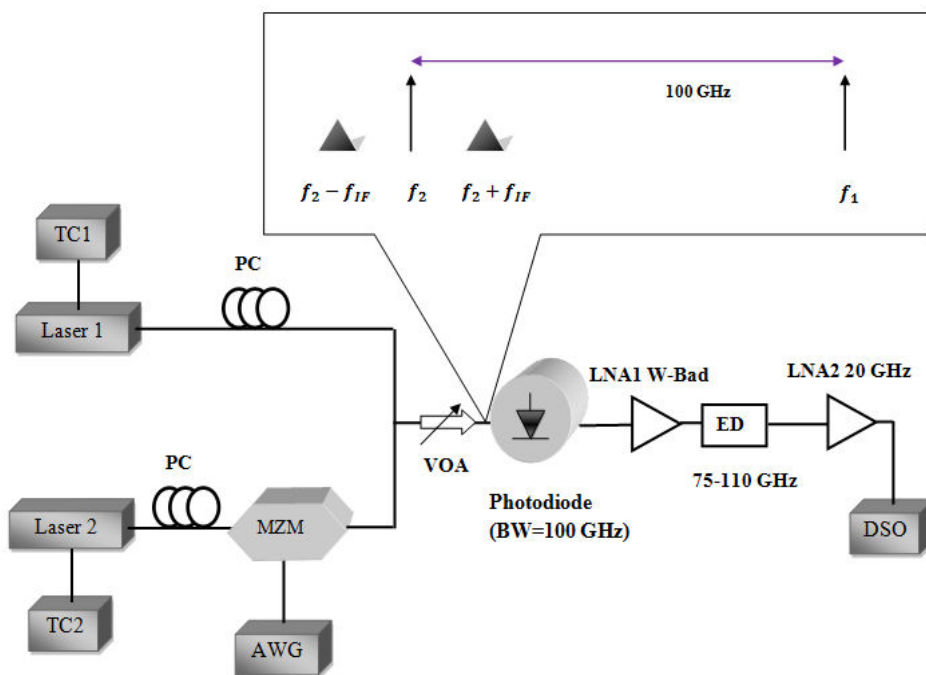


Figure 3.12 – W-band RoF based on two DFBs and non-coherent receiver.

3.4.1 Experimental results

The W-band RoF system is presented in Figure 3.12. In order to generate the signal at 100 GHz, two DFB lasers are used and the frequency distance between the two modes is controlled by temperature controller of the two lasers (TC1 and TC2). By choosing $\Delta\lambda = 0.8\text{nm}$ we can set the frequency distance to 100 GHz ($\Delta f = 100\text{ GHz}$). The IF is set at 4.5 GHz so the beating between the laser # 1's mode and the upper side band of the signal at the output of MZM will generate a frequency at 95.5 GHz at the output of the PD. At the receiver, a zero bias ED (75-110 GHz), utilizing schottky barrier beam lead diode, is used to down convert the signal from mm-wave frequency to IF. Before the ED a W-band LNA is used to increase the signal level so that the ED can detect the signal. EVM values of the down-converted signal are measured

3.4. RoF at W band based on non-coherent receiver

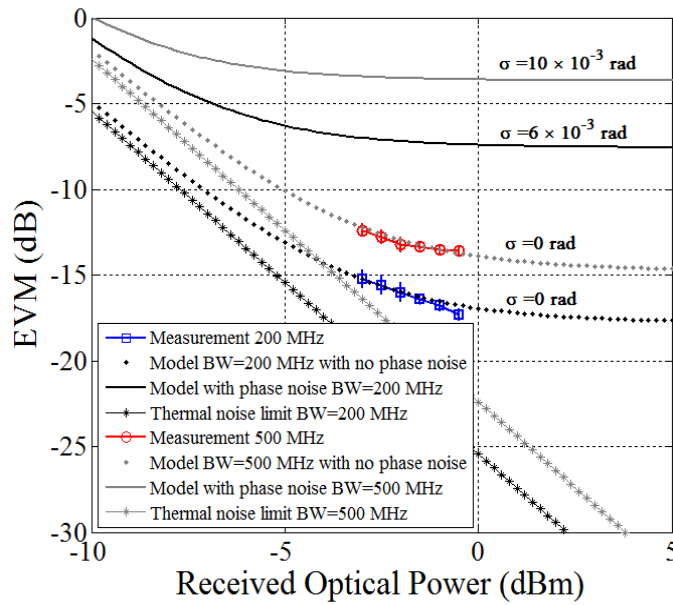


Figure 3.13 – EVM versus received optical power for 16QAM modulation scheme in the RoF W-band system.

using VSA and DSO.

The system performance is verified for various bit rates and received optical powers. For a fixed length of optical fiber, the received optical power is varied by changing attenuation value of the VOA and the EVM values are monitored by plotting them versus different values of the received optical power. Using this technique, one can determine impact of different noise on the performance of the RoF system under test. This technique is well studied in our work that is presented in [13], where we have proposed a method to determine the origin of the noise which has the most impact on EVM. This method is based on analyzing the trends of EVM versus received optical power. The details of this technique are presented in the next chapter. Fig. 3.13 shows the trend of EVM values versus received optical power for different scenarios. The EVM values are measured at 200 Mbps (square points) and 1 Gbps (circle points) for 16QAM modulation scheme and IF of 4.5 GHz. It can be seen that for the same received optical power, the EVM value for 200 Mbps (-17 dB for -0.5 dBm optical power) is much lower than that for 1 Gbps (-14 dB for -0.5 dBm optical power). The reason the EVM value increases is that for measuring EVM for the signals with higher data rates, we need to increase the bandwidth of the VSA while receiving the same optical power which reduces SNR. For example, for data rate of 200 Mbps the VSA's bandwidth is set to 200 MHz while for 1 Gbps its bandwidth is set to 500 MHz. As can be seen in this figure, the models with no phase noise impact (phase noise variance $\sigma = 0$) well match the measurement results for both 200 Mbps and 1 Gbps data rates. By setting σ to 6×10^{-3} rad and 10×10^{-3} rad, which correspond to the rms phase jitter of a signal generator with broadband phase noise equals -130 dBc/Hz over 200 MHz and 500 MHz

Chapter 3. Impact of Phase Noise in RoF System Based on PMLLD

bandwidths [14], one can see that for the same received optical power the EVMs are increased to much higher values, especially for large values of received optical power. This shows that using the non-coherent receiver in this RoF system we could successfully overcome the phase noise impact on performance of the system. In this figure, the star point lines show the EVM evolution versus the received optical power when there is no phase and no optical (RIN, shot) noise impact on the received signal. In this case, the only noise that impacts the performance of the system is the receiver thermal noise.

The OOK modulation is also tested on this RoF system at 100 GHz. Figure 3.14 represents the eye diagram of the OOK data at the output of ED and for different data rates (A) 100 Mbps (B) 400 Mbps (C) 1 Gbps (D) 2 Gbps. The results are showing well open eye upto 1 Gbps. By increasing the data rate to 2 Gbps, the eye opening is reducing which is caused by the limited bandwidth of the ED.

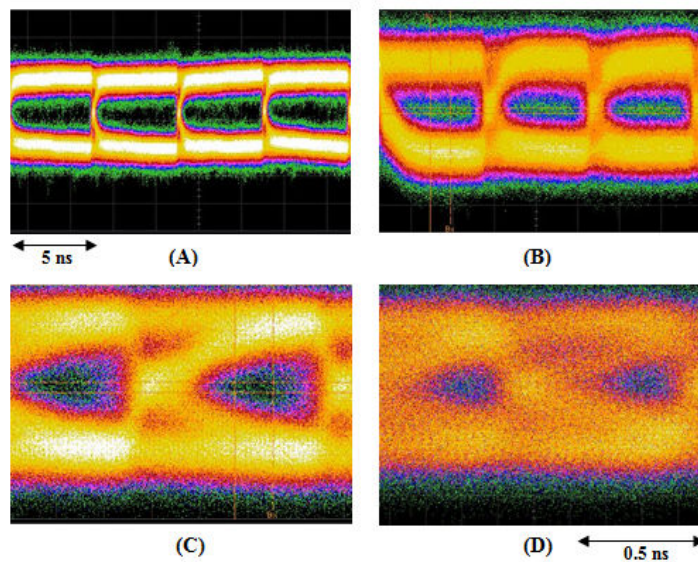


Figure 3.14 – Eye diagram for different data rates (A) 100 Mbps (B) 400 Mbps (C) 1 Gbps (D) 2 Gbps.

3.5 Conclusion

In this chapter, a 60 GHz RoF communication system based on PMLLD and a W band RoF system based on two DFB lasers are proposed. The performances of coherent and non-coherent electrical down-conversion methods used in 60 GHz RoF system are compared from phase noise point of view. It is shown, in theory and experimental demonstration, that using non-coherent receiver the impact of phase noise of PMLLD on EVM is highly reduced and as result for the same received optical power the EVM impressively decreased. By comparing the two different receivers for an RoF based on PMLLD at 60 GHz, it is concluded that even if very high SNR is achieved, the phase noise highly degrades the performance of the system and so it acts as a limit for improving the fulfilment of the RoF system. A Q factor of more than 8 is demonstrated for non-coherent receiver using OOK modulation and data rate of 500 Mbps. Finally, a W band RoF system based on two free running DFB lasers and non-coherent receiver is demonstrated. Using a non-coherent receiver at the receiver side, we could successfully overcome the phase fluctuations caused by two free running lasers in this communication system. On the other hand, using non-coherent receiver, the down-conversion is done without utilizing any local oscillator at 100 GHz which highly reduces the cost and complexity of the system.

The results of this chapter are published in:

Khayatzadeh, R., Poette, J., and Cabon, B. (2014). "Impact of phase noise in 60-GHz Radio-over-Fiber communication system based on passively mode-locked laser,". *IEEE Journal of Lightwave Technology*, 32(20), 3529-3535.

Khayatzadeh, R., Poette, J., Rzaigui, H., and Cabon, B. (2013). "Coherent and non-coherent receivers in 60-GHz RoF system based on passively mode-locked laser". *IEEE Microwave Photonics (MWP)*, Alexandria, VA, USA, 138-141.

Bibliography

- [1] F. Brendel, T. Zwick, J. Poette, and B. Cabon, "PLL-Stabilized optical communications in millimeter-wave RoF systems," *IEEE J. Opt. Commun. Netw.*, vol. 6, no. 1, pp. 45–53, Jan. 2014.
- [2] "Error Vector Magnitude." Wikipedia, The Free Encyclopedia. Wikimedia Foundation, Inc. 20 April 2015.
- [3] Available: <http://www.ecma-international.org/publications/standards/Ecma-387.htm>
- [4] A. Georgiadis, "Gain, phase imbalance, and phase noise effects on error vector magnitude," *IEEE Trans. Veh. Technol.*, vol. 53, no. 2, pp. 443-449, March 2004.
- [5] "Constellation diagram." Wikipedia, The Free Encyclopedia. Wikimedia Foundation, Inc. 20 April 2015.
- [6] Govind P. Agrawal, "Lightwave technology telecommunication systems" Hoboken, NJ, USA: Wiley, 2005.
- [7] H. Huang, C. Lin, C. Ho, W. Liang, C. Wei, Y. Cheng, and S. Chi, "High spectral efficiency W-band OFDM-RoF system with direct-detection by two cascaded single-drive MZMs," *Optics Express*, vol. 21, no. 14, July 2013.
- [8] A. Kanno, K. Inagaki, I. Morohashi, T. Sakamoto, T. Kuri, I. Hosako, T. Kawanishi, Y. Yoshida, and K. Kitayama, "40 Gb/s W-band (75-110 GHz) 16-QAM radio-over-fiber signal generation and its wireless transmission," *Optics Express*, vol. 19, no. 26, July 2011.
- [9] X. Pang, A. Caballero, A. Dogadaev, V. Arlunno, L. Deng, R. Borkowski, J. S. Pedersen, D. Zibar, X. Yu, and I. T. Monroy, "25 Gbit/s QPSK hybrid fiber-wireless transmission in the W-band (75-110 GHz) with remote antenna unit for in-building wireless networks," *IEEE photon. J.*, vol. 4, no. 3, June 2012.
- [10] H. Essen, M. Brautigam, R. Sommer, and A. Wahlen, "SUMATRA, a W-band SAR for UAV application" *Radar Conference-Surveillance for a Safer World, 2009. RADAR. International*. pp. 48-48, IEEE, 2009.
- [11] S. Myers, and R. Z. Ramos, "Application of W-band, Doppler Radar to Railgun Velocity Measurements," *Procedia Engineering*, vol. 58, pp. 369-376, 2013.

Bibliography

- [12] A. Kanno, et al., "40 Gb/s W-band (75-110 GHz) 16-QAM radio-over-fiber signal generation and its wireless transmission" *Optics Exp.*, vol. 19, no. 26, pp. 1-3, July 2011.
- [13] R. Khayatzadeh, H. Hallak Elwan J. Poette, and B. Cabon, "Impact of amplitude noise in millimeter-wave Radio-over-Fiber systems" *IEEE J. Lightw. Technol.*, DOI: 10.1109/JLT.2015.2422572, Apr. 2015.
- [14] W. Kester, "Converting oscillator phase noise to time jitter" Analog Devices, MA, USA, Tech. Rep. MT-008, 2009.

4 Impact of Amplitude Noise in Millimeter-Wave Radio over Fiber Systems

4.1 Introduction

Phase noise in a radio over fiber system at mm-wave frequencies is well studied in two previous chapters. In Chapter 2, the phase noise of the carrier at mm-wave frequency, which is generated using heterodyne technique, is measured utilizing our new digital phase noise measurement technique. In Chapter 3, a non-coherent receiver is proposed in order to overcome the phase noise impact on the performance of the RoF system based on PMLLD and free running lasers. This receiver is tested for both 60 GHz and 100 GHz frequency bands and different modulation schemes. Using non-coherent receiver, the impacts of phase noise on EVM results is removed [1], while the amplitude noise is still degrading the performance of the RoF system based on this type of receivers. In this chapter, a complete theoretical and experimental study of amplitude noise impact on performance of RoF communication systems in mm-wave frequency band is presented. A simulation method is also presented that can determine the origin of the amplitude noise which has the most impact on EVM values. The impact of different optical and electrical noise such as relative intensity noise (RIN), shot noise and thermal noise on EVM is precisely studied employing experimental and theoretical analysis. In the proposed RoF system, two techniques are used to generate mm-wave signal and the EVM results are compared from amplitude noise viewpoint. In the first technique, two independent DFB lasers are used to generate mm-wave carrier signal at the output of a PD, and the second technique is based on a PMLLD. Impact of optical sources phase noise on performance of the system is removed using a non-coherent down-conversion method. Finally, using this method that is proved here, a very good matching between the experimental and the simulation results is observed.

4.2 Different amplitude noise in RoF systems

The amplitude noise in an RoF system can be divided into two main types. The optical noise and the electrical noise. The optical noise are those which have optical origin such as laser excess noise and spontaneous emission which are characterized by relative intensity noise (RIN), and the electrical noise are those which have electrical origin like thermal noise. We also can mention the shot noise which can be considered as both electrical and optical noise. The total system noise is the linear summation of these two noise groups as they can be considered independent. In this section these noise groups are studied very briefly.

4.2.1 Relative intensity noise (RIN)

The output power or intensity of a laser always contains some fluctuations due to quantum noise and fluctuations of various technical origins [2]. In a receiver, laser intensity fluctuations can cause noise that exceeds the thermal noise of the load impedance of the receiver PD. Thus, these fluctuations can become a limiting factor for optimizing performance of RoF system.

Relative intensity noise (RIN) describes these power fluctuations as:

$$RIN = \frac{\langle \Delta P^2 \rangle}{P_{opt}^2} \quad (4.1)$$

where $\langle \Delta P^2 \rangle$ is the mean-square optical intensity fluctuation in 1 Hz bandwidth at a specified frequency and P_{opt} is the average optical power. The mean squared noise current from a PD with responsivity of R caused by RIN can be written as:

$$\sigma_{RIN}^2 = 10^{RIN_{dB}/10} I^2 \Delta f = 10^{RIN/10} R^2 P_{opt}^2 \Delta f \quad (4.2)$$

where I is replaced by RP_{opt} and Δf is bandwidth of measurement.

4.2.2 Shot noise

The fluctuation of number of photons detected by PD is called shot noise. This comes from discretization of electromagnetic energy in terms of photons. For a system at a given temperature, the shot noise varies with average power. The mean squared noise current from a PD

is:

$$\sigma_{shot}^2 = 2qI\Delta f \quad (4.3)$$

where q is the electron charge (1.6e-19 coulomb), I is average output current of PD, and Δf is bandwidth of measurement. Considering a PD at the receiver side with responsivity of R , one can rewrite 4.3 as:

$$\sigma_{shot}^2 = 2qRP_{opt}\Delta f \quad (4.4)$$

4.2.3 Thermal noise

Thermal noise or Nyquist noise is generated as a result of thermal fluctuation of the electrons within a conductor. The thermal noise occurs regardless of the applied voltage to the conductor and its value only depends on temperature and resistance value of the conductor. The mean squared noise current from load resistance R_L is:

$$\sigma_{thermal}^2 = \frac{4kTF\Delta f}{R_L} \quad (4.5)$$

where k , T , F and Δf are Boltzmann constant, temperature, amplifier noise figure and received signal bandwidth, respectively.

4.3 Global SNR in RoF system based on two DFB lasers

The schematic of the suggested RoF system based on two DFB lasers is presented in Figure 4.1. In this figure, the electrical fields of the two lasers are $E_1(t)$ and $E_2(t)$:

$$E_1(t) = \left(E_1 + \epsilon_1(t) \right) \exp \left(j(2\pi f_1 t + \phi_1) \right) \quad (4.6)$$

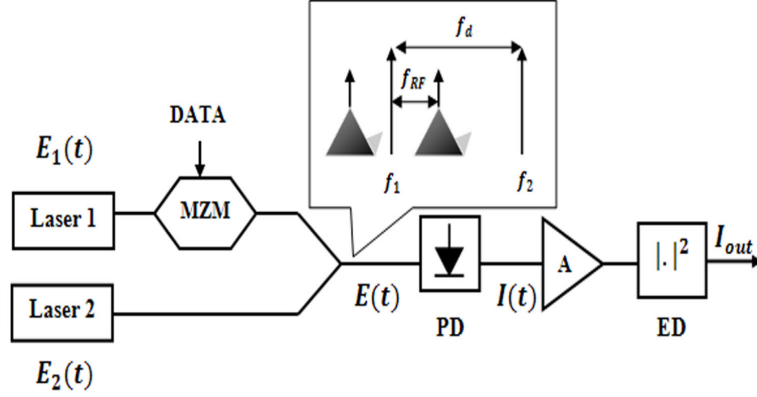


Figure 4.1 – Schematic of RoF communication system based on two DFB lasers and non-coherent receiver, MZM: Mach-Zehnder Modulator, PD: Photo diode, A: Amplifier, ED: Envelope detector

$$E_2(t) = (E_2 + \epsilon_2(t)) \exp(j(2\pi f_2 t + \phi_2)) \quad (4.7)$$

where E_i , ϵ_i , f_i and ϕ_i , ($i = 1, 2$), are the field amplitude, amplitude noise, carrier frequency, and phase fluctuation, respectively.

As it is shown in this figure, the output light of laser # 1 is externally modulated by digital signals such as BPSK or QPSK at Radio-Frequency (RF) using an MZM. The signal at the output of the MZM can be expressed as:

$$E_{M1} = \frac{1}{2} (E_1 + \epsilon_1(t)) \exp(j(2\pi f_1 t + \phi_1)) (1 + \exp(j\Delta\phi(t))) \quad (4.8)$$

$$\Delta\phi(t) = \frac{\pi}{V_\pi} V(t) \quad (4.9)$$

where $V(t)$ is the applied voltage to the MZM and V_π is the required voltage to tune MZM from minimum to maximum transmission to cause a phase shift of 180° . Considering that the MZM is biased in the linear region ($V_{DC} = \frac{V_\pi}{2}$) then:

$$V(t) = \frac{V_\pi}{2} + v(t) \quad (4.10)$$

where $v(t)$ is a small signal, then the cosine of the data signal can be expressed as following:

$$\cos \Delta\phi(t) \approx -\frac{\pi}{V_\pi} v(t) \quad (4.11)$$

The optical spectrum of the combined optical signals from two lasers is illustrated in Figure 4.1. At the base station, beating between the modes is done utilizing a PD. Output current of the PD, with responsivity of R , can be found as:

$$I(t) = R |E(t)|^2 = R \left[\frac{1}{2} (E_1 + \epsilon_1(t))^2 (1 + \cos(\Delta\phi(t))) + (E_2 + \epsilon_2(t))^2 + 2(E_1 + \epsilon_1(t))(E_2 + \epsilon_2(t)) \cos\left(\frac{\Delta\phi(t)}{2}\right) \cos\left(2\pi f_d t + \phi_2 - \phi_1 - \frac{\Delta\phi(t)}{2}\right) \right] \quad (4.12)$$

The first two terms in 4.12 are baseband signals, so they will be experimentally filtered out after passing through low noise amplifier (A) whose center frequency is at 60 GHz and its bandwidth is limited to some GHz. The last term with carrier frequency equals the frequency distance between the two main optical modes, $f_d = f_2 - f_1 = 60$ GHz, is amplified and then detected by a square law ED. Assuming an ideal ED, the signal at output of ED can be written as:

$$S_{out}(t) = |I_{filtered}(t)|^2 = 4R^2 (E_1 + \epsilon_1(t))^2 (E_2 + \epsilon_2(t))^2 \cos^2\left(\frac{\Delta\phi(t)}{2}\right) \times \left(\frac{1 + \cos\left(2\pi 2f_d t + 2(\phi_2 - \phi_1) - \Delta\phi(t)\right)}{2} \right) \approx R^2 \left(E_1^2 E_2^2 + 2E_1^2 E_2 \epsilon_2(t) + 2E_2^2 E_1 \epsilon_1(t) - \frac{E_1^2 E_2^2 \pi}{V_\pi} v(t) \right) \quad (4.13)$$

Equation 4.13 is found by neglecting the second order terms, $\epsilon_i(t)\epsilon_j(t)$ and $\epsilon_i(t)v(t)$ ($i,j=1,2$) and filtering the high frequency term.

Observing 4.13, one can conclude that using an ED, the transmitted data can be recovered from the intensity of the mm-wave signal, free of phase noise impacts, $\phi_2 - \phi_1$. However, the amplitude fluctuation reminds the main disturbing term.

The power spectral density (PSD) of S_{out} can be easily found since the two lasers are independent, so there is no need of cross-correlation calculation. The signal to noise ratio as a function of frequency is presented as:

$$SNR(\omega) = \frac{\frac{E_1^2 E_2^2 \pi^2}{4V_\pi^2} S_v(\omega)}{E_2^2 S_{e_1}(\omega) + E_1^2 S_{e_2}(\omega)} \quad (4.14)$$

where $S_{e_1}(\omega)$, $S_{e_2}(\omega)$ and $S_v(\omega)$ are the PSD of amplitude noise of laser # 1, laser # 2 and the PSD of signal, respectively. Observing 4.14, one can conclude that the SNR in RoF based on two independent DFBs and ED depends on the intensity noise of each DFB.

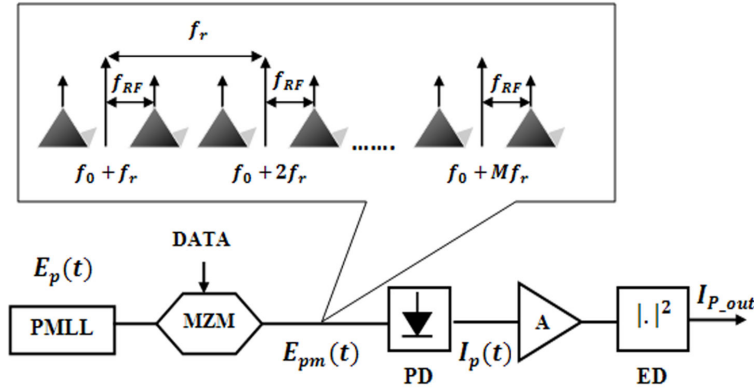


Figure 4.2 – Schematic of RoF communication system based on PMLLD and non-coherent receiver, MZM: Mach-Zehnder Modulator, PD: Photo diode, A: Amplifier, ED: Envelope detector

4.4 Global SNR in RoF system based on PMLLD

Figure 4.2 depicts the schematic of an RoF system based on PMLLD. As it is shown, the PMLLD produces many optical modes at its output. Thus, using a single PMLLD laser, the mm-wave signal can be generated at the output of the PD by mode beating. The optical frequency distance between the adjacent modes corresponds to the repetition frequency of the PMLLD, f_r . The electrical field of a PMLLD consisting of M modes can be described as follows:

$$E_p(t) = \exp\left(j(2\pi f_0 t)\right) \sum_{n=0}^{M-1} E_n(t) \exp\left(j(2\pi f_r n t + \phi_n(t))\right) \quad (4.15)$$

where

$$E_n(t) = E_n + \epsilon_n(t) \quad (4.16)$$

and f_0 is the first mode carrier frequency, E_n , $\epsilon_n(t)$ and ϕ_n are the field amplitude, amplitude fluctuation and the relative phase fluctuation of the n th lasting point, respectively.

The signal at the output of the MZM can be expressed as:

$$E_{mp}(t) = \frac{1}{2} \exp(j(2\pi f_0 t + \theta)) \left[1 + \exp(j\Delta\phi(t)) \right] \times \sum_{n=0}^{M-1} E_n(t) \exp(j(2\pi n f_r t + \phi_n(t))) \quad (4.17)$$

The spectrum of the signal at the output of modulator is also shown in this figure. At the base station, beating between the modes is done utilizing a PD. Since bandwidth of the PD is less than $2f_r$, the terms with frequencies higher than $2f_r$ are filtered out by the PD. The low frequency term also will be experimentally filtered out after passing through a low noise amplifier, the amplified signal is then detected by an ED. The output signal of ED can be written as:

$$\begin{aligned} S_{p-out}(t) &= \left| I_{filtered}(t) \right|^2 = R^2 \left(1 + \cos \Delta\phi(t) \right)^2 \left[\sum_{i=0}^{M-2} E_{i+1}(t) E_i(t) \cos(2\pi f_r t + \phi_{i+1} - \phi_i) \right]^2 \\ &= R^2 \left(1 + \cos \Delta\phi(t) \right)^2 \left[\sum_{i=0}^{M-2} E_{i+1}(t) E_i(t) \cos(2\pi f_r t + \phi_{i+1} - \phi_i) \right] \\ &\times \left[\sum_{j=0}^{M-2} E_{j+1}(t) E_j(t) \cos(2\pi f_r t + \phi_{j+1} - \phi_j) \right] \\ &= R^2 \left(1 + \cos \Delta\phi(t) \right)^2 \sum_{i=0}^{M-2} \sum_{j=0}^{M-2} E_{i+1}(t) E_i(t) E_{j+1}(t) E_j(t) \\ &\times \left(\cos(2\pi 2f_r t + 2(\phi_{i+1} - \phi_i)) + \cos((\phi_{i+1} - \phi_i) - (\phi_{j+1} - \phi_j)) \right) \\ &= R^2 \left(1 + \cos \Delta\phi(t) \right)^2 \sum_{i=0}^{M-2} \sum_{j=0}^{M-2} E_{i+1}(t) E_i(t) E_{j+1}(t) E_j(t) \quad (4.18) \end{aligned}$$

The high frequency terms of $S_{p-out}(t)$ are filtered out by the low pass filter (LPF) of the ED and

Chapter 4. Impact of Amplitude Noise in Millimeter-Wave Radio over Fiber Systems

the phase noise term is approximately zero $((\phi_{i+1} - \phi_i) - (\phi_{j+1} - \phi_j)) \approx 0$ [1]. Theory in 4.18 shows that a receiver based on ED is completely robust against the laser phase noise effects. In previous chapter, it is experimentally shown that, using an ED, the laser phase noise effects on the quality of the received signal can be neglected.

By substituting 4.16 into 4.18, one can find the S_{p-out} in function of noise and signal terms. By neglecting the terms $\epsilon_i(t)\epsilon_j(t)$, we rewrite summation term in 4.18 as follows:

$$\begin{aligned} \sum_{i,j} E_{i+1}(t)E_i(t)E_{j+1}(t)E_j(t) &\approx \sum_{i,j} (E_{i+1}E_i + E_{i+1}\epsilon_i + E_i\epsilon_{i+1})(E_{j+1}E_j + E_{j+1}\epsilon_j + E_j\epsilon_{j+1}) \\ &= \sum_{i,j} (E_iE_{i+1}E_jE_{j+1} + E_iE_{i+1}(E_{j+1}\epsilon_j + E_j\epsilon_{j+1}) + E_jE_{j+1}(E_{i+1}\epsilon_i + E_i\epsilon_{i+1})) \\ &= \sum_{i,j} (E_iE_{i+1}E_jE_{j+1} + 2E_iE_{i+1}E_j\epsilon_{j+1}(t) + 2E_iE_{i+1}E_{j+1}\epsilon_j(t)) \end{aligned} \quad (4.19)$$

where

$$\sum_{i,j} 2E_iE_{i+1}E_j\epsilon_{j+1}(t) + 2E_iE_{i+1}E_{j+1}\epsilon_j(t) = \sum_{i,j} 2E_iE_{i+1}(E_{j-1} + E_{j+1})\epsilon_j(t) \quad (4.20)$$

To justify 4.20, we just can try this equation for some j values and take to account that $E_M = 0$ and $E_j = 0$ for $j < 0$.

Substituting 4.19 and 4.20 into 4.18 one can drive 4.21.

$$\begin{aligned} S_{p-out}(t) &\approx R^2 \left[\sum_{i,j} E_{i+1}E_iE_{j+1}E_j \right] + R^2 \left[\sum_{i,j} 2E_{i+1}E_i(E_{j-1} + E_{j+1})\epsilon_j(t) \right] \\ &\quad - \frac{R^2\pi}{V\pi} \left[\sum_{i,j} E_{i+1}E_iE_{j+1}E_j \right] v(t) \end{aligned} \quad (4.21)$$

The first term in 4.21 is a DC term, second term represents the amplitude noise term and the last term contains the data signal links with $v(t)$. PSD of S_{p-out} can be calculated by Fourier transform of its auto-correlation function. Finding the PSD of the DC term and the term containing data signal in 4.21 is straight forward since they do not contain any random variable. Assuming that the amplitude fluctuations are stationary [3], the noise term auto-correlation function can be calculated as:

$$n(t) = \sum_{i,j} E_{i+1} E_i (E_{j-1} + E_{j+1}) \epsilon_j(t) \quad (4.22)$$

$$\begin{aligned} \gamma_{nn}(\tau) &= \langle n(t)n(t+\tau) \rangle \\ &= \left\langle \left[\sum_{i,j} E_{i+1} E_i (E_{j-1} + E_{j+1}) \epsilon_j(t) \right] \left[\sum_{m,n} E_{n+1} E_n (E_{m-1} + E_{m+1}) \epsilon_m(t+\tau) \right] \right\rangle \\ &= \sum_{i,j,m,n} K_{i,j,m,n} \langle \epsilon_j(t) \epsilon_m(t+\tau) \rangle = \sum_{i,j,m,n} K_{i,j,m,n} \langle \epsilon_j(t) \epsilon_j(t+\tau) \rangle \\ &\quad + \sum_{i,j,m,n} K_{i,j,m,n} \langle \epsilon_j(t) \epsilon_m(t+\tau) \rangle \quad (4.23) \end{aligned}$$

where

$$K_{i,j,m,n} = \sum_{i,j,m,n} \left(4E_{i+1} E_i E_{n+1} E_n (E_{j-1} + E_{j+1}) (E_{m-1} + E_{m+1}) \right) \quad (4.24)$$

and $n(t)$ is the noise term, $\gamma_{nn}(\tau)$ is the auto-correlation function of the noise term and $\langle . \rangle$ denotes the mean value over time. The first term in 4.23 is the summation of the auto-correlation functions of individual modes amplitude fluctuation and the last term shows the summation of cross-correlation functions among different modes amplitude fluctuation. One can find PSD of noise term by taking the Fourier transform of 4.23.

$$\begin{aligned} S_n(\omega) &= \left(\sum_{i,j,m,n} K_{i,j,m,n} FT \left[\langle \epsilon_j(t) \epsilon_j(t+\tau) \rangle \right] \right. \\ &\quad \left. + \sum_{i,j,m,n} K_{i,j,m,n} FT \left[\langle \epsilon_j(t) \epsilon_m(t+\tau) \rangle \right] \right) \quad (4.25) \end{aligned}$$

where $FT[]$ denotes the Fourier transform.

$$FT \left[\langle \epsilon_j(t) \epsilon_j(t + \tau) \rangle \right] = S_{\epsilon_j}(\omega) \quad (4.26)$$

and

$$FT \left[\langle \epsilon_j(t) \epsilon_m(t + \tau) \rangle \right] = S_{\epsilon_j \epsilon_m}(\omega) \quad (4.27)$$

There, the noise PSD becomes:

$$S_n(\omega) = \left(\sum_{\substack{i,j,m,n \\ j=m}} K_{i,j,m,n} S_{\epsilon_j}(\omega) + \sum_{\substack{i,j,m,n \\ j \neq m}} K_{i,j,m,n} S_{\epsilon_j \epsilon_m}(\omega) \right) \quad (4.28)$$

and the detected signal PSD is:

$$S(\omega) \approx R^4 C_{i,j}^2 \delta(\omega) + R^4 S_n(\omega) + \frac{R^4 \pi^2}{V_\pi^2} C_{i,j}^2 S_v(\omega) \quad (4.29)$$

where

$$C_{i,j} = \sum_{i,j} E_{i+1} E_i E_{j+1} E_j \quad (4.30)$$

$S(\omega)$, $S_n(\omega)$ and $S_v(\omega)$ are the PSDs of the detected signal, noise term and the data signal, respectively. In 4.27, $S_{\epsilon_j}(\omega)$ is the PSD of amplitude fluctuation of the j th mode taken alone and $S_{\epsilon_j \epsilon_m}(\omega)$ presents the cross-power spectrum between amplitude fluctuation of two different modes. One can express the SNR as a function of frequency as:

$$SNR(\omega) = \frac{\frac{\pi^2}{V_{\pi}^2} C_{i,j}^2 S_v(\omega)}{S_n(\omega)} \quad (4.31)$$

According to 4.31, the performance of an RoF system based on PMLLD and ED is limited by individual modes amplitude fluctuation power and cross-power between amplitude fluctuation of two different modes.

4.5 EVM in an RoF system based on non-coherent receiver

In this section, impacts of different noise on EVM values for two different RoF systems are studied. The first system is based on two DFB lasers and the second system is based on PMLLD. In order to observe the impact of different types of noise on EVM, the following formula is used [4]:

$$EVM = \sqrt{\frac{1}{SNR} + 2 - 2 \exp\left(\frac{-\sigma^2}{2}\right)} \sqrt{\frac{1}{PAPR}} \quad (4.32)$$

where SNR is signal to noise ratio, σ is rms value of phase noise and PAPR is the peak to average power ratio for the considered modulation scheme. In previous sections, we have shown that the impact of phase fluctuations on received signal can be vanished using an ED, so by replacing σ with zero and considering QPSK modulation (PAPR=1), 4.32 can be rewritten as:

$$EVM = \sqrt{\frac{1}{SNR}} \quad (4.33)$$

Theory of laser intensity noise impact on SNR is studied in previous sections. However, in practice, all receivers are subjected to thermal noise and shot noise as well as received intensity noise of lasers. So the total current noise variance at the receiver can be considered as:

$$\sigma_{noise}^2 = \sigma_{thermal}^2 + \sigma_{shot}^2 + \sigma_{RIN}^2 \quad (4.34)$$

The signal power (S) is:

$$S = R^2 P_{opt}^2 R_L \quad (4.35)$$

Using 4.34 and 4.35, the SNR can be written as:

$$SNR = \frac{S}{\sigma_{noise}^2} = \frac{R^2 P_{opt}^2}{\frac{4kTF\Delta f}{R_L} + 2qRP_{opt}\Delta f + 10^{RIN/10} R^2 P_{opt}^2 \Delta f} \quad (4.36)$$

Substituting 4.36 into 4.33, the EVM dependence upon the received optical power and amplitude noise can be shown. Thus, by plotting the EVM versus the received optical power and comparing the trend of the curve with the theory in 4.33, one can determine the noise which has the most impact on EVM results. Equation 4.36 is a more complete description of noise compared to 4.14 and 4.31.

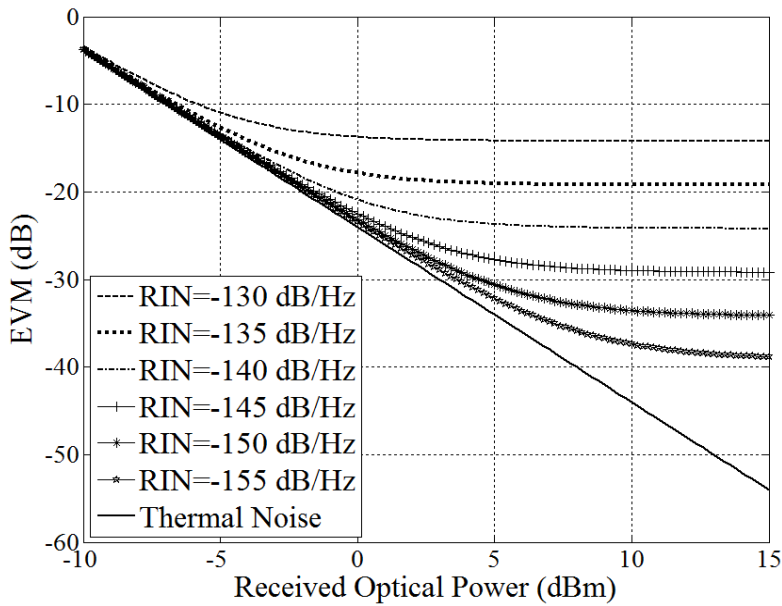


Figure 4.3 – EVM simulation results versus received optical power for different RIN values.

4.5.1 Simulation of EVM behaviour versus received optical power

In order to study the impact of different noise (optical and thermal) on behaviour of EVM values versus received optical power equation 4.36 is modelled using MATLAB.

Figure 4.3 illustrates the EVM evolution versus received optical power for different RIN values. In order to only observe the impact of RIN on EVM values the thermal noise for different RIN

4.5. EVM in an RoF system based on non-coherent receiver

values is set and fixed to -100 dBW and the impact of phase noise is neglected. Observing this figure, it can be seen that for the scenario in which the optical noise is set to zero (thermal noise the bold curve) the EVM (dB) is decreasing linearly with respect to received optical power which indicates that by increasing the received optical power the SNR is increasing and consequently the EVM values decrease. By increasing the RIN value an error floor can be observed. This error floor can be explained using 4.36, since in this equation the RIN power and the signal power are both proportional to the P_{opt}^2 and so increasing the received optical power makes the same increase for both RIN and signal power, especially when the RIN value is high, consequently the SNR and EVM values exhibit a plateau (constant value). Impact of different RIN values on the EVM error floor is also shown in this figure. For the laser with RIN value equals -155 dB/Hz the error floor starts from 8 dBm received optical power and reaches -39 dB, while for the laser with the RIN equals -130 dB/Hz this error floor starts from -2 dBm and reaches -14 dB. This figure proves that if the RIN value of the laser used in an RoF communication system is high, then we cannot improve the performance of the system by increasing the received optical power.

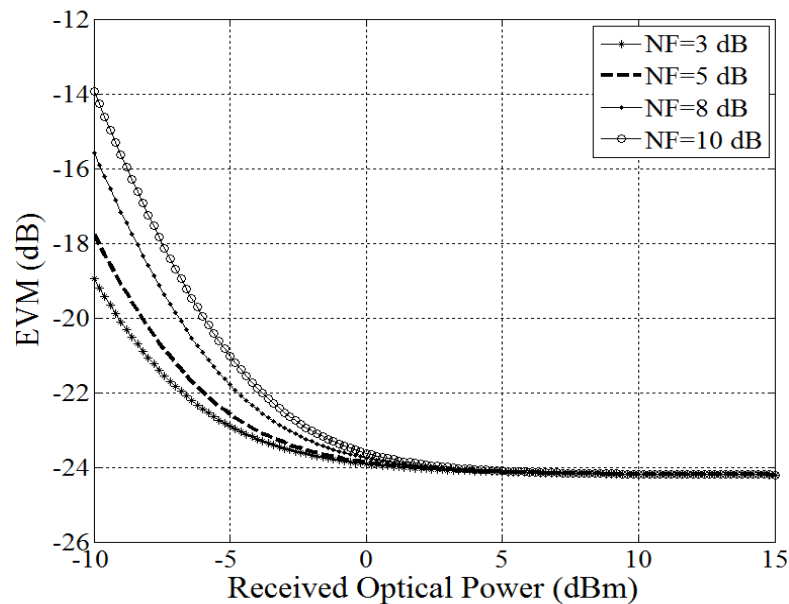


Figure 4.4 – EVM simulation results versus received optical power for different noise figure values of the LNA.

Figure 4.4 represents the EVM evolution versus received optical power for different thermal noise values. The thermal noise is changed by choosing different noise figure (NF) values for the LNA. The RIN is fixed at -140 dB/Hz and the phase noise impact on EVM values is neglected. As it is illustrated in this figure, one can see that the error floor remains constant for different NF values which shows that the thermal noise impact on EVM is more important for the low received optical powers. This is due to the fact that the impact of optical noise (RIN, shot) on performance of the system is low for low received optical powers while the thermal noise impact on EVM is independent of the received optical power value. By increasing the NF

value we can see that the EVM is increasing and this increase is larger for lower optical powers. For example, for received optical power of -5 dBm the EVM value difference between $NF = 3$ dB and $NF = 10$ dB is 2 dB while for optical power of -10 dBm the difference is 5 dB.

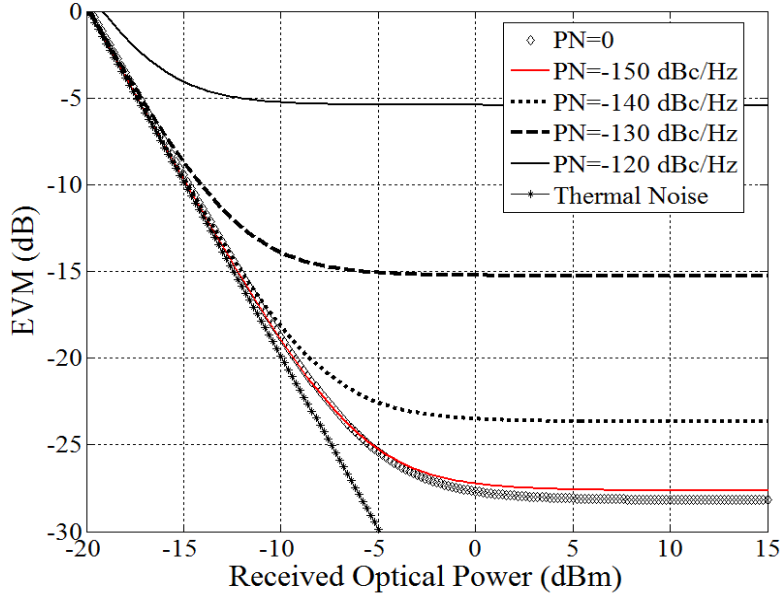


Figure 4.5 – EVM simulation results versus received optical power for different phase noise values.

Figure 4.5 represents the EVM evolution versus received optical power for different phase noise (PN) values. In this figure, the NF and RIN are set to 5 dB and -140 dB/Hz, respectively. Different rms jitter values are calculated considering four different broadband phase noise floors (-120 dBc/Hz, -130 dBc/Hz, -140 dBc/Hz and -150 dBc/Hz) then the integrated phase noise power in dBc is calculated considering 200 MHz bandwidth. Using following equation the rms jitter σ values are found in radians as [5]:

$$\sigma \approx \sqrt{2 \times 10^{\frac{A}{10}}} \tag{4.37}$$

where A is the integrated phase noise power in dBc.

Observing Figure 4.5, one can see that phase noise causes an error floor for high received optical powers. This error floor implies again here, as for RIN, that in an RoF system even if RIN is very low, increasing received optical power in order to improve SNR will not improve the performance of the system without reducing the phase noise. As can be seen in this figure, by increasing the broadband phase noise floor from -150 dBc/Hz to -140 dBc/Hz the EVM value is increased by 10 dB. This high sensitivity to phase noise can be explained using 4.32

which shows that EVM depends on rms phase noise jitter exponentially.

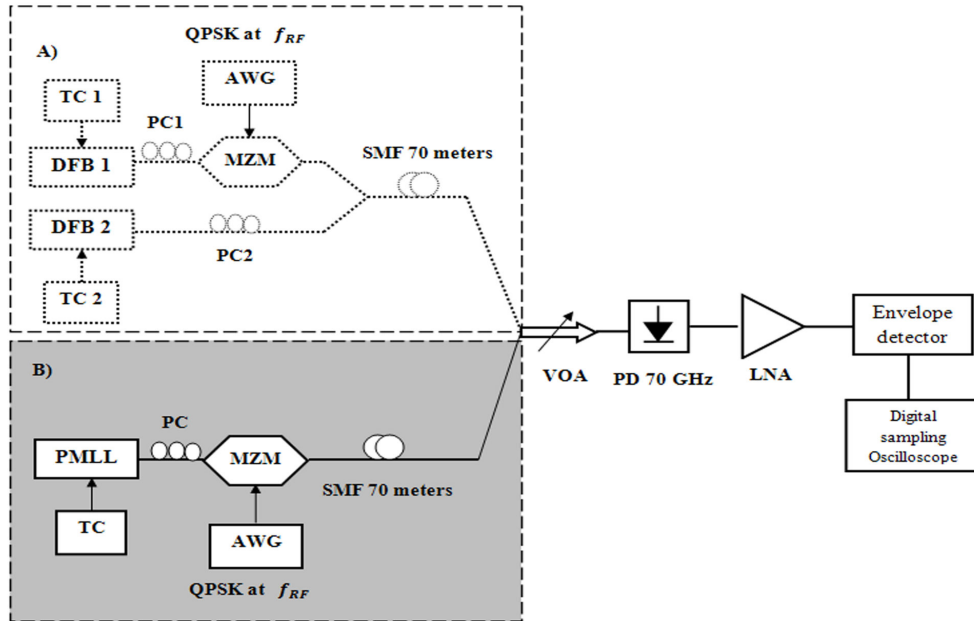


Figure 4.6 – Experimental setup of RoF communication system based on A) two DFB lasers B) PMLLD, TC: Temperature Controller, PC: Polarization Controller, MZM: Mach-Zehnder Modulator, AWG: Arbitrary Waveform Generator, SMF: Single Mode Fiber, VOA: Variable Optical Attenuator, LNA: Low Noise Amplifier.

4.5.2 Experimental setup and results

4.5.2.1 RoF based on two DFB lasers

Figure 4.6 (A) presents the experimental setup of RoF communication system based on two independent DFB lasers and an electrical non-coherent down-conversion stage using an ED. The frequency of the two lasers are controlled using temperature controllers (TC1 and TC2) in such a way that the frequency distance between the two optical modes is fixed at 60 GHz. The output light of the DFB one is externally modulated using an MZM and an AWG that is able to generate the QPSK signal at different RF frequencies. The light from the two lasers are then coupled into a 70 meter single mode fiber (SMF) using a 3-dB optical coupler. A 70 GHz PD is used to transform optical signal to electrical signal and also to generate mm-wave signal by heterodyning the optical modes generated by the two DFBs. Before the PD, a variable optical attenuator (VOA) is used in order to change the total received optical power at the PD. The electrical signal at the output of the PD is then amplified using a 24 dB gain LNA and the envelope of the amplified signal is extracted utilizing an ED, schottky barrier beam lead diode, in order to be sampled using a digital sampling oscilloscope (Agilent 54855A DSO, 6 GHz). The EVM values of the sampled signal is then measured using VSA software installed on the DSO.

4.5.2.2 RoF based on PMLLD

The experimental setup of the RoF system based on PMLLD is shown in Figure 4.6 (B). The repetition frequency of PMLLD is 60.9 GHz and the total achieved optical power is 9 dBm. The same external modulation and receiver setup is used as in previous section, by doing so all the modes are modulated. Beating between the modes is done using a PD of 70 GHz bandwidth, which also acts as a filter for higher order mode beating signals. EVM values are measured using VSA after being sampled by DSO.

4.5.2.3 Noise measurements

At the output of the PD the RIN is up converted to MMW frequency and then it appears as two side-bands around the carrier with frequency offset equals the relaxation frequency of the laser. The RIN is then down converted to IF using ED. Figure 4.7 depicts the power spectrum of the detected noise for three different scenarios; curve (1) presents the thermal noise with no light at the input of the PD, curve (2) shows the case of two DFB lasers and curve (3) is the case of PMLLD. Comparing curves (2) and (3), one can conclude that the generated optical noise of the PMLLD is much higher than that of the two DFBs at low frequency ($f < 1.5$ GHz). As it is shown in theory section, this conclusion is not general and depends on the intensity noise of the DFB and PMLLD lasers used in the RoF system which depends on biasing current of the lasers. Observing Figure 4.7, it can be seen that the noise power values for high frequencies are filtered out by the ED which acts like a low-pass filter, as predicted.

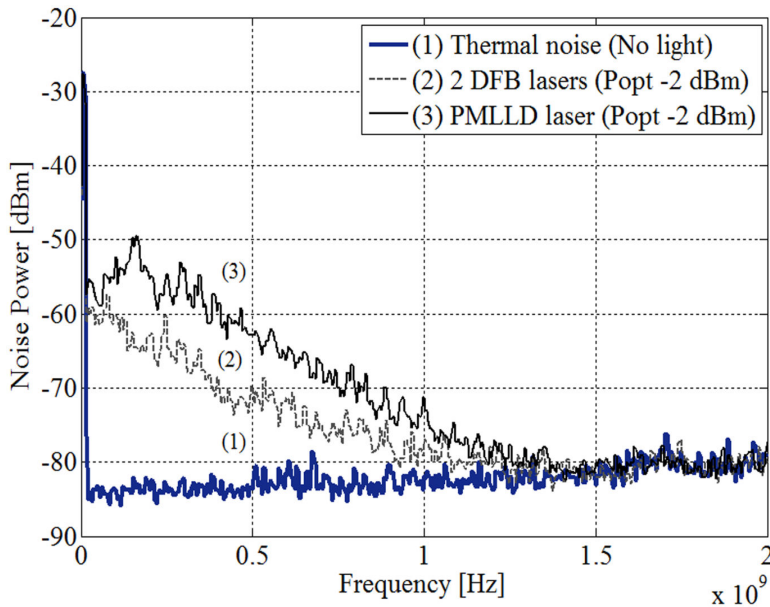


Figure 4.7 – Power spectrum of the received noise for RoF based on PMLLD and two DFB lasers.

4.5.2.4 Discussion on amplitude noise impact on EVM behavior

In section 4.3 and 4.4, it is shown that, using an ED, the EVM values only depend on the SNR of the received signal. In this section, the measured EVM values are compared with the theory presented in 4.36 in order to observe different noise (thermal, RIN, shot) impacts on EVM. Equation 4.36 is simulated in MATLAB substituting the measured parameters of 4.2 to 4.5. The simulation results are then normalized to that of the measurements so that a precise comparison between the two can be done.

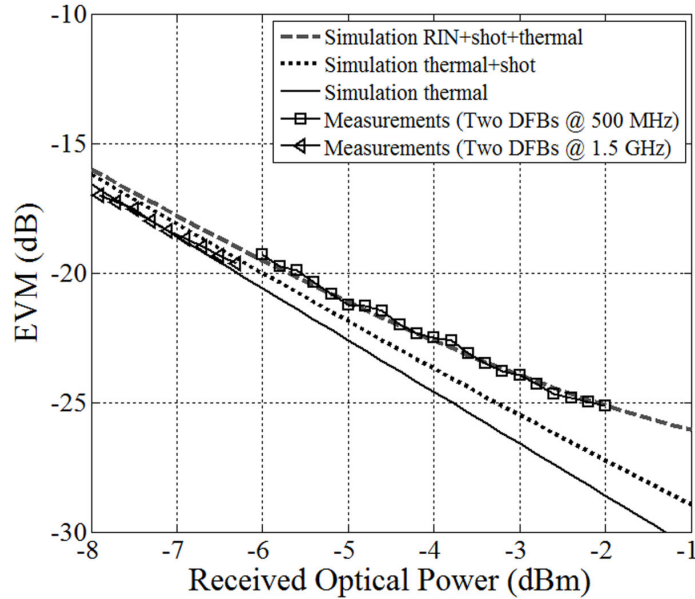


Figure 4.8 – Measurement and simulation results of EVM versus received optical power for RoF based on two DFBs

Figures 4.8 and 4.9 depict the measured and simulation EVM results versus received optical power (P_{opt}) in the RoF based on two DFB lasers and PMLLD, respectively. The measurements were done at 500 MHz and 1.5 GHz intermediate frequencies (f_{RF}) and the data rate of 100 Mbps using QPSK modulation. The simulation is done for three different scenarios; the grey dashed curve represents the EVM versus the received optical power when the RIN, shot and thermal noise are all taken into account, the black dot curve shows the EVM while the shot and thermal noise are the dominant noise, and the bold line with the slope of -20 dB per decade exhibits the EVM values when the thermal noise is dominating the RIN and shot noise. We need to mention that the impact of phase noise on EVM is vanished utilizing an ED.

In Figure 4.8, comparing the simulation results and the measured EVM values at 500 MHz (square points), it can be seen that the EVM values match the simulation results in which the RIN, shot and thermal noise are taken into account. It can also be observed that for the low optical power values the measured EVM values approach the thermal noise curve. In order to reduce the optical noise impact on EVM results the intermediate frequency is set to 1.5 GHz

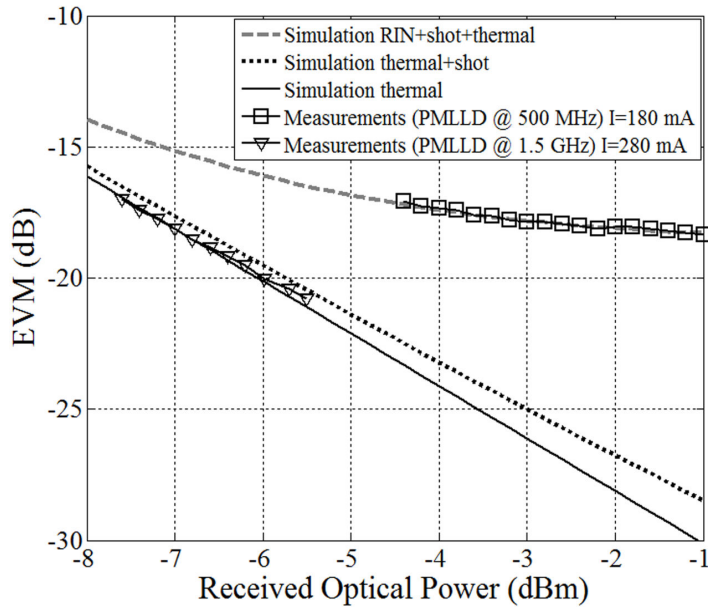


Figure 4.9 – Measurement and simulation results of EVM versus received optical power for RoF based on PMLLD

and the received optical power is attenuated. Observing the EVM results at 1.5 GHz (triangle points), it can be seen that the results are similar to the simulation in which the thermal noise is dominant. In Figure 4.9, the measured EVM values at 500 MHz and the simulation in which both optical and thermal noise are taken into account are also well matched. In order to reduce the RIN noise the biasing current of PMLLD is increased to 280 mA and intermediate frequency is set to 1.5 GHz. By changing these two parameters and also reducing the received optical power the EVM values curve (triangle points) is similar to the simulation in which the thermal noise is dominant noise.

Comparing the EVM results at intermediate frequency of 500 MHz in figures 4.8 and 4.9, it can be noticed that in Figure 4.8, the measured EVM values are close to the simulation results in which thermal noise is considered as dominant noise, while in Figure 4.9 the measurement results are similar to the scenario in which RIN is the dominant noise, especially for high optical power where the RIN and shot noise values are higher, corroborating the power spectrum of the noise presented in Figure 4.7. Observing this figure, it can be seen that the received optical noise in RoF based on PMLLD at 500 MHz is much higher than the optical noise detected in RoF system based on two DFBs at this frequency, and as the received optical power is the same, this indicates that the RIN using PMLLD is higher than the one using two DFBs. Thus, the EVM in RoF based on PMLLD is mostly impacted by the RIN while in RoF based on two DFBs the EVM results are not dominated by the optical noise.

In Figure 4.8 and Figure 4.9, it has been shown that just by observing the EVM trend versus received optical power and comparing with the simulations, one can determine the most

4.5. EVM in an RoF system based on non-coherent receiver

affecting noise on RoF system performance.

4.6 Conclusion

In this chapter, a complete theoretical and experimental study of amplitude noise impact on EVM values in mm-wave RoF system based on PMLLD and two DFB lasers is presented. A simulation method is presented that is able to determine, among different optical and electrical noise, the one which has the most effects on EVM results just by observing the EVM evolution versus received optical power. Using an envelope detector at the receiver, the phase noise impact is removed from the received signal. Thus, the impact of amplitude noise on EVM values is studied free of the phase noise influence on the system performance. Using this technique, a very good matching between the measured EVM values and the simulation results is achieved.

The results of this chapter are published in:

Khayatzadeh, R. ,HallakElwan, H. ,Poette, J. ,Cabon, B. "Impact of Amplitude Noise in Millimeter-wave Radio-over-Fiber Systems" IEEE Journal of Lightwave Technology, vol. 33, no. 13, pp. 2913-2919, Apr. 2015.

Bibliography

- [1] R. Khayatzadeh, J. Poette and B. Cabon, "Impact of phase noise in 60 GHz Radio-over-Fiber communication system based on passively mode locked laser," *J. Lightw. Technol.*, vol. 32, no. 20, pp. 3529-3535, May 2014.
- [2] R. Paschotta, article on "Laser noise" in RP Photonics, Encyclopedia., 1. Edition Oct. 2008, Wiley-VCH, ISBN 978-3-527-40828-3.
- [3] H. A. Haus, and A. Mecozzi, "Noise of mode-locked lasers," *IEEE J. Quantum Electron.*, vol. 29, no. 3, March 1993.
- [4] A. Georgiadis, "Gain, phase imbalance, and phase noise effects on error vector magnitude," *IEEE Trans. Veh. Technol.*, vol. 53, no. 2, March 2004.
- [5] W. Kester, "Converting oscillator phase noise to time jitter" Analog Devices, MA, USA, Tech. Rep. MT-008, 2009.

5 Conclusions and Prospects

This work is focused on radio over fiber communication systems at mm-wave frequencies higher than 60 GHz. The thesis elaborates on three crucial issues in these systems including: phase noise measurement of unstable optically generated mm-wave signals, elimination of phase noise impact on performance of RoF systems using non-coherent down conversion technique, and studying the amplitude noise impacts on performance of RoF system based on non-coherent detectors.

In the second chapter of this thesis, a new digital technique is presented which is able to measure the phase noise of any unstable mm-wave optically generated signal. In this technique, the classical power spectrum analyzer is replaced with a digital storage oscilloscope. Using digital oscilloscope, we are able to sample the signal faster than the frequency drift of the carrier which is not the case while using analogue techniques such as direct spectrum analyzer technique. Another advantage of using our digital technique is the numerical analysis that we do to extract the exact phase noise value without considering any small angle approximation. Assuming small angle approximation makes the results unreliable for the offset frequencies close to the carrier since at these offset frequencies the phase noise value is high and small angle approximation cannot be applied for the measurement. Our presented digital technique is able to measure the phase noise for a wide range of offset frequencies from close-in phase noise to far noise floor by adapting frequency resolution of measurement.

In the second part of the thesis, we present an RoF system based on non-coherent electrical frequency down conversion stage using an envelope detector which is robust against phase and frequency fluctuations of the optically generated carrier signal. The third chapter of this thesis is contributed to this work. In this chapter, two different frequency down conversion techniques are compared and it is shown that using non-coherent detection technique the EVM value is highly reduced compare to the technique based on mixer and local oscillator. The Q factor of more than 8 is demonstrated for RoF system based on non-coherent receiver using OOK modulation and data rate of 500 Mbps. As a part of this work, a W band RoF system based on two free running DFB lasers and a non-coherent detector is demonstrated at 100 GHz carrier for different modulation techniques (16 QAM, QPSK, OOK) and data rate of more

than 1 Gbps.

After demonstrating RoF system based on non-coherent receiver as a robust system against phase and frequency fluctuations, amplitude noise remains the main disturbing factor for this system. In the last chapter, a theoretical and experimental study of amplitude noise impact on performance of RoF systems based on non-coherent receivers is presented. In this study, a simulation technique based on theory is developed which is able to determine, among different optical and electrical noise, the one which has the dominant effect on EVM results. This simulation technique is based on observing the EVM evolution versus received optical power. The impact of phase noise on EVM values is vanished using non-coherent receiver and so the impact of amplitude noise on EVM values is studied free of the phase and frequency influence on performance of the system.

The results of this work are published in three IEEE journals and two international IEEE conferences.

Although a W-band RoF system based on envelope detector at 100 GHz is demonstrated in this work, an RoF system at higher frequencies such as 300 GHz to 500 GHz with much higher bit rate would be a possible extension of this PhD work. Furthermore, a WDM RoF system at W-band using a non-coherent receiver and based on passively mode locked lasers can also be considered as an important topic to be investigated.

A List of personal publications

International Journal Papers

- [1] **Khayatzadeh, R.** ;Hallak Elwan, H. ;Poette, J. ;Cabon, B. "Impact of Amplitude Noise in Millimeter-wave Radio-over-Fiber Systems" **IEEE J. Lightw. Technol.**, vol. 33, no. 13, pp. 2913-2919, Apr. 2015.
- [2] **Khayatzadeh, R.** ;Poette, J. ;Cabon, B. "Impact of Phase Noise in 60-GHz Radio-over-Fiber Communication System Based on Passively Mode-Locked Laser" **IEEE J. Lightw. Technol.**, vol. 32, no. 20, pp. 3529-3535, May 2014.
- [3] **Khayatzadeh, R.** ;Rzaigui, H. ;Poette, J. ;Cabon, B. "Accurate Millimeter-wave laser phase noise measurement technique" **IEEE Photon. Technol. Lett.**, vol. 25, no. 13, pp. 1218-1221, Jul. 2013.
- [4] Rzaigui, H. ;Poette, J. ;Brendel, F. ;Cabon, B. ;**Khayatzadeh, R.** "Optical Heterodyning for Reduction of Chromatic Dispersion Sensitivity in 60 GHz Mode-Locked Laser Systems" **IEEE J. Lightw. Technol.**, vol. 31, no. 13, pp. 2955-2960, Jul. 2013.

International Conference Papers

- [5] **Khayatzadeh, R.** ;Poette, J. ;Rzaigui, H. ;Cabon, B. "Coherent and non-coherent receivers in 60 GHz RoF system based on passively mode-locked laser" IEEE International Topical Meeting on Microwave Photonics , 28-31 October 2013, Alexandria, Virginia, US.
- [6] **Khayatzadeh, R.** ;Hallak-Elwan, H. ;Poette, J. ;Cabon, B. "100 GHz RoF system based on two free running lasers and non-coherent receiver" IEEE International Topical Meeting on Microwave Photonics 2015(submitted).
- [7] Hallak-Elwan, H. ;**Khayatzadeh, R.** ;Poette, J. ;Cabon, B. "Relative intensity noise in optical heterodyning applied to millimeter-wave systems" IEEE International Topical Meeting on

Appendix A. List of personal publications

Microwave Photonics 2015(submitted).